

NANO-SELF-ASSEMBLY IN Mn-BASED SPINELS THROUGH SOLID STATE PROCESS

by

CHENGLIN ZHANG

A Dissertation submitted to the
Graduate School-New Brunswick
Rutgers, The State University of New Jersey
in partial fulfillment of the requirements

for the degree of

Doctor of Philosophy

Graduate Program in Physics

Written under the direction of

Sang-Wook Cheong

and approved by

New Brunswick, New Jersey

October, 2008

Abstract of the Dissertation

Nano-Self-Assembly in Mn-based Spinel through Solid State Process

by

Chenglin Zhang

Dissertation Director:

Sang-Wook Cheong

Transition-metal oxides characterized with anisotropic d-orbital electrons are subject to intense discussion in strongly correlated electron systems, ranging from colossal magnetoresistance (CMR) to high temperature superconductivity (HTSC). The orbital degree of freedom often underpins complex physical properties and a variety of extraordinary phenomena while coupling with charge, spin and lattice. In this thesis, we demonstrate a fascinating example of orbital-related physical properties in Mn-based spinels. The strong octahedral preference of Jahn-Teller ions Mn^{3+} results in simultaneous chemical and structural phase separation into Mn-poor (cubic) and Mn-rich (tetragonal) regions, forming two types of rectangular nanorods with cross section checkerboard-like (CB). Because of the pioneering discovery of checkerboards in the nonmagnetic $\text{ZnMn}_x\text{Ga}_{1-x}\text{O}_4$, we chose to study two magnetic spinel systems: (1) $\text{Mg}(\text{Mn}_x\text{Fe}_{1-x})\text{O}_4$, where unfortunately only poorly-ordered magnetic nano CBs were observed; and (2) Mn-doped CoFe_2O_4 , the nano CBs with distinct magnetic properties and tunable sizes achieved here are highly ordered, exhibiting a nearly ideal architecture for the patterned perpendicular recording medium. The evolution of such compositional separation and topological nanoscale ordering is reasonably understood based on a three dimensional (3D) phase-field microelasticity (PFM) model.

Acknowledgements

First of all, I sincerely thank my advisor, Sang-Wook Cheong, who took me to Rutgers and introduced me into materials physics. Very Special thanks go to Namjung Hur and Bing Liang, who taught me experimental techniques hand by hand at my early stage in the lab. I greatly appreciate Soonyong Park, who patiently guided me like an older brother in both study and life. I would like to acknowledge the significant help from my previous group members: Sabya Guha, William Ratcliff, Yew-San Hor, Peter. Sharma, Seong-baek Kim, Han-Jin Noh and Toshihiro Asada, and current group members: Young Jai Choi, Nara Lee, Hee Taek Yi, Seongsu Lee and Taekjip Choi, and undergraduate students: Hemal Vora, Matthew Vannucci, Sean Franckle and Daniel Kwok. I express my sincere appreciation to Sunmog Yeo, Yoichi horibe, especially Tien-Ming Chuang and Professor Cheng-Hsuan Chen at National Taiwan University, who significantly contributed to the work in this thesis. In the progress of this work, I benefited from useful discussion from Yong Ni, a postdoctoral fellow at Department of Materials Science and Engineering. I thank my PhD committee for their valuable comments: Premala Chandra, Paul Leath, Theodore Williams, and Tao Zhou. I thank the helpful suggestions from Mark Croft and Weida Wu. I am grateful to our business office people: Valerie Cardinale, Helen Posluszny and Frances Delucia, for their great services.

Finally, I sincerely express appreciation to my friends: Xifan Wu, Xinjie Wang, Junyi Li, Tian Feng, Weihua Zheng, Jian Wei, Shitao Lou, Hao Wang, Zhen Qin, Xiongying Tu, Quankun Sun, Yanxi Cai, Ivan Skachko and Bumsu Lee. Over the years at Rutgers, I enjoyed the time with them. Particular thanks for help in various ways go to

my housemate and family doctor Paul Gwozdz and of course his lovely dog Brianna. I am so happy to have the wonderful four years with them at Penrose 10.

Table of Contents

Abstract of the Dissertation	ii
Acknowledgements.....	iv
Table of Contents.....	vi
List of Figures	viii
I. Phase Separation Associated with Self-assembled Patterns in Oxides.....	1
1. Introduction to Spinodal Decomposition	2
2. Introduction to Phase Separation in Oxides	7
3. Phase Separation in Manganites and Cuprates	8
4. Checkerboards in the Perovskite ($\text{Nd}_{2/3-x}\text{Li}_{1/3x}\text{TiO}_3$)	12
5. Checkerboards in the Polycrystalline ZnMnGaO_4	13
6. Checkerboards in the ZnMnGaO_4 Thin Film.....	15
7. Background of the Perpendicular Recording.....	20
8. Conclusion.....	22
9. References.....	24
II. Nanostructure in the Magnetic Spinel $\text{Mg}(\text{Mn,Fe})_2\text{O}_4$	26
1. Introduction.....	27
2. Experimental Method.....	28
3. Result and Discussion	28
4. Conclusion.....	36
5. References.....	37
III. Nanostructure in the Mn-doped CoFe_2O_4	41

1. Introduction.....	42
2. Experimental Method.....	42
3. Result and Discussion.....	43
4. The Mechanism in the Formation of Nanocheckerboards	56
5. Conclusion	63
6. References.....	65
IV. Composition and Strain Effect on the Microstructure of the Mn-based Spinel.....	68
1. Introduction.....	69
2. Experimental Method.....	69
3. Result and Discussion.....	70
6. Conclusion	81
7. References.....	82
V. Conclusion	83
Appendix I: Coercivity and nanostructure in magnetic spinel $\text{Mg}(\text{Mn,Fe})_2\text{O}_4$ (<i>Appl Phys. Lett.</i> , 2007).....	87
Appendix II: Magnetic nanocheckerboards with tunable sizes in the Mn-doped CoFe_2O_4 Spinel (<i>Appl.Phys.Lett.</i> , 2007).....	90
Curriculum Vitae	93

List of Figures

FIG. I.1. A typical spinodal decomposition phase diagram.....	4
FIG. I.2. Morphology of liquid mixture changes with time and convection number [2]...	6
FIG. I.3. Schematic diagram showing the coexistence of the charge ordered insulating (dark area) and FM metallic (white area) domains in $(\text{La, Pr, Ca})_x\text{MnO}_3$. Arrows show alignment in a magnetic field [11].....	10
FIG. I.4. Inhomogeneous states in HTSC materials. (a) Schematic stripes in $\text{La}_{2-x}\text{Ba}_x\text{CuO}_{4+\delta}$ (circles are holes; arrows, spins). (b) d -wave SC gap real-space distribution in $\text{Bi}_2\text{Sr}_2\text{CaCu}_2\text{O}_{8+\delta}$. The entire frame is $560 \text{ \AA} \times 560 \text{ \AA}$. (c) charge-order state in $\text{Ca}_{2-x}\text{Na}_x\text{CuO}_2\text{Cl}_2$ [5].....	11
FIG. I.5. (a) TEM image of polycrystalline $(\text{Nd}_{0.53}\text{Li}_{0.43})\text{TiO}_3$ shows chessboard-type phase separation. (b) A typical spinodal decomposition (c) and (d) The phase separation in $(\text{Nd}_{2/3-x}\text{Li}_{1/3+x})\text{TiO}_3$ with $x \sim 0.05$ and ~ 0.12 . The black region is Li-poor and the white region Li-rich [13].....	14
FIG. I.6. (a) and (b), TEM images with the relative sample orientation of $\sim 90^\circ$. The checkerboard domain denoted as “A” in the $[100]$ incidence image displays a herringbone pattern for the $[010]$ incidence, demonstrating that the checkerboard and herringbone images are different angular views of the same nanoscale object. (c) A schematic representation of two (110) twin-related colonies of a CB structure, where yellow regions show cubic phase; blue regions tetragonal equilibrium phase with different orientations [14].....	16
FIG. I.7. A schematic view of the ordering of cubic and orthorhombically distorted (O) phases. Two O-type rods, having two different directions of Mn orbital order, and two	

C-type rods with a relative 6° rotation, stack in the checkerboard pattern [7].....	18
FIG. I.8. A self-assembled nanocheckerboard ZnMnGaO_4 film grown on a (001) MgO substrate. (a) TEM side-view image of the spinel film at low magnification. The picture is normal to the (010) axis. Pt is used for a capping layer for focused ion beam (FIB) sample preparation. (b) Schematic picture of a well-oriented nanorod spinel film formed on a substrate. The nanorods are aligned along the [001] direction. (c) A TEM dark field image near the top surface showing a checkerboard domain. (d) A TEM right field side-view image near the MgO substrate showing the nanostructured film, a thin transition layer, and the substrate, from top to bottom [15].....	19
Fig. I.9. A schematic view of the perpendicular recording method [18].....	21
FIG. II.1. (a), M vs H at 5 K for $x = 1.5$ with selected CR's. The inset displays magnetic coercivity vs. CR. Q represents quenching in cold water. (b), XRD patterns at room temperature for $x = 1.5$ with selected CR's. C' represents the cubic phase of the quenched specimen, and the cubic XRD peaks of (220) and (311) are denoted. T' represents the tetragonal phase of the 50°C/h -cooled specimen, and the tetragonal XRD peaks of (103) and (211) are denoted. C and T represent the cubic and tetragonal phases after phase separation, respectively. (c), XRD patterns of the quenched (solid line) and 0.3°C/h -cooled (dashed line) specimens of selected Mn concentrations.....	30
FIG. II.2. (a), Phase diagram of $\text{Mg}(\text{Mn}, \text{Fe})_2\text{O}_4$. Colored area depicts the miscibility gap region in the 5°C/h -cooled specimens. Arrow denotes the tetragonal T phase of $x=2$. \triangle and ∇ denote the JT transition temperature, T_{JT} , upon warming and cooling,	

respectively, determined from high-temperature resistivity measurements. \square and \bigcirc denote ferrimagnetic T_C of the 5 °C/h-cooled and quenched specimens, respectively. PM and FM stand for paramagnetic and ferrimagnetic, respectively. The inset displays logarithmic resistivity vs. temperature upon warming (red) and cooling (blue) for $x = 1.5$. (b), T_C (\blacklozenge) and coercivity (\redlozenge) vs. logarithmic CR for $x = 1.5$. Lines are drawn for guides to the eyes. The mixture of C+T forms for very slow CR (the most left region). The shaded areas at the left and right hand sides represent the regions for the T' and C' phases, respectively. Between the shaded regions, mixed C'+T' is observed. The inset displays the temperature dependence of zero field-cooled M/H in H=2 KOe for $x = 1.5$ with selected CR's.....33

FIG. II.3. (a), M vs. H of the 10 °C/h-cooled $\text{MgMn}_{1.5}\text{Fe}_{0.5}\text{O}_4$ at selected temperatures. (b), H_c (\star) and M_r (\star) vs. temperature. (c), Magnetization vs. temperature of the 10 °C/h-cooled $\text{MgMn}_{1.5}\text{Fe}_{0.5}\text{O}_4$ (\redlozenge) and 4 nano-meter size spherical Co particles embedded in Al_2O_3 matrix (\blacktriangleleft : from Ref. 29). Magnetization is normalized by the maximum value. (d) and (e), TEM images of the 10 °C/h-cooled specimen, showing checkerboard and herringbone patterns, respectively. The arrows represent the crystallographic axes of the cubic spinel unit cell. (f), a schematic view of the circled region in (d). The blue and yellow regions represent the C and T phases, respectively.....35

FIG. III.1. Bright field TEM images of $\text{Co}_{0.6}\text{Fe}_{0.9}\text{Mn}_{1.5}\text{O}_4$ annealed at 375 °C for 324 hours. (a) Coexisting nanoscale checkerboard (CB) and herringbone (HB) domains, (b) and (c) Expanded views of checkerboards (the upper circled region) and

herringbones (the bottom circled region). The insets are the corresponding diffraction patterns.....	44
FIG. III.2. (a) High-resolution TEM image of the checkerboard in the 324 h-annealed specimen at 375 °C, which consists of two cubic domains α and γ with different rotations and two tetragonal domains β and δ with different orientations. (b) Dark field image taken by using γ spot around (008) position; (c) The diffraction pattern of checkerboard domains, the dashed lines with arrows indicate the rotations of the two cubic domains.....	
	47
FIG. III.3. (a) XRD patterns of $\text{Co}_{0.6}\text{Fe}_{0.9}\text{Mn}_{1.5}\text{O}_4$ annealed at 375 °C with selected annealing time, C' is the cubic phase of the quenched specimen, T' is the tetragonal phase of the 3.6 h-annealed specimen, and the cubic and tetragonal peaks are denoted. C and T are the final equilibrium cubic and tetragonal phases after phase separation. The dashed lines indicate the positions of (311) and (211) peaks; (b) Schematic process of crystal structure evolution with prolonging annealing time; (c)-(f) The corresponding microstructure development with annealing time. All images have the same scale.....	
	49
FIG. III.4. Magnetic properties of $\text{Co}_{0.6}\text{Fe}_{0.9}\text{Mn}_{1.5}\text{O}_4$ annealed at 375 °C with selected annealing time. (a) Normalized M/H vs temperature with 200 Oe field cooling ; (b) H_c (●) and M_r (○) vs annealing time in the logarithmic scale at 5 K, the shadow and patterned regions indicate the structure evolution with annealing time; (c) $M(H)$ at 5 K; (d) H_c (■) and M_r (□) vs temperature for the 156 h-annealed specimen.....	
	54
FIG. III.5. A schematic free energy vs. composition diagram for the spinodal decomposition with coherent cubic and tetragonal phases [26].....	
	57

- FIG. III.6. The 3D modeling of the microstructure evolution at $c > c_o(T)$ with different time scale. The black color is the cubic phases. Other colors are the tetragonal domains with three different orientations. The diffraction patterns in the insets are generated along [010] axis of the tetragonal phases. (d)-(h) only show the green tetragonal domains by the Fourier filtering to remove small perturbations from the back Fourier transformation describing the image contrast [26].....60
- FIG. III.7. (a) The dark field images of the as-grown ZMGO thin film. (b) The schematic view of the diffraction pattern of CBs. The A and C peaks come from the tetragonal T' phase with different orientations. (c) and (d) are the magnified dark field images of the region marked with dashed line in (a) by using A and C peaks, respectively [from Y. Horibe].....62
- FIG. III.8 (a) and (b) are the high magnified TEM images of Fig. III.7(c) and Fig. III.7(d), respectively. The red arrows indicate that the contrast of the white region in (a) is inversed to the dark region in (b). (c) is the overlap of (a) and (b), showing a tendency of forming CBs [from Y. Horibe].....64
- FIG. IV.1. (a) Bright field TEM images of the annealed polycrystal $\text{Co}_{0.5}\text{FeMn}_{1.5}\text{O}_4$. Coexisting nanoscale CB and HB domains, the dashed lines indicate the habit plane formed in the cubic to tetragonal transformation, arrows indicate the [001] direction of cubic phase; (b) and (c) Expanded views of HBs (the bottom circled region) and CBs (the upper circled region). The insets are the corresponding diffraction patterns.....71
- FIG. IV.2 (a) XRD patterns of $\text{Co}_{0.5}\text{FeMn}_{1.5}\text{O}_4$, $\text{Co}_{0.5}\text{Fe}_{1.7}\text{Mn}_{0.8}\text{O}_4$ (cubic) and $\text{Co}_{0.5}\text{Fe}_{0.3}\text{Mn}_{2.2}\text{O}_4$ (tetragonal). All of them have identical heat treatment. The latter

two compositions are the speinodal separated phases of $\text{Co}_{0.5}\text{FeMn}_{1.5}\text{O}_4$. The dashed line indicates the peak shift of C and T phases. (b) The measurement of $\ln\rho$ vs. temperature. The arrows indicate the warming and cooling processes. (c) $M(H)$ for the three samples at room temperature. (d) Normalized M/H vs. temperature of the annealed $\text{Co}_{0.5}\text{FeMn}_{1.5}\text{O}_4$ with 200 Oe field cooling.....	73
FIG. IV.3 (a) XRD of the annealed $\text{Co}_{0.5}\text{FeMn}_{1.5}\text{O}_4$ polycrystal sintered at different temperatures and annealed single crystal. (b) and (c) Bright field TEM image and diffraction patter of the polycrystal sintered at 1200 °C.....	75
FIG. IV.4 (a) Bright field image of the annealed $\text{Co}_{0.5}\text{FeMn}_{1.5}\text{O}_4$ single crystal. (b) Expanded view the circle region in (a). (c) The diffraction pattern.....	76
FIG. IV.5 (a) and (b) Bright field image of $\text{CoFe}_{0.55}\text{Mn}_{1.45}\text{O}_4$ polycrystals viewed from [001] and [111] directions of C phase. (sample made by S. Yeo) (c) Bright field image of $\text{CoFe}_{0.55}\text{Mn}_{1.45}\text{O}_4$ single crystal. (d) The high magnification image of the circled region in (c).....	79
FIG. IV.6 (a) Bright field image of the annealed $\text{Co}_{1.6}\text{Mn}_{1.4}\text{O}_4$ polycrystal. (b) The optical picture of the annealed $\text{Fe}_{0.9}\text{Mn}_{2.1}\text{O}_4$ single crystal along the growth direction. (c) and (d) Bright field image of annealed $\text{Co}_{0.4}\text{FeMn}_{1.6}\text{O}_4$ polycrystal and the diffraction patter, respectively.....	80

Chapter I

Phase Separation Associated with Self-assembled Patterns in Oxides

1. Introduction to Spinodal Decomposition

Phase separation occurs when a homogenous system separates spatially into two or more phases. This occurs in the unstable region of the phase diagram, as illustrated in Fig. I.1, which is a binary eutectic phase diagram for the mixing of two types of atoms A and B, and which was obtained by the common tangent construction from the free energy diagram. This picture basically is better to describe for liquid mixtures. The boundary of the unstable region is the binodal curve, which is the limit of solid solubility. The single-phase region is outside the binodal curve. Here, we concerned about the region inside the binodal curve, which is also called the miscibility gap. Any homogeneous solution cooled into this region spatially decomposes into A-rich and B-rich phases. The dashed line inside the miscibility gap is the spinodal region. The point where the binodal and spinodal curves meet is the critical point.

Phase separation takes place through either nucleation and growth or spinodal decomposition depending on the curvature of $\frac{\partial^2 G}{\partial c^2}$ in the free-energy phase diagram, where G is the free energy of the system, and c is the chemical concentration. The underlying mechanisms between them are distinguishable. In the region between the binodal and spinodal where $\frac{\partial^2 G}{\partial c^2} > 0$, nucleation and growth occurs associated with large initial composition fluctuations. Therefore, the growth is slow because atoms have to migrate over long distance. The overall composition of the precipitate remains unchanged in the whole process. In contrast, spinodal decomposition happens in the region where $\frac{\partial^2 G}{\partial c^2} < 0$. In this region, infinitesimal concentration fluctuation will trigger

spontaneous phase separation to lower the free energy. The inhomogeneities are largely different in chemical composition, but often with identical crystal structures. The compositions of the product vary with time before reaching equilibrium, and the interfaces of the different phases become sharper with time. The boundary between the nucleation/growth region and spinodal decomposition region, $\frac{\partial^2 G}{\partial c^2} = 0$, is the spinodal curve.

The process of phase separation is quantitatively described by the Cahn-Hilliard equation. For 1D cases with mass conservation, the continuity equation is written as

$$\frac{\partial c}{\partial t} = -\frac{\partial J}{\partial x} = M \frac{\partial^2 f_0}{\partial c^2} \frac{\partial^2 c}{\partial x^2} + 2MK \frac{\partial^4 c}{\partial x^4},$$

where c is the local concentration, J is the flux, M is an Onsager coefficient and K is the gradient energy coefficient. The effective diffusion coefficient D_{eff} is given by

$$D_{eff} = M \frac{\partial^2 f_0}{\partial c^2} \text{ where } \frac{\partial^2 f_0}{\partial c^2} \text{ is negative. This indicates that } D_{eff} \text{ is negative since } M \text{ is}$$

always positive. In contrast to the downhill diffusion, the diffusion is uphill in spinodal decomposition. The chemical difference between the neighboring phases increases with time. The general solution of the continuity equation is

$$c(x, t) = c_0 + \cos(qx) \exp[-(D_{eff} q^2 t (1 + \frac{2kq^2}{f_0''}))]$$

Where c_0 is the initial composition, f_0'' is the second derivative of the free energy in the respect to the composition, and q is the wave vector of the composition fluctuation. The

amplitude of the composition fluctuation is defined as $R(q) = -D_{eff} q^2 (1 + \frac{2kq^2}{f_0''})$. By

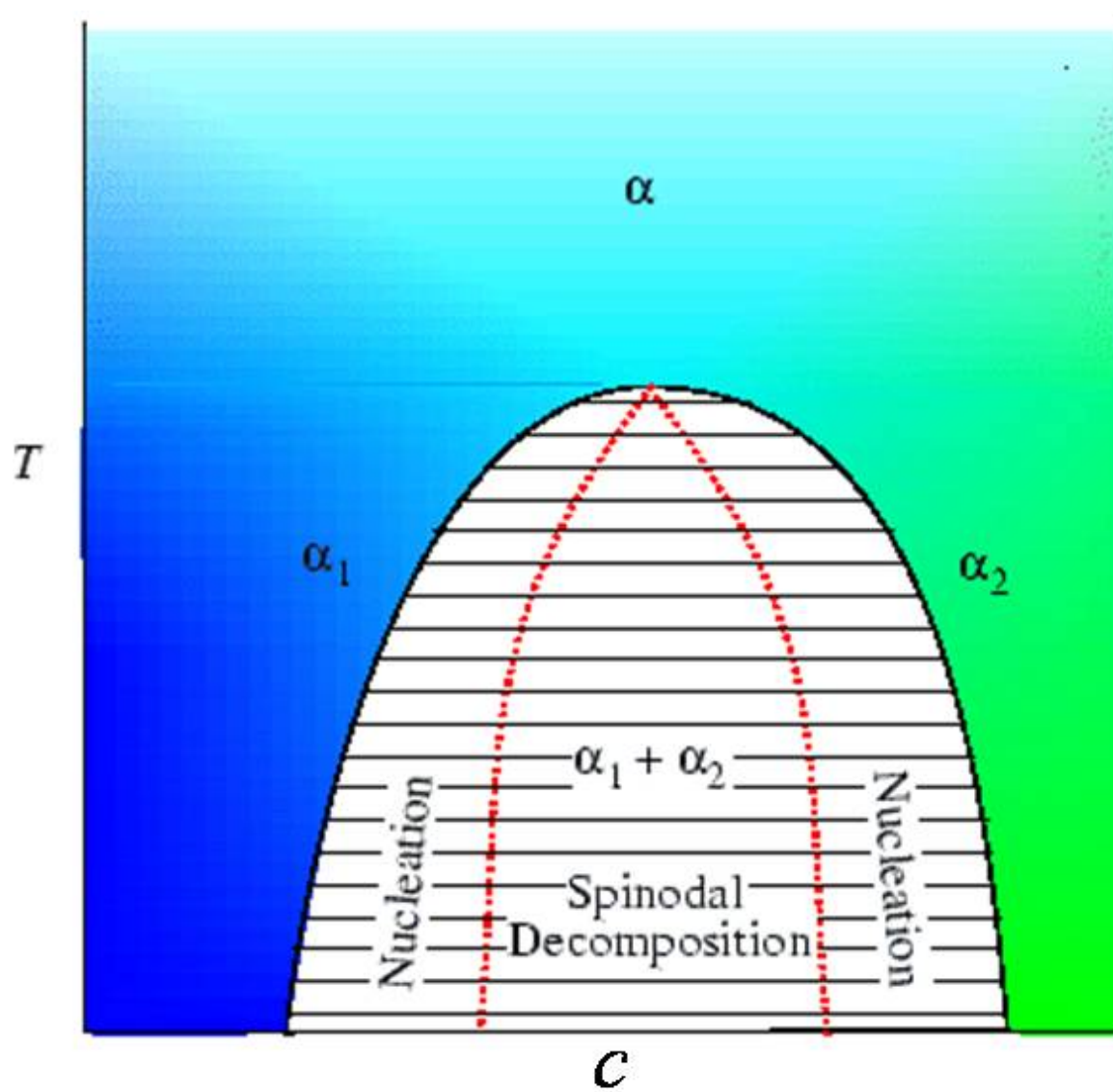


FIG. I.1. A typical spinodal decomposition phase diagram.

taking $\frac{dR(q)}{dq} = 0$, the largest wave vector corresponds to $q_{\max} = \frac{1}{2} \sqrt{-\frac{f_0''}{K}}$. The fastest growing wavelength is $\lambda_{\max} = \frac{2\pi}{q_{\max}}$. Obviously, microstructure at finer scale will be obtained by deeply quenching the parent compound further into the spinodal region because f_0'' is more negative [1].

The typical morphology of spinodal decomposition in a liquid mixture is a random interconnected structure as shown in Fig. I.2 [2]. The dimensionless Peclet number α is defined as the ratio between the convective and diffusive mass fluxes, where α is often small due to the high viscosity of liquid. The droplets form first followed by growth. But for most liquids, α is typically in the range from 10^3 to 10^5 . In the early stages of phase separation, the diffusion is dominant so that the size of microstructure increases linearly with time. Later on, the convection becomes the dominant way for mass transport, therefore, and the microstructure grows as $t^{1/3}$. With increasing Peclet number, droplet formation and growth occur simultaneously. The driving force of the microstructure coarsening is a capillarity effect. Large droplets grow at the expense of shrinking small ones depending on the balance between the surface energy and the bulk free energy.

We briefly describe the microstructure formation and coarsening in spinodal decomposition by the simplest theoretical model “1D linear Cahn-Hilliard equation” to qualitatively understand the underlying mechanisms. As a matter of fact, the situation turns out to be much more complicated in solid-solid transitions due to the elastic strain energy. The Time-Dependent Ginzburg-Landau phase-field approach is employed to explain the coherent microstructures by taking into account the ordering, decomposition and strain-induced coarsening. This effectively describes the decomposition when the

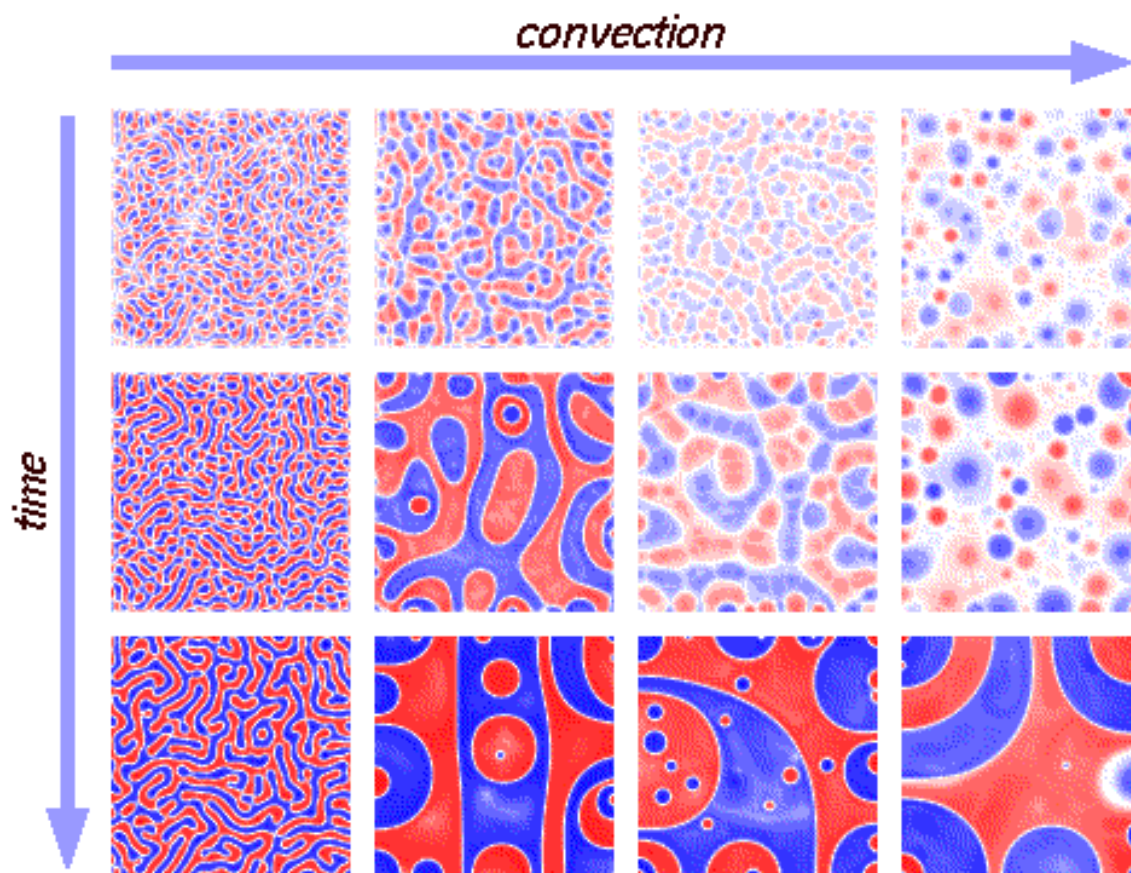


FIG. I.2. Morphology of liquid mixture changes with time and convection number [2].

crystal symmetry of precipitated phase is different from that of parent compound. The model is further improved by stochastic time-dependent equations involving some initial fluctuation. 2D computer simulations based on this model has been used to successfully explain the checkerboard-like microstructure in the cubic-tetragonal transformation of Co-Pt alloy. The simulations are good agreement with experimental observations [3].

A 3D computer simulation based on the same model was attempted to clarify the formation of checkerboard structure in some spinel systems. This will be discussed in the following chapters [4]. The experimental situation is more complicated than expected because the phase transformation is diffusion-dependent associated with Jahn-Teller (JT) distortion. The microstructure formation is intrinsically different from whatever pattern has been observed before. In the following sections, a few patterns in oxides, formed through phase separation associated with JT distortion, will be presented.

2. Introduction to Phase Separation in Oxides

Phase separations in transition metal oxides such as rare earth manganites, cuprates and cobaltates are intriguing phenomena that occurs in a broad range from bulk materials to thin films as well as multilayer heterostructures. In a certain temperature window, a pure monophasic composition separates into two or multiple competing phases with distinct electronic and magnetic properties, often associated with spontaneous formation of self-assembly patterns. In many cases, simultaneous interactions among lattice, charge, spin and orbital account for the rich variety of patterns. Particularly, contributions from the charge, spin and orbital degrees of freedom are more or less relevant, and able to

bring forth dramatic responses to subtle external perturbations for example colossal magnetoresistance (CMR) effect in perovskite manganites [5-7].

Significantly different from intergrowth of related phases, phase separations in various length scales lead to entirely new physical properties which are totally unexpected in the parent compounds. Such phase separations are tunable with composition, temperature, magnetic/electric field, photo-excitations and pressure etc. Apart from CMR, many novel physical properties have emerged with the electronic and magnetic inhomogeneities which could be exploited for a number of technological applications. For instance spintronics, the energy difference between distinguished phases is usually very small, therefore states can be quickly switched by minute perturbations in an input signal [8,9].

Physical properties are related with not only the atomic crystal structure, but also the detailed nature of the microstructure. Engineering of microstructures forming through phase separation might lead to a revolution of recording medium. The presence of phase separation is argued as an intrinsic feature in the spin-charge-orbital coupled systems in transition-metal oxides. Understanding the underlying mechanism of self-assembly patterns caused by the coexistence of coherent phases will provide significant insight into the nature of many exotic phenomena including CMR and HTSC, which are not understandable based on homogenous systems [5].

3. Phase Separation in Manganites and Cuprates

Perovskite manganite with CMR effect is the most representative system showing versatile unconventional electron-electron or electron-lattice interactions. Phase

separation is argued as the essential ingredient in CMR physics. It has been unraveled by considerable experiments that coexistence of competing phases near bicritical point in manganites is indeed a ground state. Two kinds phase separation are generally recognized: electronic phase separation and disorder-induced phase separation [5,9,10].

Self-assembly patterns formed through phase separations vary widely on time scales from statics to dynamic, as well as length scales from nano to micron, giving rise to distinct signatures in X-ray, neutron diffraction patterns, as well as TEM and other spectroscopies. In the case of phase separation driven by quenched disorder arising from inherent chemical randomness or intentional impurity doping, micron grain-like pattern characterized by percolation are observed in phases with equal densities. However, it is not possible to form long-range ordered microstructure in electronic phase separation owing to the high coulomb energy cost. Therefore, glass-like phase separation at nanoscale is observed in some compounds wherein ferromagnetic (FM) metallic and antiferromagnetic insulating phases (AFI) with comparable energies coexist. The two types of domains with contrasting electronic and magnetic properties are separated by first-order transition with different densities. Meanwhile, the large strain mismatch between the domains also contributes to induce the nanoscale phase separation [5]. Evidence of such phase separation is found in $(\text{La}, \text{Pr}, \text{Ca})\text{MnO}_3$ as shown in Fig. I. 3(a) [11].

A variety of electronic inhomogeneous states have also been unveiled in cuprates for examples: stripes in $\text{La}_{2-x}\text{Ba}_x\text{CuO}_{4+\delta}$, patchworks in d-wave superconductor gaps in $\text{Bi}_2\text{Sr}_2\text{CaCu}_2\text{O}_{8+\delta}$ (Bi-2212), checkerboards in $\text{Ca}_{2-x}\text{Na}_x\text{CuO}_2\text{Cl}_2$ as shown in Fig. I.4. The tendency of phase separation or intrinsic hole clustering is universally observed in doped

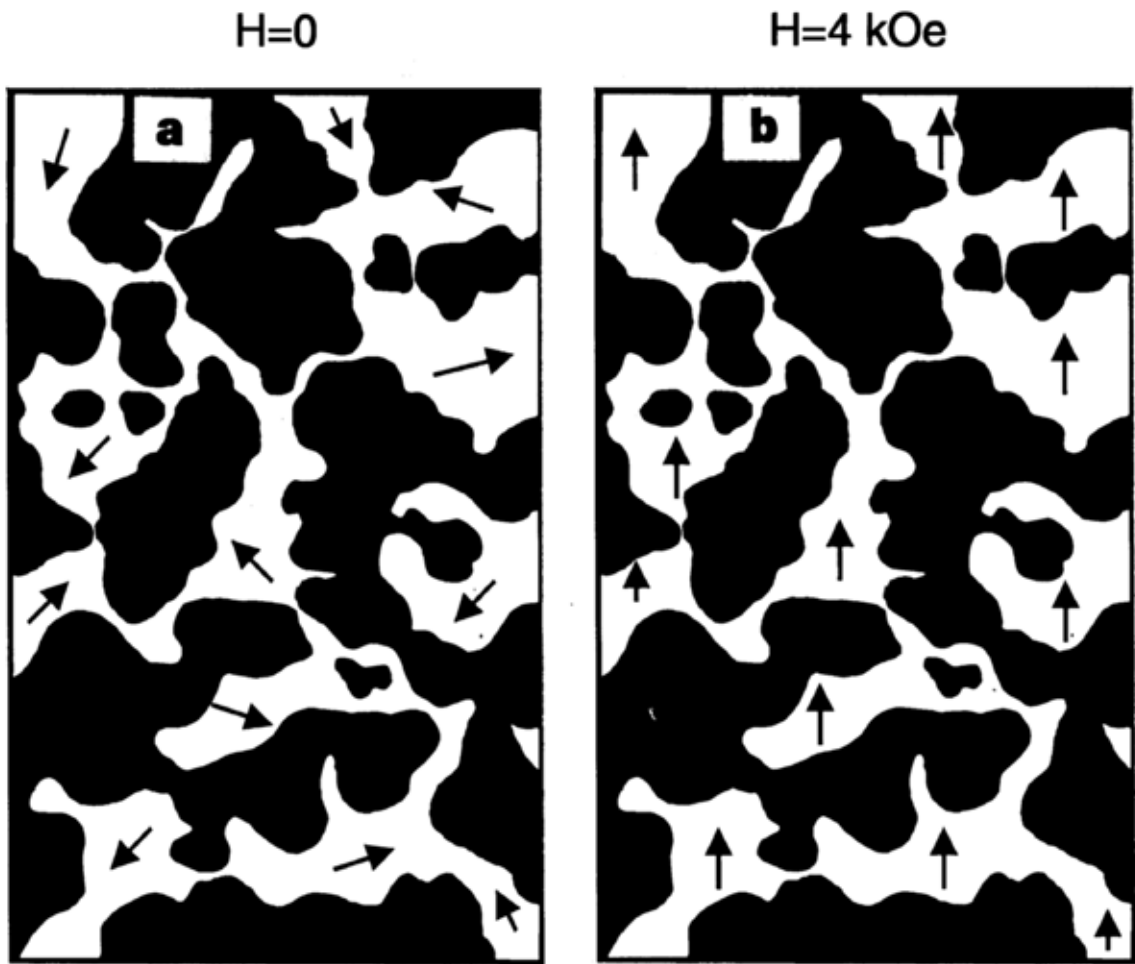


FIG. I.3. Schematic diagram showing the coexistence of the charge ordered insulating (dark area) and FM metallic (white area) domains in $(\text{La, Pr, Ca})\text{xMnO}_3$. Arrows show alignment in a magnetic field [11].

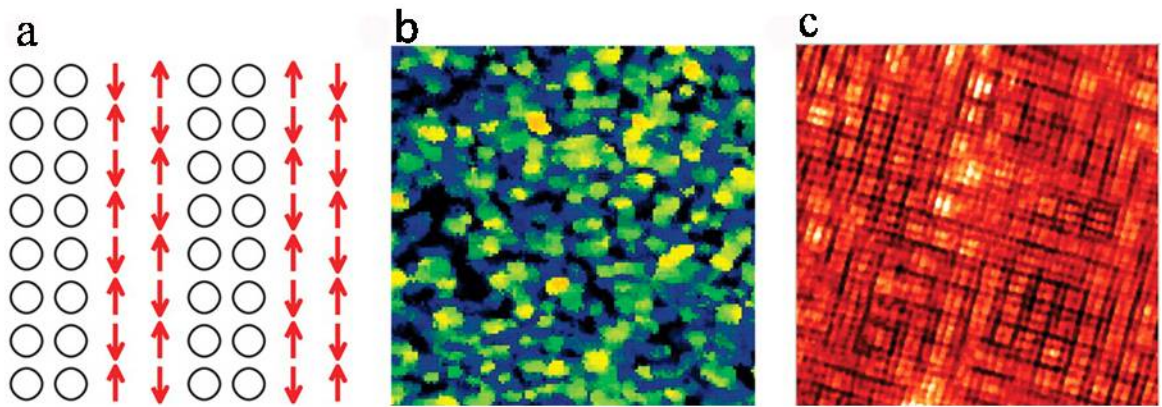


FIG. I.4. Inhomogeneous states in HTSC materials. (a) Schematic stripes in $\text{La}_{2-x}\text{Ba}_x\text{CuO}_{4+\delta}$ (circles are holes; arrows, spins). (b) d -wave SC gap real-space distribution in $\text{Bi}_2\text{Sr}_2\text{CaCu}_2\text{O}_{8+\delta}$. The entire frame is $560 \text{ \AA} \times 560 \text{ \AA}$. (c) charge-order state in $\text{Ca}_{2-x}\text{Na}_x\text{CuO}_2\text{Cl}_2$ [5].

cuprates. A good example is $\text{La}_2\text{CuO}_{4+\delta}$ which, below a specific temperature, undergoes a reversible spinodal decomposition into two nearly identical orthorhombic phases with distinct magnetic and electrical properties: an oxygen-excess (hole-rich) region and an oxygen-deficient (hole-poor) region. The former is a superconducting phase with $T_C \sim 35$ K, while the latter is an AFM insulated phase with $T_N \sim 250$ K. The two phases are alternately arranged in CuO_2 sheets and form quasi-one-dimensional stripes as visualized in Fig. I.4(a) [5,12].

Although the nature of phase segregation in the physics of manganites and cuprates is still controversial, it is no doubt that this unusual feature is essential to understand the underlying mechanism while incorporating with lattice distortion, strain, and quenched disorder etc.

4. Checkerboards in the Perovskite ($\text{Nd}_{2/3-x}\text{Li}_{3x}\text{TiO}_3$)

Two-dimensional (2D) modulated nanocheckerboards associated with chemical phase separation has been recently observed in the Li-containing perovskites ($\text{Nd}_{2/3-x}\text{Li}_{3x}\text{TiO}_3$) as shown by TEM image in Fig. I.5(a). Due to the large number of highly mobile Li^+ ions and vacancies at the A sites, the sample undergoes spinodal decomposition in the process of cooling from high temperature, whereby the sample spontaneously separates into $\text{Nd}_{1/2}\text{Li}_{1/2}\text{TiO}_3$ and $\text{Nd}_{2/3}\text{TiO}_3$ with roughly identical periodicities. Both diamond and checkerboard contrasts are shown in Fig. I.5(a). The light square nanodomains rich with Li are separated by dark zigzag boundary regions rich with Nd.

Generally, patterns formed through spinodal decomposition are neither symmetric nor random (Fig. I.5(b)). However, a highly ordered superstructure is adopted in this specific system as schematically illustrated in Fig. I.5(c) and (d). The periodicity can be adjusted in a range from 5 to 11 nm by changing the composition. With increasing Li concentration, the Li-rich regions increase at the expense of the Nd-rich regions, eventually reaching a checkerboard pattern at the equilibrium states. Fig. I.5(c) and (d) clearly show the development of checkerboards with Li concentration.

The reason forming the unique pattern is mainly because of the ionic size difference between Li^+ and Nd^{3+} . For an ideal perovskite structure, the ion sitting at the center should be coordinated with twelve oxygen atoms. Ti^{4+} is relatively small so that it reduces the oxygen coordination by cooperative distortion of TiO_6 octahedra. This distortion is enough to satisfy the coordination preference of Nd^{3+} ion. In contrast, Li^+ ion has to undergo a remarkable displacement to further low the number of oxygen coordination to four, forming a square window site. The only choice to accommodate both ions is to go through phase separation into $\text{Nd}_{1/2}\text{Li}_{1/2}\text{TiO}_3$, in which Li^+ layers alternately stack with Nd^{3+} layers, and $\text{Nd}_{2/3}\text{TiO}_3$ without the presence of Li^+ . The high mobility of Li^+ and vacancies significantly facilitates the ion diffusion to form the specific pattern. This demonstrates a potential way to fabricate highly ordered 2D nanostructures by the conventional solid state reaction [13].

5. Checkerboards in the Polycrystalline ZnMnGaO_4

Jahn-Teller (JT) ions such as Mn^{3+} or Cu^{2+} sitting at octahedral sites have strong tendency to cluster together leading to structure distortion. This JT distortion tends to

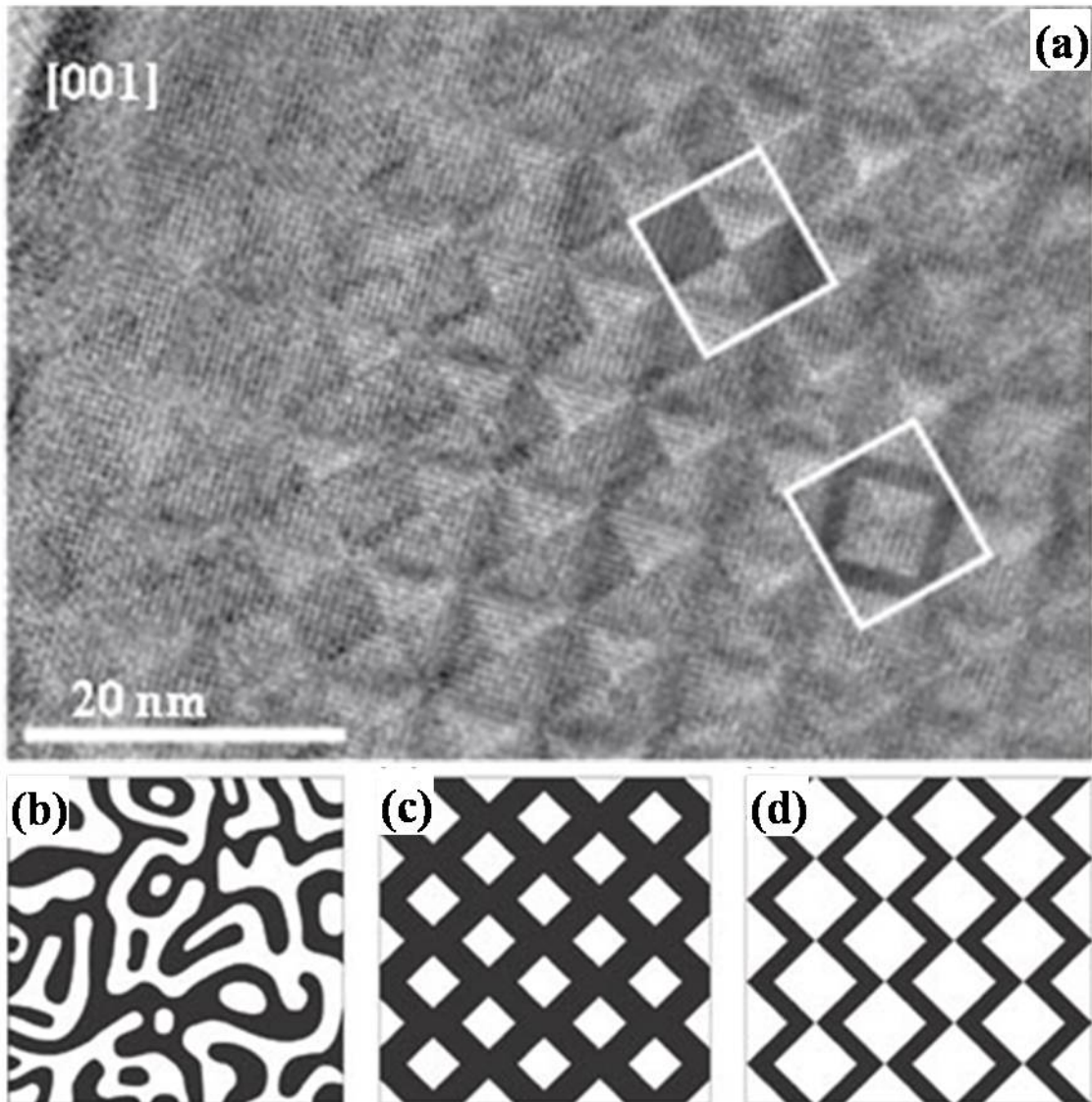


FIG. I.5. (a) TEM image of polycrystalline $(\text{Nd}_{0.53}\text{Li}_{0.43})\text{TiO}_3$ shows chessboard-type phase separation. (b) A typical spinodal decomposition (c) and (d) The phase separation in $(\text{Nd}_{2/3-x}\text{Li}_{3x})\text{TiO}_3$ with $x \approx 0.05$ and ≈ 0.12 . The black region is Li-poor and the white region Li-rich [13].

induce an ionic phase separation of the JT ions, resulting in spatially separated regions with higher and lower JT ion concentrations. Utilizing this ionic phase separation tendency induced by the JT effect, we have fabricated highly ordered nanostructures in the spinel ZnMnGaO_4 (ZMGO) [14].

ZMGO is a mixture of two normal spinels: cubic ZnGa_2O_4 and tetragonal ZnMn_2O_4 . The quenched parent compound ZMGO is cubic. While slowly cooling down, it undergoes a cooperative JT transition below ~ 1323 K and separates into cubic $\text{ZnMn}_{0.5}\text{Ga}_{1.5}\text{O}_4$ and tetragonal $\text{ZnMn}_{1.7}\text{Ga}_{0.3}\text{O}_4$ phases. These two phases form two types of long nanorods with the $\sim 4 \times 4 \times 70$ nm³ size (Fig. I.6(c)), alternatively stacking in a way that the cross sectional view is checkerboard-like (Fig. I.6(a)) and side view is herringbone-like (Fig. I.6(b)).

Fig. I.6(a) and (b) are the bright field TEM images of the 5 °C/h-cooled ZMGO with the incident beam parallel to [100] and [111] directions of the cubic phase, respectively. The CB regions, denoted as “A” in Fig. I.6(a), becomes HB patterns (Fig. I.4(b)). This confirms that the regions actually are the same nanodomains but with different view angles.

As we see from the above two pictures, the fundamental blocks are nanorods with CB cross sections. A schematic view of the nanorods stacking is shown in Fig. I.6(c). The tetragonal domains (more precisely, orthorhombical (O) phases) orientate in two different directions which are closely related with the Mn^{3+} orbital ordering as shown in Fig. I.7 [7].

6. Checkerboards in the ZnMnGaO_4 Thin Film

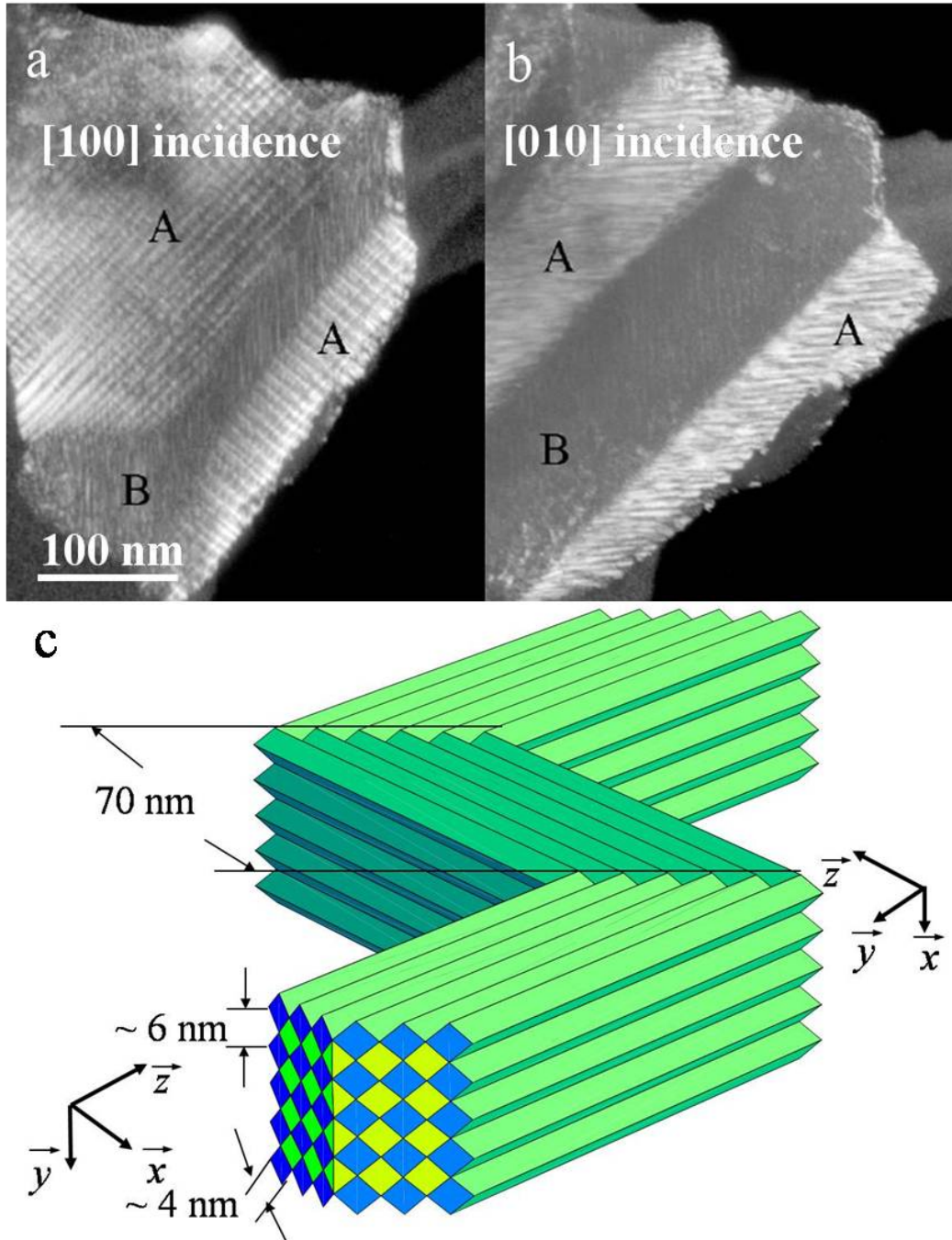


FIG. I.6. (a) and (b), TEM images with the relative sample orientation of $\sim 90^\circ$. The checkerboard domain denoted as “A” in the [100] incidence image displays a herringbone pattern for the [010] incidence, demonstrating that the checkerboard and herringbone images are different angular views of the same nanoscale object. (c) A schematic representation of two (110) twin-related colonies of a CB structure, where yellow regions show cubic phase; blue regions tetragonal equilibrium phase with different orientations [14].

Followed by the discovery of highly ordered nano CBs in ZnMnGaO_4 polycrystalline samples, unprecedented ordered array of nanorods ($\sim 4 \times 4 \times 750 \text{ nm}^3$) with the same composition are vertically fabricated on a (001) cubic MgO substrate by the pulsed laser deposition (PLD) technique as demonstrated in Fig. I.8. Fine fringes perpendicular to the substrate surface is shown in Fig. I.8(a), indicating the formation of well organized nanorods. The magnification of the nanorods from side view is illustrated in Fig. I.8(d). The top view of nanorods (Fig. I.8(c)) reveals CB pattern composed by orthorhombic and tetragonal phases [15].

A schematic view of the two phases vertically packing on the substrate is shown in Fig. I.8(b). This amazing architecture shows almost an ideal prototype of the patterned recording medium. Although tremendous effort has been paid to fabricate self-assembled structures in oxide films by PLD, highly ordered phases with different chemical compositions have not been achieved yet [16]. On the other hand, the relevant length scale is above 30 nm, which is too large to serve as high capacity media. The nanorods ($\sim 750 \text{ nm}$) in our ZnMnGaO_4 film are ten times longer than that in our polycrystalline sample ($\sim 70 \text{ nm}$). This clearly indicates that the shape anisotropy of the nanorods might be tunable with external strain by changing the length of HBs in a broad range from nano to micro scale. The successful fabrication of CB pattern on film is a robust evidence of the possibility to exploit it as an ultrahigh density recording medium if one phase was ferromagnetic while another paramagnetic.

The deformation of Mn-poor phase from cubic to tetragonal and Mn-rich phase from tetragonal to orthorhombic is due to the coherent strain among the phases. The symmetry lifting observed in the above experiment is well consistent with the prediction by the 3D

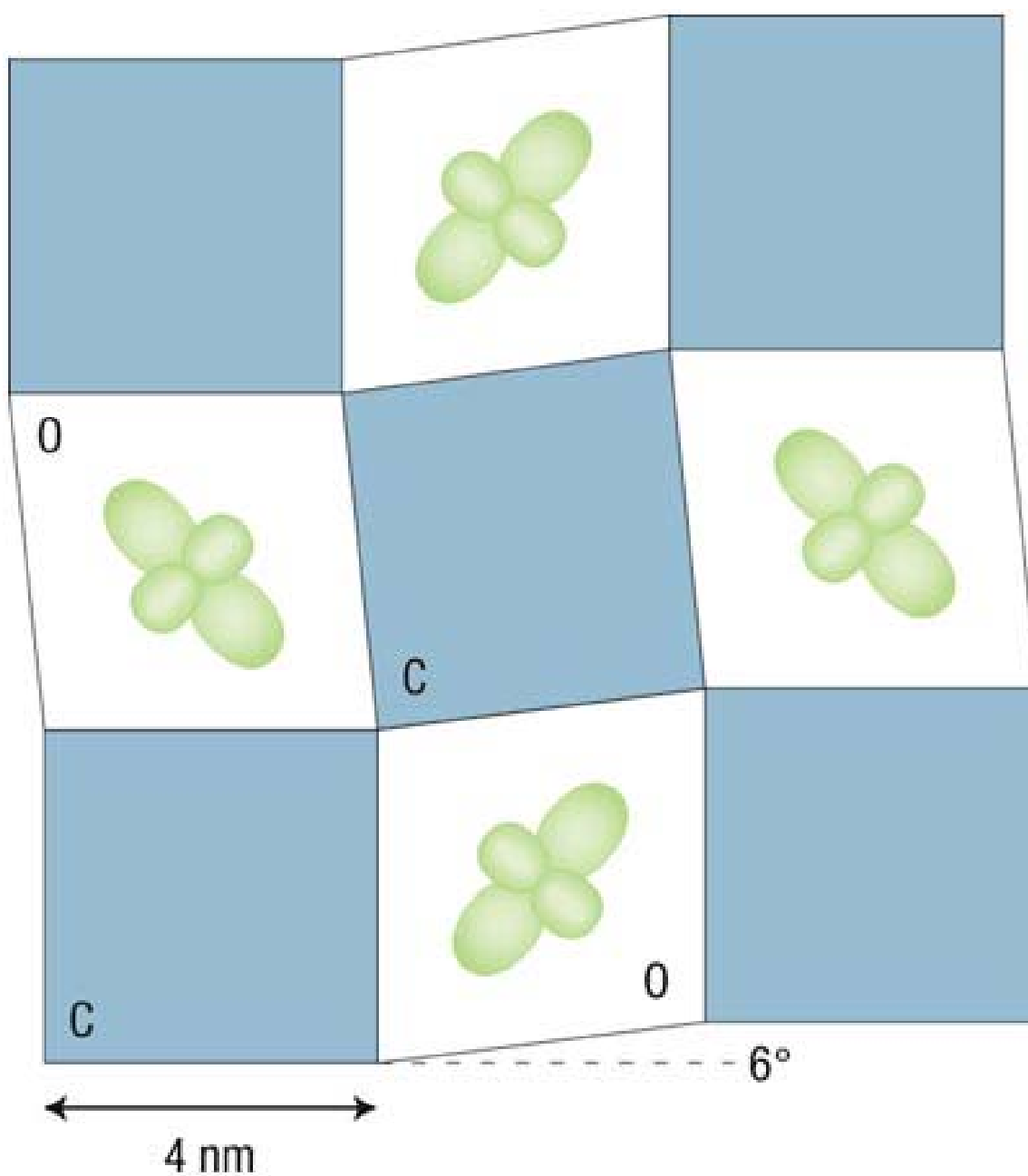


FIG. I.7. A schematic view of the ordering of cubic and orthorhombically distorted (O) phases. Two O-type rods, having two different directions of Mn orbital order, and two C-type rods with a relative 6° rotation, stack in the checkerboard pattern [7].

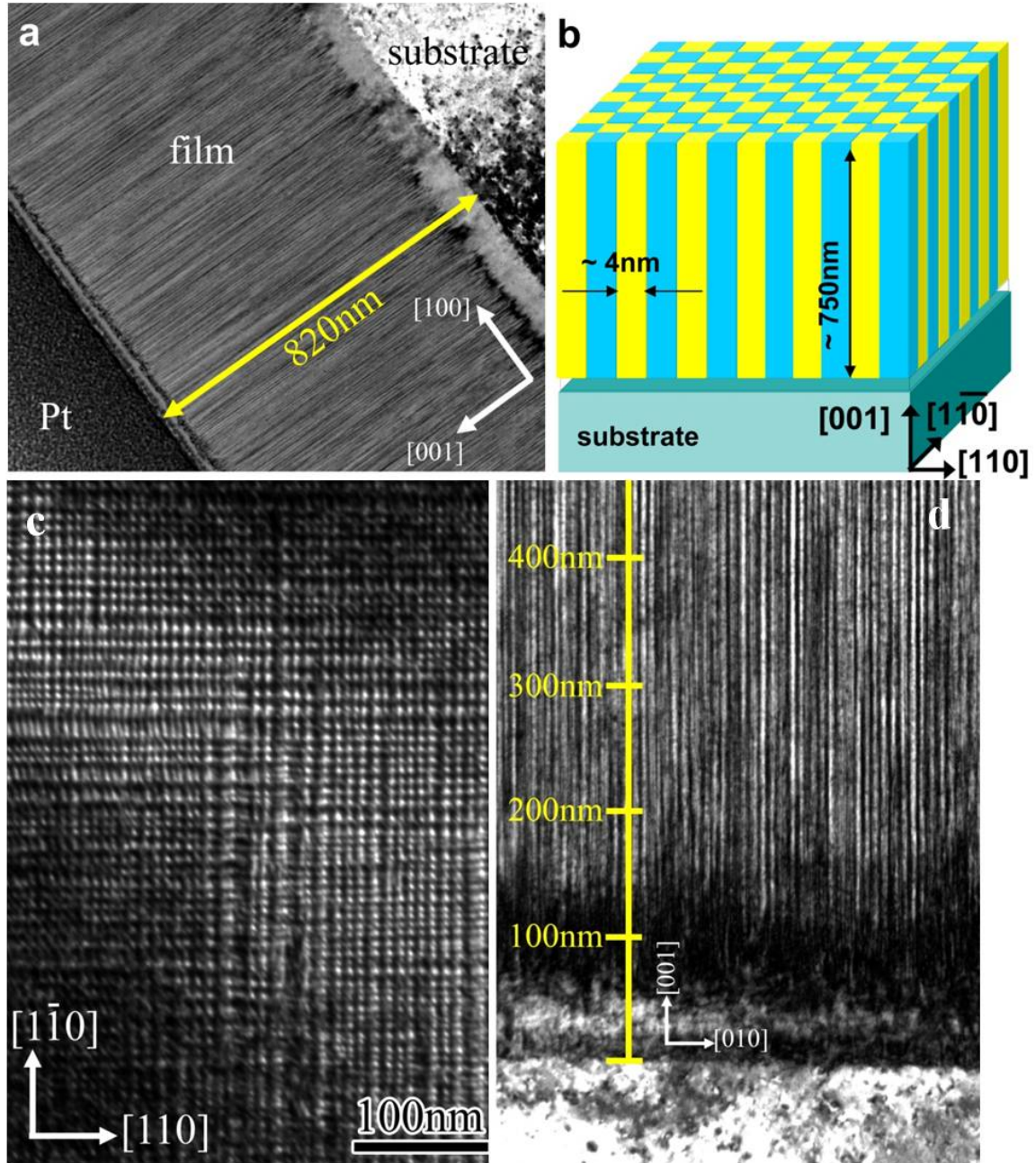


FIG. I.8. A self-assembled nanocheckerboard ZnMnGaO_4 film grown on a (001) MgO substrate. (a) TEM side-view image of the spinel film at low magnification. The picture is normal to the (010) axis. Pt is used for a capping layer for focused ion beam (FIB) sample preparation. (b) Schematic picture of a well-oriented nanorod spinel film formed on a substrate. The nanorods are aligned along the $[001]$ direction. (c) A TEM dark field image near the top surface showing a checkerboard domain. (d) A TEM right field side-view image near the MgO substrate showing the nanostructured film, a thin transition layer, and the substrate, from top to bottom [15].

PFM model which will be stated in detail in the Chap. 3 [4]. By the synchrotron radiation X-ray diffraction, it further observes that the out-of-plane lattice parameters of the two phases are identical [17]. This is also good agreement with the prediction of the model.

7. Background of the Perpendicular Recording

Perpendicular recording is widely viewed as the next generation of recording [18]. The areal density could be 10 times larger than that of longitudinal recording. As shown in Fig. I.9, the data bits are packed vertically, perpendicular to the disc. Therefore, each bit takes less space on the surface area of a disc. More bits can be squeezed in per square inch and allow higher storage capacity compared with the conventional longitudinal recording. The magnetization of adjacent bits stands in an opposite direction. In terms of energy, the adjacent bits attract each other and are more favorite to overcome thermal fluctuation. It is predicted that the areal density could be pushed up to 1 Tbit/inch² by the perpendicular recording. Actually, because of the limitation of write field, it is really challenging to achieve this goal.

Patterned magnetic recording is superior to any recording methods. In patterned media, the magnetic islands are created as an ordered array with high uniformity and isolated from each other. Each island represents an individual bit; in the conventional media, the bits composed by many grains form a mosaic and are randomly distributed on the disc. With patterned media recording, the areal density could be extended 50 Tbit/inch² assisted with heat-assisted magnetic recording (HAMR) technique.

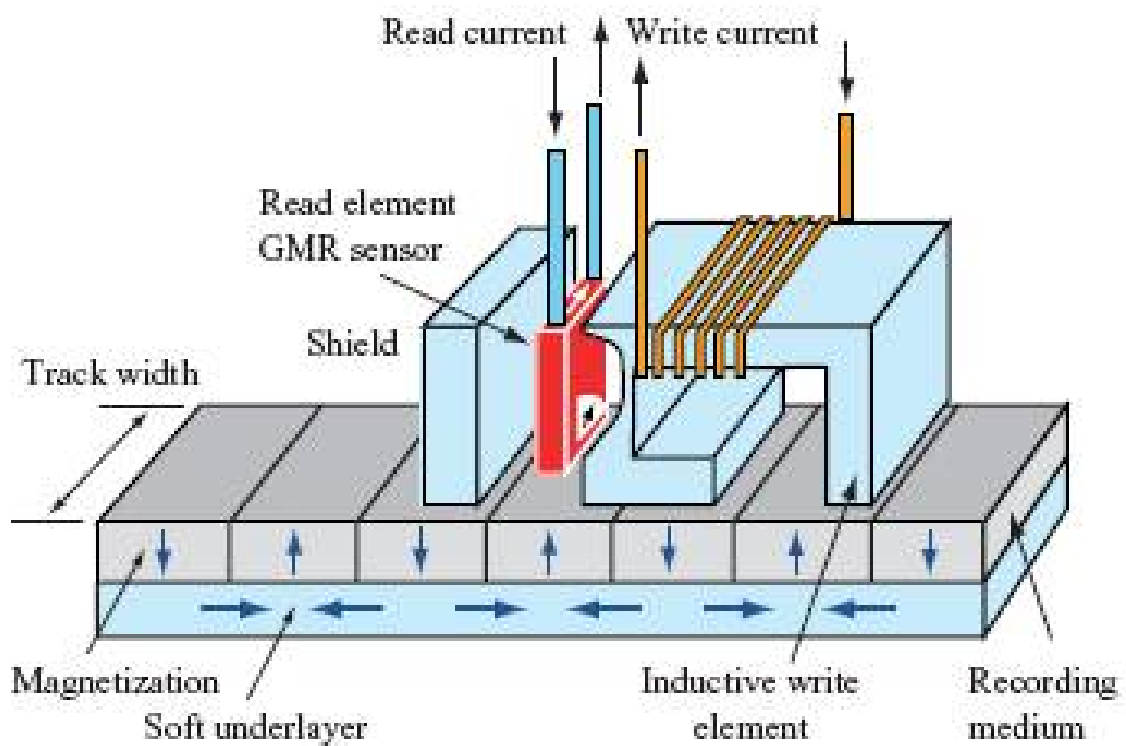


Fig. I.9. A schematic view of the perpendicular recording method [18].

Global efforts in nano-science have been launched to fabricate and characterize ever-smaller structures and exploit their properties for miniaturized technological devices. The central challenge of these diverse initiatives is the fabrication of nanoscale structure/assembly with well-controlled architectures. Two general strategies have been adopted here: high-resolution lithography (top-down) and nanoscale self-assembly (bottom-up). However, none of them is economical enough to massively manufacture [19-22].

8. Conclusion

Nanoscale Phase separation in oxides has been briefly reviewed. Although the simultaneous formation of checkerboard-like microstructure associated with phase separation has been observed in several systems especially in alloys such as Co-Pt, Ni-V, etc. even in natural mineral [3,23,24], it is a rare case to form highly ordered nanostructures constituted by two or multiple phases with different chemical compositions in oxides.

Different from whatever so-called checkerboard patterns observed before, several points of the CBs achieved in ZnMnGaO_4 both polycrystal and film are deserved to be addressed. First, they are truly checkerboards in terms of the rectangular shapes of the components. Second, the 3D structure might be superior to the 2D structure in the analog and digital communications, in which signal-to-noise ratio (SNR) is a measure of the signal strength relative to the background noise. It is critical to preserve certain number of grains in a bit to suppress the noise since $\text{SNR} \sim \log_{10}(N)$, where N is the number of grains in a bit. Higher density requires to reduce the volume (V) of each grain in a bit.

Decreasing the grain size will unavoidably encounter the above thermal stability condition [21]. For our CBs, even though the size is only a few nanometers far below or close to the threshold of superparamagnetism (10 nm), the overall volume is big enough to accommodate a large number of atoms because of the tunable length of HBs. Additionally, the large shape anisotropy of the nanarods will assist to overcome the instability caused by the thermal activation.

The most meaningful point of discovering the nanostructure in ZGMO is that it demonstrates an alternative way, except top-down and bottom-up methods, to fabricate highly self-organized patterns in Mn-based spinels. Ordered nanostructures can be synthesized through the conventional solid state reaction. The subsequent fabrication of this spectacular pattern on the thin film is a robust evidence to make it potentially applicable in the ultrahigh density medium recording. Impressively, the length of the nanorods in thin film could be facilely controlled by the thickness of films. What we will see in the Chap. 4 is that the cross section, in other words the sizes of CB, actually can also be broadly controlled by the isothermal annealing time and compositions in other magnetic systems.

Unfortunately, the two separated phases in ZnMnGaO_4 spinel system are nonmagnetic, not much directly related with magnetic application. In the magnetic recording, it is important to decouple the magnetization of magnetic domains and control each of them independently by applying an external magnetic field. The ideal case is to have one separated phase ferromagnetic and another nonmagnetic at room temperature. Hereby, searching systems characterized with this feature will be our main focus in this

thesis. We will discuss two magnetic Mn-based MgFe_2O_4 and CoFe_2O_4 spinel systems in detail.

9. References

- [1] A. G. Khachaturyan, *Theory of Structural transformations in solids* (Wily, New York, 1983).
- [2] N. Vladimirova, A. Malagoli and R. Mauri, *Phys. Rev. E.* **60**, 6968 (1999).
- [3] Y. Le. Bouar, A. Loiseau, A. G. Khachaturyan, *Acta Mater*, **46**, 2777(1998).
- [4] Y. Ni, and A. G. Khachaturyan, *Acta Mater* (2008), doi:10.1016/j.actamat.
- [5] E. Dagotto, *Science* **309**, 257 (2005).
- [6] Y. Tokura and N. Nagaosa, *Science* **288**, 462 (2000).
- [7] S. W. Cheong, *Nat Mater* **6**, 928 (2007).
- [8] Y. Tokura, *Rep. Prog. Phys.* **69**, 797 (2006).
- [9] Y. Tokura, *Phys. Today* **56**(7), 50 (2003).
- [10] E. Dagotto, *Nanoscale Phase Separation and Colossal Magnetoresistance*, Springer, Berlin (2003).
- [11] M. Uehara, S. Mori, C. H. Chen and S.-W. Cheong, *Nature*, **399**, 560 (1999).
- [12] C. N. R. Rao, P. V. Vanitha, and A. K. Cheetham, *Chem, Eur. J.* **9**, 828 (2003).
- [13] B. S. Guiton and P. K. Davies, *Nat. Mater* **6**, 586 (2007).
- [14] S. Yeo, Y. Horibe, S. Mori, C. M. Tseng, C. H. Chen, A. G. Khachaturyan, C. L. Zhang, and S.-W. Cheong, *Appl. Phys. Lett.* **89**, 233120 (2006).

- [15] S. Park, Y. Horibe, T. Asada, L. S. Wielunski, N. Lee, P. L. Bonanno, S. M. O'Malley, A. A. Sirenko, A. Kazimirov, M. Tanimura, T. Gustafsson, and S.-W. Cheong, *Nano Lett* **8**, 2, 720 (2008).
- [16] H. Zheng, J. Wang, S. E. Lofland, Z. Ma, L. Mohaddes-Ardabili, T. Zhao, L. Wuttig, Salamanca-Riba, S. R. Shinde, S. B. Ogale, F. Bai, D. Viehland, Y. Jia, D. G. Schlom, M. A. Roytburd, and R. Ramesh, *Science* **303**, 661 (2004).
- [17] S. M. O'Malley, P. L. Bonanno, K. H. Ahn, A. A. Sirenko, A. Kazimirov, S. Park, and S-W. Cheong, arXiv:0804.1973v1
- [18] D. A. Thompson and J. S. Best, *IBM J. Res. Develop.* **44**(3),311 (2000).
- [19] J.V. Barth, G. Costantini and K. Kern, *Nature* **437**, 671 (2005).
- [20] S. H. Charap, L. P. Lu, and Y. He, *IEEE Trans. Magn.* **33**, 978 (1997).
- [21] D. Weller and A. Moser, *IEEE Trans. Magn.* **35**, 4423 (1999).
- [22] T. W. McDaniel, *J. Phys.: Condens. Matter* **17**, R315 (2005).
- [23] A.Suzuki and M.Takeyama: *J. Mater. Res.*, **21**, 21(2006).
- [24] R. J. Harrison, R. E. Dunin-Borkowski, and A. Putnis, *PNAS* **99**, 16556(2002).

Chapter II

Nanostructure in the Magnetic Spinel $\text{Mg}(\text{Mn,Fe})_2\text{O}_4$

1. Introduction

The electronic degeneracy of ions such as Mn^{3+} or Cu^{2+} can be lifted by a Jahn-Teller (JT) distortion, when the electronic energy gain can overcome the structural energy cost [1]. This JT effect can be associated with intriguing physical phenomena such as the colossal magnetoresistance effect in perovskite manganites and high temperature superconductivity in layered cuprates [2-7]. Furthermore, the JT effect can couple to chemical phase separation by inducing a miscibility gap in the system with mixed JT and non-JT ions, leading to spatially separated regions with higher and lower JT ion concentrations [8,9]. One extraordinary example of JT-induced phase separation was observed in the spinel $\text{Zn}(\text{Mn,Ga})_2\text{O}_4$ (ZMGO), where a truly nanoscale and well ordered structure is stabilized by the phase separation. The nano-structure consists of two types of long square rods ($\sim 4 \times 4 \times 70 \text{ nm}^3$) with different Mn concentrations that are alternatively stacked with long-range periodicity, and thus its cross section shows a checkerboard (CB) pattern [10]. Crystallographically, the nano-CB of ZMGO is truly remarkable, but does not constitute a technological advance in a “magnetic” sense, because ZMGO is basically paramagnetic (PM) near room temperature [11,12].

Since “ferrimagnetic (FM)” spinel compounds are abundant [13], one can contemplate forming a nano-CB structure with two types of nano-rods having distinct magnetic properties, ideally with one of them having a FM transition above room temperature. Such a magnetic nanostructure with large shape anisotropy is potentially useful as a medium for perpendicular magnetic recording [14,15]. Keeping this in mind, we have investigated many FM spinels with partial Mn concentrations, and found that the nanostructures are common in mixed spinels with proper heat treatments. Herein, we

report the realization of the magnetic nanostructure in $\text{Mg}(\text{Mn,Fe})_2\text{O}_4$. We also discuss the structural evolution of $\text{Mg}(\text{Mn,Fe})_2\text{O}_4$ as well as the change of magnetic properties with various chemical compositions and cooling rates (CR). MgFe_2O_4 is FM with Curie temperature (T_C) of ~ 600 K, while MgMn_2O_4 is PM down to low temperatures [16,17]. In addition, MgFe_2O_4 crystallizes in a cubic structure ($Fd3m$) with $a \approx 8.52$ Å [18], but MgMn_2O_4 is tetragonal ($I4_1/amd$; due to cooperative JT distortions) with $a \approx 5.75$ Å and $c \approx 9.38$ Å [17]. This tetragonality in MgMn_2O_4 reflects the presence of cooperative JT distortions. Both of them are partially inverse spinels, meaning that some of the Fe and Mn ions in $\text{Mg}(\text{Mn,Fe})_2\text{O}_4$ are located in tetrahedral A sites [13,16-19].

2. Experimental Method

A dozen $\text{MgMn}_x\text{Fe}_{2-x}\text{O}_4$ specimens were prepared by conventional solid state reaction. Stoichiometric amounts of MgO , Mn_2O_3 , and Fe_2O_3 powders were mixed and sintered at 1050-1250 °C three times with intermediate grindings. The final cool-down from 1250 °C to room temperature was performed with various CR, ranging from quenching in cold water to 0.3 °C/h-cooling. Crystallographic structures were examined using a Rigaku x-ray diffractometer (XRD) at room temperature. A SQUID magnetometer was used for magnetization measurements and standard four-probe resistivity (ρ) experiments were performed. Bright field images were taken using a JEOL 2000FX transmission electron microscope (TEM) at 200 kV, equipped with a 14-bit charge-couple-device array detector.

3. Result and Discussion

Fig. II.1(a) demonstrates that the CR drastically influences the magnetic hysteresis loop at 5 K for $x = 1.5$. The coercivity (H_c) of the 50 °C/h-cooled specimen is $\sim 4,700$ Oe, which is about 25 times larger than that of the quenched one ($H_c \approx 187$ Oe). The plot of H_c vs CR reveals that the 50 °C/h-cooled specimen exhibits the maximum H_c (see the inset of Fig. II.1(a)). Fig. II.1(b) displays that the XRD patterns for $x = 1.5$ significantly change with varying CR, suggesting that the H_c change is associated with the structural modification. The XRD pattern for the quenched specimen shows a pure cubic phase. However, the structure of the 50 °C/h-cooled specimen is purely tetragonal, and this clean tetragonality indicates a cooperative JT distortion in the entire specimen. The cubic nature of the quenched specimen may reflect that the quenching is faster than the kinetics needed to support the cooperative JT distortion. Note that in the quenched cubic specimen, there may be a significant amount of Mn ions in the A sites, which are not JT-active. These non-JT-active Mn ions also contribute to the absence of cooperative JT distortions in the quenched specimen [20-23]. In contrast, the 10°C/h-cooled specimen shows the mixture of cubic and tetragonal phases, stemming from the chemical phase separation with the clustering of the JT Mn ions in the octahedral B sites. Still slower cooling, 0.3 °C/h, produces a more distinct phase separation between the cubic and tetragonal phases.

In order to conveniently discuss the structural change for $x = 1.5$, we introduce a few notations. C' and T' are for the cubic phase of the quenched specimen and the tetragonal phase of the 50 °C/h-cooled one, respectively. Both of them are metastable, and slower cooling than 50 °C/h induces the decomposition of T' into a mixture of cubic (C) and tetragonal (T) phases. Mn concentrations in C' and T' are identical. However, Mn

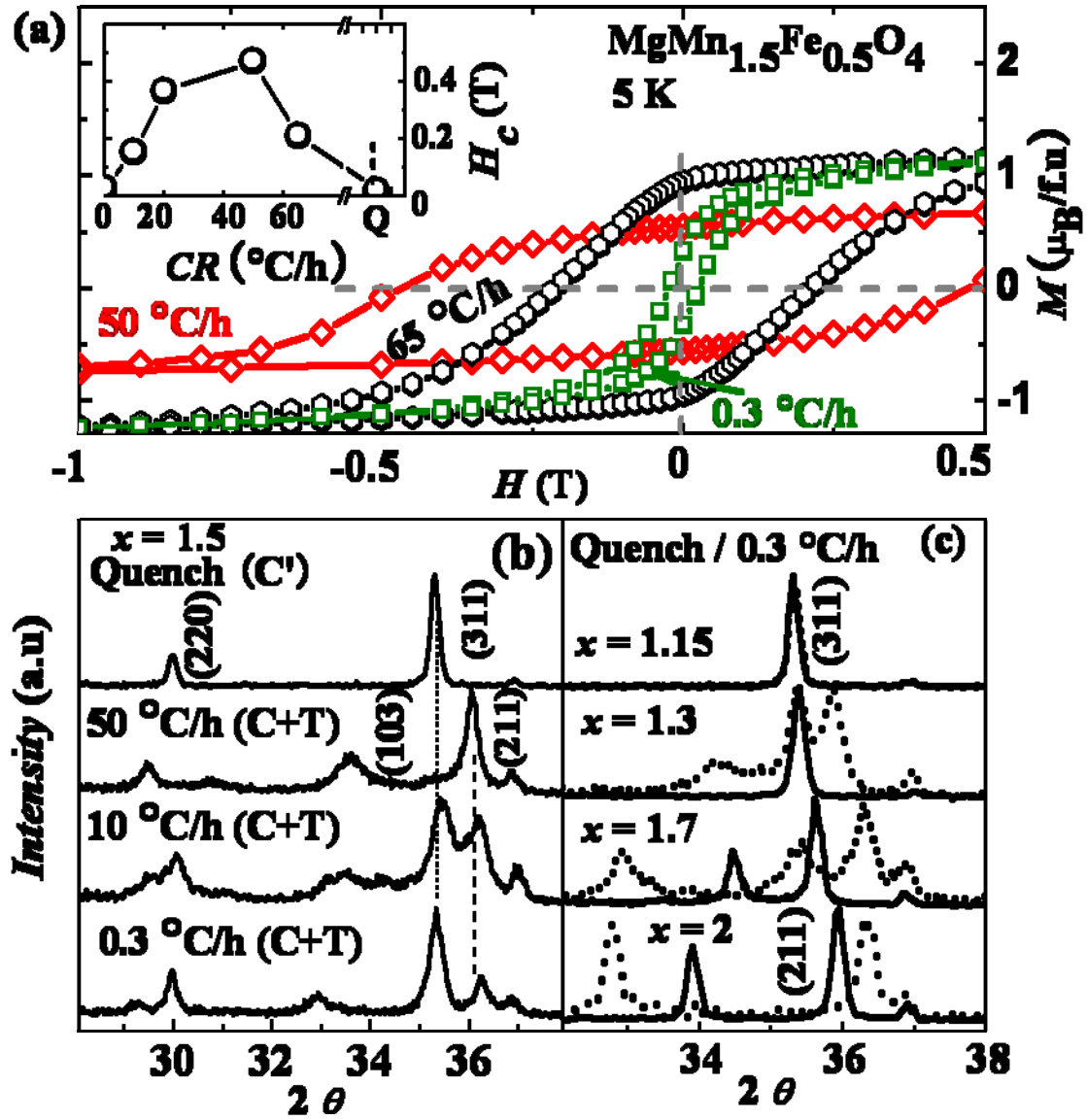


FIG. II.1. (a), M vs H at 5 K for $x = 1.5$ with selected CR's. The inset displays magnetic coercivity vs. CR. Q represents quenching in cold water. (b), XRD patterns at room temperature for $x = 1.5$ with selected CR's. C' represents the cubic phase of the quenched specimen, and the cubic XRD peaks of (220) and (311) are denoted. T' represents the tetragonal phase of the 50 °C/h-cooled specimen, and the tetragonal XRD peaks of (103) and (211) are denoted. C and T represent the cubic and tetragonal phases after phase separation, respectively. (c), XRD patterns of the quenched (solid line) and 0.3 °C/h-cooled (dashed line) specimens of selected Mn concentrations.

concentration in T (C) is presumably more (less) than that in T' . Consistently, the tetragonality of T is larger than that of T' , as evidenced in the XRD results. Using these notations, the structural evolution can be simplified as $C' \rightarrow T' \rightarrow C + T$ with decreasing CR. From extensive XRD studies, we have confirmed that other compositions in the miscibility gap region show a similar structural evolution by varying CR, and that C and T are the miscibility boundary compounds with compositions $\text{MgMn}_{1.2}\text{Fe}_{0.8}\text{O}_4$ and MgMn_2O_4 , respectively (see below).

A large H_c can be achieved by hindering the nucleation and growth of magnetization reversed domains through pinning of domain walls or increasing magnetic anisotropy [24,25]. The magnetic anisotropy can originate from various sources such as magnetocrystalline, shape, magnetoelastic, interface, and exchange anisotropies. [24-29]. Magnetocrystalline anisotropy (MA) is commonly utilized to suppress the magnetization rotation. Presumably, C' , T' and C are ferrimagnetic, and T is paramagnetic. It is expected that the MA in the tetragonal T' phase is large and in the cubic C and C' phases, is negligible. Thus, T' has the largest H_c , and the shape anisotropy of the C domains is presumed to be the main contribution to the coercivity of the $C+T$ specimens.

Fig. II.1(c) shows the XRD patterns of the quenched and 0.3 °C/h-cooled specimens for various concentrations. The $x = 1.15$ pattern does not change with varying CR. However, for $x = 1.3$, the 0.3 °C/h-cooled specimen (dashed line) displays a totally different XRD pattern from that of the quenched one (solid line), indicating that $x = 1.2$ is close to one of the miscibility gap boundaries. The quenched specimens of $1.7 \leq x \leq 2$ are tetragonal (i.e. T') while the quenched specimens of $1.2 < x < 1.7$ are cubic (i.e. C'). These results suggest that the kinetics for the cooperative JT transition for

$1.7 \leq x \leq 2$ (i.e. high Mn concentration) is faster than the quenching speed while that for $1.2 < x < 1.7$ is slower than the quenching speed. The 0.3°C/h -cooled $x = 1.7$ does exhibit the C-T phase separation, indicating that the other miscibility gap boundary is close to $x = 2$.

Based on the results of XRD, high temperature resistivity, and magnetization experiments, the phase diagram for $\text{MgMn}_x\text{Fe}_{2-x}\text{O}_4$ (see Fig. II.2(a)) has been constructed. The miscibility gap exists for $1.2 < x < 2$ [30]. The resistivity anomaly with thermal hysteresis in the inset of Fig. II.2(a) originates from the 1st-order JT phase transition. The JT transition temperature upon warming (\triangle) and cooling (∇) and the Curie temperature (T_C) for the quenched (\circ) and 5°C/h -cooled specimens (\square) are determined from sharp features in $d(\ln\rho)/dT$ and $d\chi/dT$, respectively. For $1.2 < x < 2$, the T_C 's of the 5°C/h -cooled specimens are almost independent of x . This is in good agreement with the picture that only the amount, not chemical composition, of the C phase changes with x in phase separated specimens and that the T_C is the ferrimagnetic transition of the C phase after phase separation. On the other hand, the T_C of the quenched specimens decreases monotonically with increasing x . Fig. II.2(b) displays how T_C (\blacklozenge) and H_c (\redlozenge) of $x = 1.5$ changes with CR. The T' (50°C/h) specimen exhibits the maximum H_c and the minimum T_C . Cooling slower than 50°C/h produces the mixture of C and T, so that T_C of the mixture, fixed by that of C, is higher than that of C' and T' . The slower cooling of $\text{CR} < 50^\circ\text{C/h}$ generates a higher T_C due to the further phase separation with larger length scale. The temperature dependence of M/H of $x = 1.5$ for various CR's is shown in the inset of Fig. II.2(b).

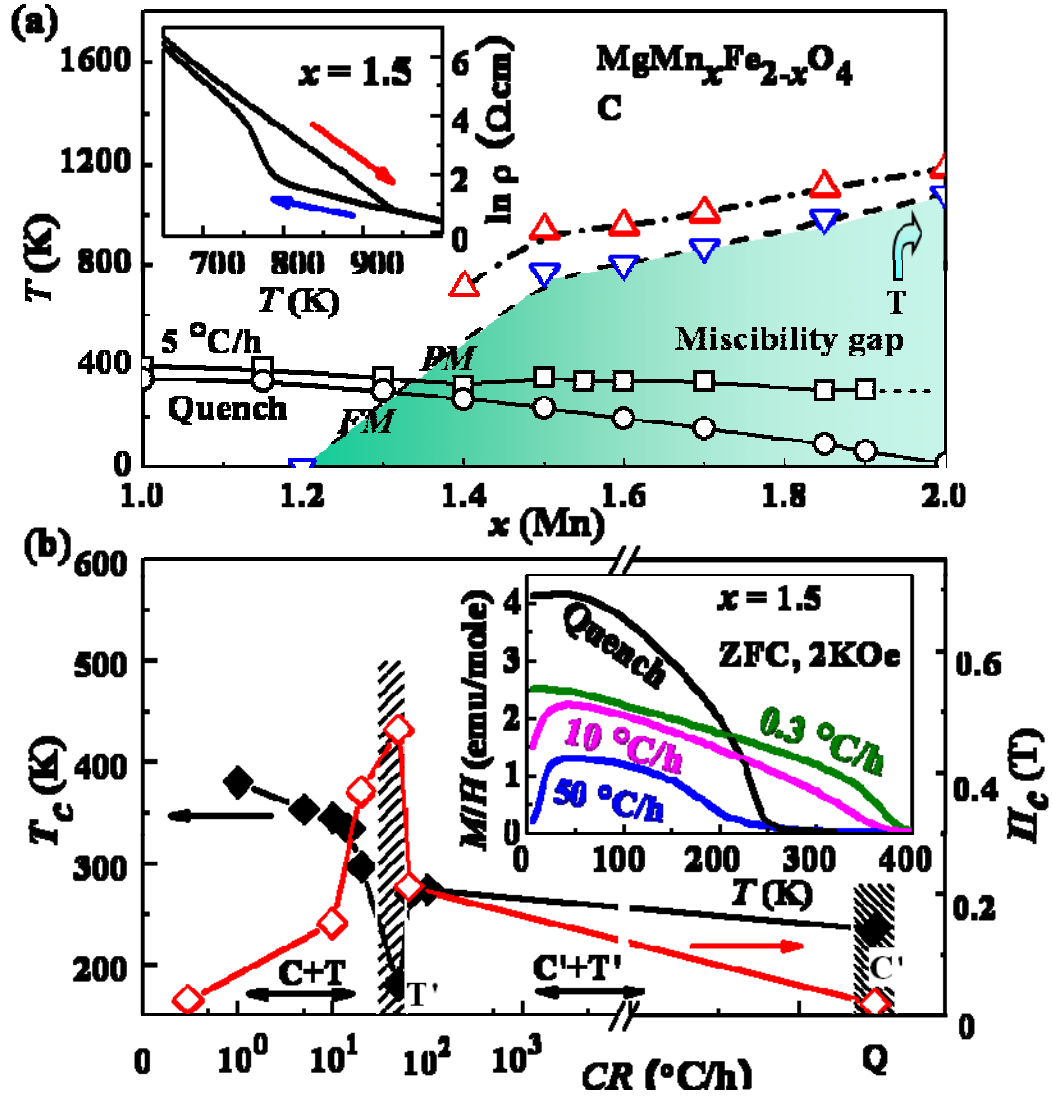


FIG. II.2. (a), Phase diagram of $\text{Mg}(\text{Mn}, \text{Fe})_2\text{O}_4$. Colored area depicts the miscibility gap region in the 5 °C/h-cooled specimens. Arrow denotes the tetragonal T phase of $x=2$. \triangle and ∇ denote the JT transition temperature, T_{JT} , upon warming and cooling, respectively, determined from high-temperature resistivity measurements. \square and \circ denote ferrimagnetic T_C of the 5 °C/h-cooled and quenched specimens, respectively. PM and FM stand for paramagnetic and ferrimagnetic, respectively. The inset displays logarithmic resistivity vs. temperature upon warming (red) and cooling (blue) for $x=1.5$. (b), T_C (\blacklozenge) and coercivity ($\color{red}\lozenge$) vs. logarithmic CR for $x=1.5$. Lines are drawn for guides to the eyes. The mixture of C+T forms for very slow CR (the most left region). The shaded areas at the left and right hand sides represent the regions for the T' and C' phases, respectively. Between the shaded regions, mixed C'+T' is observed. The inset displays the temperature dependence of zero field-cooled M/H in $H=2$ KOe for $x=1.5$ with selected CR's.

$M(H)$ curves at selected temperatures for the 50 °C/h-cooled $\text{MgMn}_{1.5}\text{Fe}_{0.5}\text{O}_4$ are shown in Fig. II.3(a), and H_c and remnant magnetization (M_r), obtained from $M(H)$ curves, are displayed in Fig. II. 3(b). Interestingly, H_c increases abruptly below ~ 30 K. This up-turn of H_c below ~ 30 K is apparently related with the down-turn of M/H below ~ 30 K (Fig. II.3(c)).

In analogy with the observation in the 5 °C/h-cooled ZMGO [10], our TEM results show that the 10 °C/h-cooled $x = 1.5$ specimen displays checkerboard (CB) and herringbone (HB) patterns with a few nanometers in size as shown in Fig. II.3(d) and (e). As explained in Ref. 10, the CB and HB patterns are the cross sectional and side views of the self-assembled nano-rods, respectively. The results in Ref 10 along with our results of TEM, XRD and magnetic measurements on $x = 1.5$ indicate that the self-assembled nanostructure consists of two types of square nano-rods with distinct magnetic properties: the cubic-phase (C) rods are ferrimagnetic, and the tetragonal-phase (T) rods are paramagnetic. (Note that the T rods can be orthorhombically-distorted as discussed in Ref 10.) The unique self-assembly is spontaneously formed during the coherent spinodal decomposition into non-JT Fe^{3+} -rich (cubic) and JT Mn^{3+} -rich (tetragonal) phases through accommodating elastic strain induced by the lattice misfit of the two precipitated crystallographically-distinct phases [10,31-33]. Since the miscibility gap occurs for $1.2 < x < 2$, the chemical compositions of the C and T rods are expected to be $\text{MgMn}_{1.2}\text{Fe}_{0.8}\text{O}_4$ and MgMn_2O_4 (i.e. the miscibility gap boundaries), respectively. The lever rule for $x = 1.5$ indicates that the total volume of the C rods is

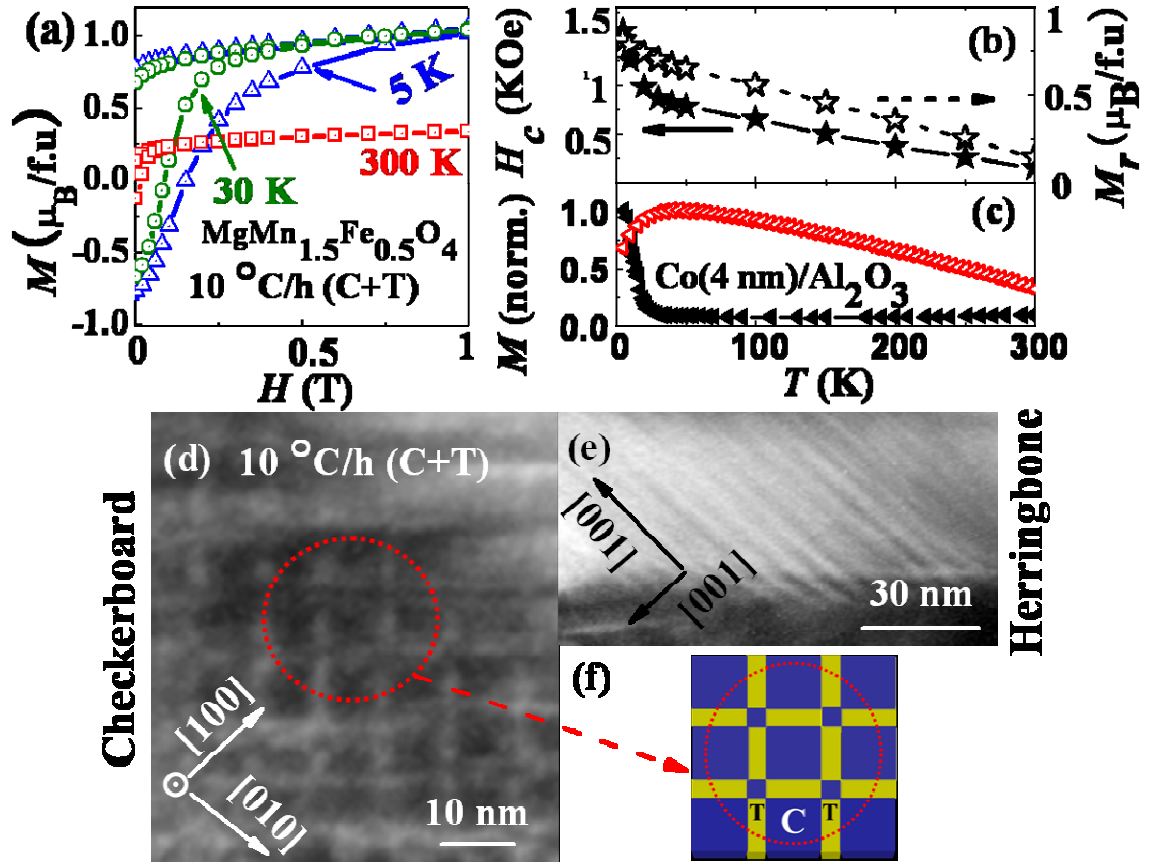


FIG. II.3. (a), M vs. H of the 10°C/h -cooled $\text{MgMn}_{1.5}\text{Fe}_{0.5}\text{O}_4$ at selected temperatures. (b), H_c (\star) and M_r (\star) vs. temperature. (c), Magnetization vs. temperature of the 10°C/h -cooled $\text{MgMn}_{1.5}\text{Fe}_{0.5}\text{O}_4$ (\blacklozenge) and 4 nano-meter size spherical Co particles embedded in Al_2O_3 matrix (\blacktriangleleft : from Ref. 29). Magnetization is normalized by the maximum value. (d) and (e), TEM images of the 10°C/h -cooled specimen, showing checkerboard and herringbone patterns, respectively. The arrows represent the crystallographic axes of the cubic spinel unit cell. (f), a schematic view of the circled region in (d). The blue and yellow regions represent the C and T phases, respectively.

larger than that of the T rods, which is consistent with the XRD results in Fig. II.1(b) and TEM images. A schematic view of the CB structure is depicted in Fig. II.3(f).

One of the main challenges to developing ultra high density magnetic recording media is associated with the so-called superparamagnetic limit, due to the destabilization of magnetization direction by thermal fluctuations [34,35]. As shown in Fig. II.3(c), spherical 4 nm-size Co particles embedded in Al_2O_3 (◀) show little magnetization above ~ 10 K [29]. In contrast, the 10 °C/h-cooled $x = 1.5$ (◀) exhibits a significant magnetization as well as magnetic coercivity in a wide temperature range, probably because of the large shape anisotropy of the C rods.

4. Conclusion

In conclusion, we have investigated how the JT distortions can influence the structural and magnetic properties, and induce a unique magnetically active nanostructure in $\text{Mg}(\text{Mn,Fe})_2\text{O}_4$ due to the clustering tendency of the JT-distorted Mn ions. There exists a strong tendency toward phase separation because of the clustering of the JT-distorted Mn ions, inducing a miscibility gap in this system. The kinetics for this phase separation, involving nano-scale ionic diffusion, is much slower than that for the JT distortions. With decreasing cooling rates of specimens in the miscibility gap region, the structural evolves as $C' \rightarrow T' \rightarrow C + T$. The phase-separated $C+T$ mixture, in fact, forms an intriguing nano-structure with only the C domains ferrimagnetic.

Meanwhile, the above work confirms the generality of the solid state reaction to fabricate nanostructures in Mn-based spinels no matter whether they are normal or inverse spinels. Especially, the formation of magnetic nanorods embedded in the

nonmagnetic counterparts significantly improves the magnetic properties such as coercivity. This indicates that the nanocheckerboard assembly with ferrimagnetic nanorods, can be suitable for a ultra high-density perpendicular magnetic storage medium [32,33,36]. Unfortunately, the nanocheckerboards are not organized as well as those observed in ZMGO. The distribution of nanocheckerboards is not homogenous throughout the entire grain. Most likely, it is ascribed to the difference in cationic size. The ionic size of Mg^{2+} (0.86 Å) is much bigger than those of Fe^{3+} (0.738 Å) and Mn^{3+} (0.753 Å). Their mobilities could be different. Since the formation of microstructure involves the substitutional diffusion of the three species of cations, the difference of mobilities will consequently cause inhomogeneity. Therefore, our next goal is to search for a magnetic system with a better organized microstructure. It will be discussed in the following chapter.

5. References

- [1] See, for example, Isaac Bersuker, *The Jahn-Teller Effect* (Cambridge University Press, Cambridge, 2006).
- [2] E. Dagotto, *Science* **309**, 257 (2005).
- [3] D. Louca, T. Egami, E. L. Brosha, H. Roder, A. R. Bishop, *Phys. Rev. B* **56**, R8475 (1997).
- [4] M. Uehara, S. Mori, C. H. Chen, S.-W. Cheong, *Nature* **399**, 560 (1999).
- [5] M. Fath, S. Freisem, A. A. Menovsky, Y. Tomioka, J. Asrts, and J. A. Mydosh, *Science* **285**, 1540 (1999).

- [6] L. Zhang, C. Israel, A. Biswas, R. L. Greene, and A. de Lozanne, *Science* **298**, 805 (2002).
- [7] G. Alvarez, M. Mayr, A. Moreo, E. Dagotto, *Phys. Rev. B* **71**, 014514 (2005).
- [8] M. A. Ivanov, N. K. Tkachev, and A. Ya. Fishman, *Low Temp. Phys* **28**, 613 (2002).
- [9] M. A. Ivanov, N. K. Tkachev, and A. Ya. Fishman, *Low Temp. Phys* **25**, 459 (1999).
- [10] S. Yeo, Y. Horibe, S. Mori, C. M. Tseng, C. H. Chen, A. G. Khachatryan, C. L. Zhang and S.-W. Cheong, *Appl. Phys. Lett* **89**, 233120 (2006).
- [11] A. S. Risbud, R. Seshadri, J. Ensling, and C. Felser, *J. Phys.: Condens. Matter* **17**, 1003 (2005).
- [12] S. Asbrink, A. Waskowska, L. Gerward, J. Staun Olsen and E. Talik, *Phys. Rev. B* **60**, 12651 (1999).
- [13] See, for example, F. S. Galasso, *Structure and properties of inorganic solids* (Pergamon Press, New York, 1970), Chap. **8**, p. 220-225.
- [14] D. A. Thompson and J. S. Best, *IBM J. Res. Dev* **44**, 311 (2000).
- [15] A. Moser, K. Takano, D. T. Margulies, M. Albrecht, Y. Sonobe, Y. Ikeda, S. Sun, and E. Fullerton, *J. Phys. D* **35**, 157 (2002).
- [16] R.J. Harrison and A. Putnis, *Phys. Chem. Minerals* **26**, 322 (1999).
- [17] C. B. Azzoni, M. C. Mozzati, L. Malavasi, P. Ghigna and G. Flor, *Solid state communications* **119**, 591 (2001).
- [18] D. Levy, V. Diella , M. Dapiaggi, A. Sani, M. Gemmi and A. Pavese, *Phys Chem Minerals* **31**, 122 (2004).
- [19] S. M. Antao, I. Hassan, and J. B. Parise, *American Mineralogist* **90**, 219 (2005).
- [20] A. J. Millis, *Phys. Rev. B* **53**, 8434 (1996).

- [21] M. W. Lufaso and P. M. Woodward, *Acta Cryst B* **60**, 10 (2004).
- [22] J. Kub, V. Brabers, P. Novák, R. Gemperle and J. Šimšová, *J. Magn. Magn. Mat* **217**, 19 (2000).
- [23] D. Capsoni, M. Bini, G. Chiodelli, V. Massarotti, C. B. Azzoni, M. C. Mozzati and A. Comin, *Phys. Chem. Chem. Phys* **3**, 2162 (2001).
- [24] See, for example, H. Kronmüller and M. Fähnle, *Micromagnetism and the Chap. 6, Microstructure of Ferromagnetic Solids* (Cambridge University Press, Cambridge, 2003), p.90-147.
- [25] J. D. Livingston, *J. Appl. Phys* **52**, 2544 (1981).
- [26] D Sander, *J. Phys.: Condens. Matter* **16**, 603 (2004).
- [27] S. Rusponi, T. Cren, N. Weiss, M. Epple, P. Bulushek, L. Claude, and H. Brune, *Nature Materials* **2**, 546 (2003).
- [28] H. Zeng, J. Li, J. P. Liu, Zhong, L. Wang and S. H. Sun, *Nature* **420**, 395 (2002).
- [29] V. Skumryev, S. Stoyanov, Y. Zhang, G. Hadjipanayis, D. Givord and J. Nogués, *Nature* **423**, 850 (2003).
- [30] See, for example, K. E. Easterling and D. A. Porter, *Phase Transformations in Metals and Alloys* (CRC Press, Florida, 2 edition (1992)), Chap. **1**, p. 33.
- [31] A. G. Khachaturyan, *Theory of Structural transformations in solids* (Wily, New York, 1983), Chap. **10**, p. 315-367.
- [32] Y. Le. Bouar, A. Loiseau, and A. G. Khachaturyan, *Acta Mater* **46**, 2777 (1998).
- [33] A. Suzuki and M. Takeyama, *J. Mater. Res* **21**, 21 (2006).
- [34] D. Weller and A. Moser, *IEEE Tran. Magn* **35**, 4423 (1999).
- [35] S. H. Charap, P. L. Lu and Y. He, *IEEE Tran. Magn* **33**, 978 (1997).

- [36] H. Zheng, J. Wang, S. E. Lofland, Z. Ma, L. Mohaddes-Ardabili, T. Zhao, L. Salamanca-Riba, S. R. Shinde, S. B. Ogale, F. Bai, D. Viehland, Y. Jia, D. G. Schlom, M. Wuttig, A. Roytburd, R. Ramesh, *Science* **303**, 661 (2004).

Chapter III

Nanostructure in the Mn-Doped CoFe_2O_4 Spinel

1. Introduction

Recently, organized nanostructure in the non-magnetic normal spinel system $\text{ZnMn}_x\text{Ga}_{1-x}\text{O}_4$ has been fabricated by a chemical phase separation [1]. This pioneering work first demonstrated that solid state self-assembly mediated by cooperative distortions of Jahn-Teller (JT) ions (Mn^{3+}) could produce an ordered nanostructure through spinodal decomposition in which two distinct types of square rods, with different Mn concentrations but comparable sizes, were interlaced to form a cross-sectional checkerboard pattern. This emergent method provides an alternative route to fabricate ordered nanostructures, which are usually achieved by the conventional bottom-up and top-down techniques [2,3]. However, highly ordered and densely packed magnetic nanocrystals with tunable sizes, which are indispensable for nanotechnology applications, have not yet been demonstrated by using this unique method, despite a similar, but poorly-ordered nanostructure was reported earlier in a magnetic inverse spinel system $\text{Mg}(\text{Mn}_x\text{Fe}_{1-x})\text{O}_4$ [4]. CoFe_2O_4 is an outstanding permanent magnet with high coercivity and moderate magnetization, showing great potential in magnetic recording applications [5]. In the past few years, tremendous work has been devoted to fabricate its nanostructures with diverse geometries [6-9]. Yet, no highly ordered nanostructure has been realized.

2. Experimental Method

Polycrystals $\text{Co}_x\text{Fe}_{1.5-x}\text{Mn}_{1.5}\text{O}_4$ ($x = 0.5, 0.6$) were prepared by the conventional solid state reaction. High purity oxides Co_3O_4 , MnO_2 and Fe_2O_3 were mixed and sintered at 900-1150 °C, followed by quenching into air (or ice water) and isothermally annealing

with different periods of time. Details of the sample characterization were described elsewhere [1.4].

3. Result and Discussion

In this study, we focused on a new magnetic spinel system Mn-doped CoFe_2O_4 (with nominal composition $\text{Co}_{0.6}\text{Fe}_{0.9}\text{Mn}_{1.5}\text{O}_4$), which can be viewed roughly as a proper mixture of CoFe_2O_4 and CoMn_2O_4 compounds classified as inversed and normal spinels, respectively [10]. At room temperature, CoFe_2O_4 adopts a cubic ferromagnetic phase ($a \approx 8.3 \text{ \AA}$, $T_c \sim 800 \text{ K}$) [5,6] and CoMn_2O_4 (with the presence of Mn^{3+} JT ions) adopts a tetragonal paramagnetic phase ($a \approx 8.1 \text{ \AA}$, $c \approx 9.3 \text{ \AA}$, $T_c \sim 100 \text{ K}$) [11,12]. This particular system was chosen based on the consideration that the ionic sizes of the three cations are very close so that the substitutional diffusion can occur easily and naturally. Moreover, due to the high Curie temperature of CoFe_2O_4 , the JT distortion after doping with Mn is expected to occur at high temperatures. Additionally, we performed isothermal annealing instead of slow cooling during the heat treatment to reduce the compositional fluctuation after phase separation. This heat treatment significantly improves the homogeneity of elastic field originating from the lattice mismatch between different chemical compositions.

Unprecedented ordered arrays of rectangular magnetic nanorods with tunable cross sections are achieved in the present study. Evolution of the structure, morphology and the corresponding changes of magnetic properties with isothermal annealing time were studied in details. It was observed that, in the early stage of annealing, $\text{Co}_{0.6}\text{Fe}_{0.9}\text{Mn}_{1.5}\text{O}_4$

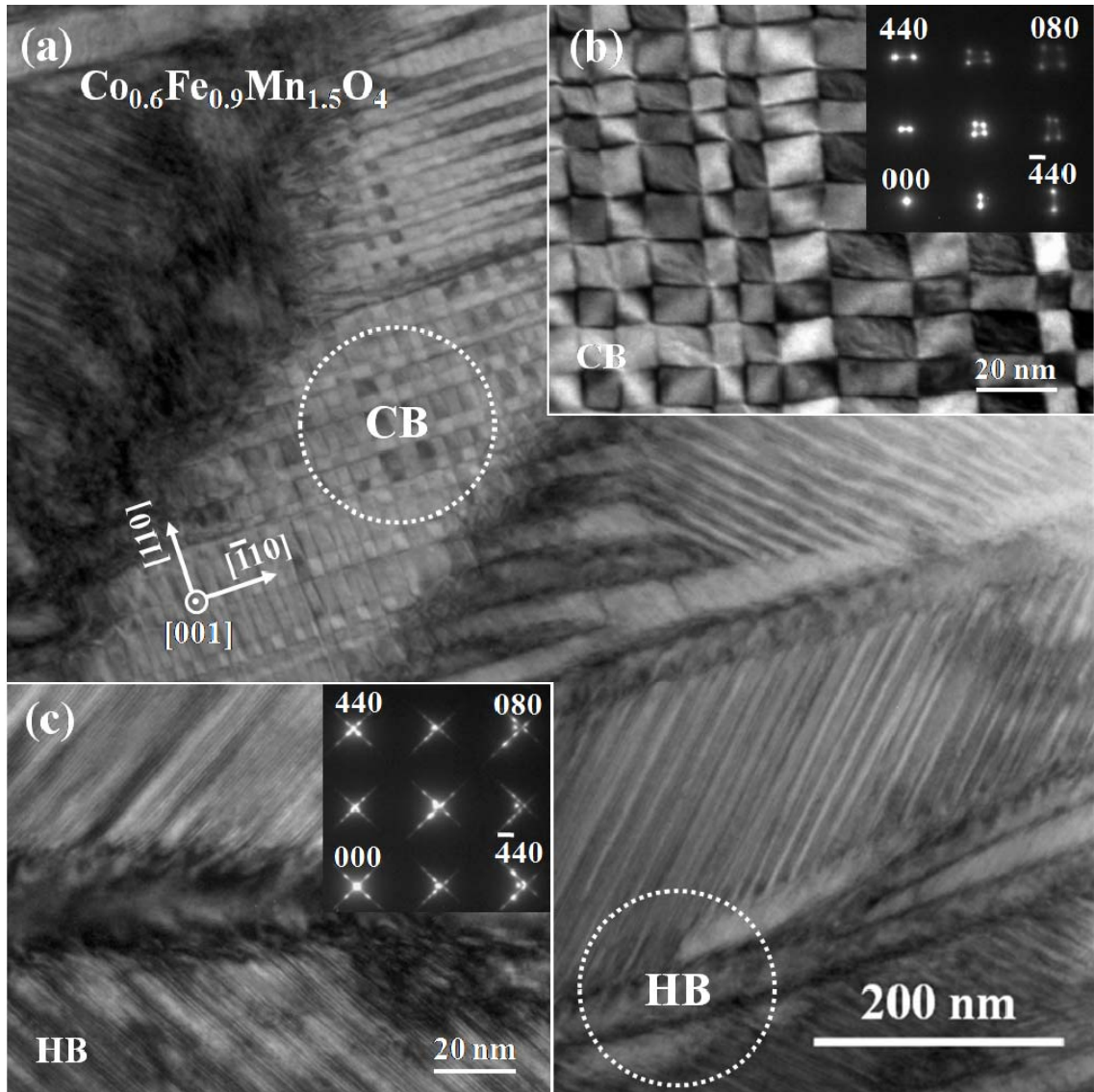


FIG. III.1. Bright field TEM images of $\text{Co}_{0.6}\text{Fe}_{0.9}\text{Mn}_{1.5}\text{O}_4$ annealed at 375 °C for 324 hours. (a) Coexisting nanoscale checkerboard (CB) and herringbone (HB) domains, (b) and (c) Expanded views of checkerboards (the upper circled region) and herringbones (the bottom circled region). The insets are the corresponding diffraction patterns.

undergoes an allotropic transformation from the cubic structure of the quenched specimen to a metastable tetragonal phase driven by the cooperative JT distortions. It is noteworthy that all of the isothermal annealing experiments are performed below the JT transition temperature between the previously mentioned cubic and tetragonal phases. With further annealing, the intermediate tetragonal phase, accompanied by inter diffusion of Fe and Mn ions, spinodally decomposes into a mixture of two equilibrium phases with distinguished crystallographic and magnetic properties: $\text{Co}_{0.6}\text{Fe}_{1.6}\text{Mn}_{0.8}\text{O}_4$ (cubic, $T_c \sim 560$ K) and $\text{Co}_{0.6}\text{Fe}_{0.2}\text{Mn}_{2.2}\text{O}_4$ (tetragonal, $T_c \sim 70$ K) (see below for further discussions on the chemical compositions). These two phases serve as the two types of fundamental building blocks for the checkerboard formation. With the emergence of the nanostructure, the magnetic coercivity is enhanced by a factor of ~ 10 at 5 K. The size of checkerboards is tunable with composition, and particularly with isothermal annealing time in the range of $\sim 13.8 \times 7.9 \text{ nm}^2$ and $\sim 17.3 \times 14.0 \text{ nm}^2$. At room temperature, the alternately stacked ferrimagnetic and paramagnetic domains exhibit a nearly ideal configuration for patterned perpendicular recording medium [13-15]. Engineering of the periodic domain patterns of magnetic nanocrystals with high anisotropy is believed to be one of the promising routes to achieve storage density well beyond the limit of superparamagnetic effect [16,17]. Compared with our previous work on the $\text{Mg}(\text{Mn}_x\text{Fe}_{1-x})\text{O}_4$ system [4], the magnetic nanocheckerboards achieved here are tunable in size, much better organized with a high degree of uniformity throughout the entire grain, and exhibit more than 10 times higher coercivity at room temperature. All of the above advantages are definitely important in order to exploit the nanostructure of checkerboards for device applications. Therefore, these nanocheckerboards offer a superior prototype for the ultra high density

magnetic recording media [18].

Annealing time was found to have the most critical effect on the microstructure of the Mn-doped CoFe_2O_4 . We will first discuss the highly ordered overall nanostructure in the form of long rectangular nanorods observed in the $\text{Co}_{0.6}\text{Fe}_{0.9}\text{Mn}_{1.5}\text{O}_4$ sample annealed at 375 °C for 324 hours (h) as shown in Fig. III. 1(a). Nanorods are periodically stacked in a particular way such that the side view is herringbone (HB)-like with length ~ 300 nm, and the cross-sectional view is checkerboard (CB)-like with the average size $\sim 15 \times 10$ nm². Expanded views of the HB and CB (circled regions) are exhibited in Fig. III. 1(b) and (c), respectively, with their corresponding diffraction patterns. The diffraction pattern of the HB clearly shows densely packed superlattice spots on a streaking diffuse background. The periodicity of the superlattice spots is ~ 18 nm, close to the distance between dark/bright fringes of HBs (Fig. III. 1(b)) and the diagonal length of the CBs (Fig. III. 1(c)). Four types of spots in the diffraction pattern of the CB (the inset of Fig. III. 1(c)) can be identified, revealing that the CB is a patchwork of four different types of domains.

Detailed microstructural information of the CB is nicely revealed through the analyses of high resolution TEM image (Fig. III. 2(a)) and the corresponding electron diffraction, Fig. III. 2(c). The CB pattern is found to be an intricate patchwork of four different types of domains denoted as α , β , γ , and δ . It is noted that α and γ domains are tetragonal (more accurately, orthorhombic) whereas β and δ are cubic. The horizontal and vertical domain boundaries in Fig. III. 2(a) adopt a slightly zigzag variation with a rotation angle $\sim 7^\circ$, consistent with the observation in Fig. II.1(b). The zigzag arrangement of CB is a way to accommodate large shears with minimal macroscopic shear strain by lattice invariant deformation, similar with the observation in Ti-48.2Ni-1.5Fe alloy [19].

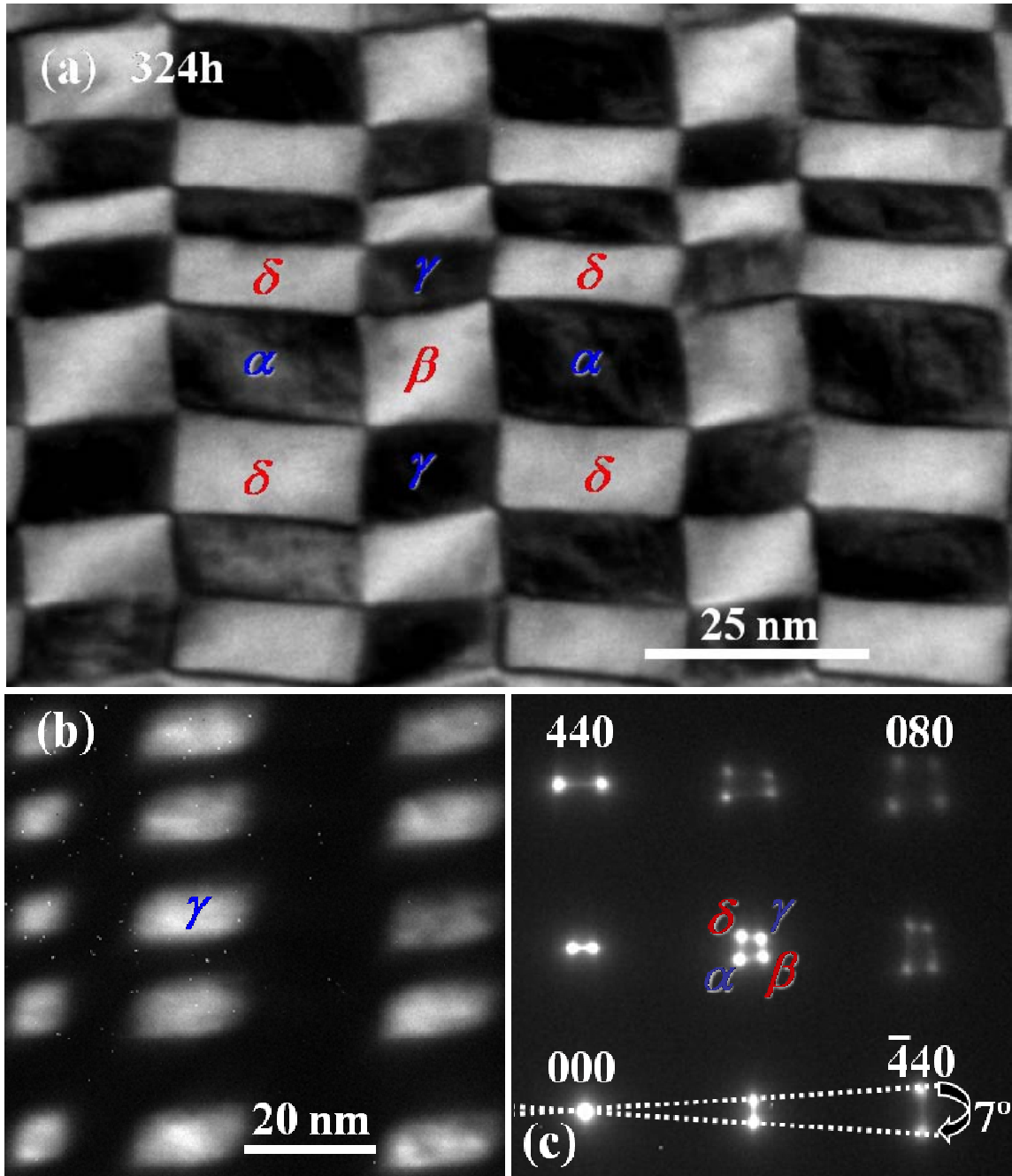


FIG. III.2. (a) High-resolution TEM image of the checkerboard in the 324 h-annealed specimen at 375 °C, which consists of two cubic domains α and γ with different rotations and two tetragonal domains β and δ with different orientations. (b) Dark field image taken by using γ spot around (008) position; (c) The diffraction pattern of checkerboard domains, the dashed lines with arrows indicate the rotations of the two cubic domains.

Lattice constants are estimated from the positions of the diffraction peaks. The dark field image, (Fig. III. 2(b)) using γ peak around (080) position, distinctly shows the highly ordered and alternating CBs of the tetragonal phase. The formation of complex microstructure is often concomitant with a chemical phase separation of the system during growth. Indeed, using energy dispersive X-ray spectrometry (EDS) with a fine electron probe ~ 0.2 nm, we have determined the chemical compositions to be approximately $\text{Co}_{0.6}\text{Fe}_{1.6}\text{Mn}_{0.8}\text{O}_4$ (Fe-rich) and $\text{Co}_{0.6}\text{Fe}_{0.2}\text{Mn}_{2.2}\text{O}_4$ (Mn-rich) for the cubic and tetragonal domains, respectively. The cobalt concentration is unchanged and uniform throughout the sample.

Having established the ordered CB structure of the nanorods, we now turn to the evolution of the microstructure with varying annealing time. Fig. III. 3(a) shows the X-ray diffraction (XRD) patterns of $\text{Co}_{0.6}\text{Fe}_{0.9}\text{Mn}_{1.5}\text{O}_4$ annealed at 375 °C. The crystal structure evolved remarkably with prolonged annealing time. Here, we introduce four notations C' , T' , C and T to facilitate the description of the structural change with annealing time. C' is a metastable cubic phase of the quenched sample, which is a high temperature phase with random distribution of the three cations on tetrahedral (A) and octahedral (B) sites in the crystal structure. T' is an intermediate metastable tetragonal phase for the 3.6 h-annealed sample, presumably with the same composition as C' but more Mn^{3+} ions now occupying the B sites randomly. It should be noted that Mn^{3+} ions become JT active once situated in B sites. C denotes the Fe-rich cubic phase and T the Mn-rich tetragonal phase after the phase separation under thermal equilibrium condition. The quenched sample undergoes a displacive, martensitic transformation during the first 10 minutes of annealing. We note from XRD patterns that the (311) peak has

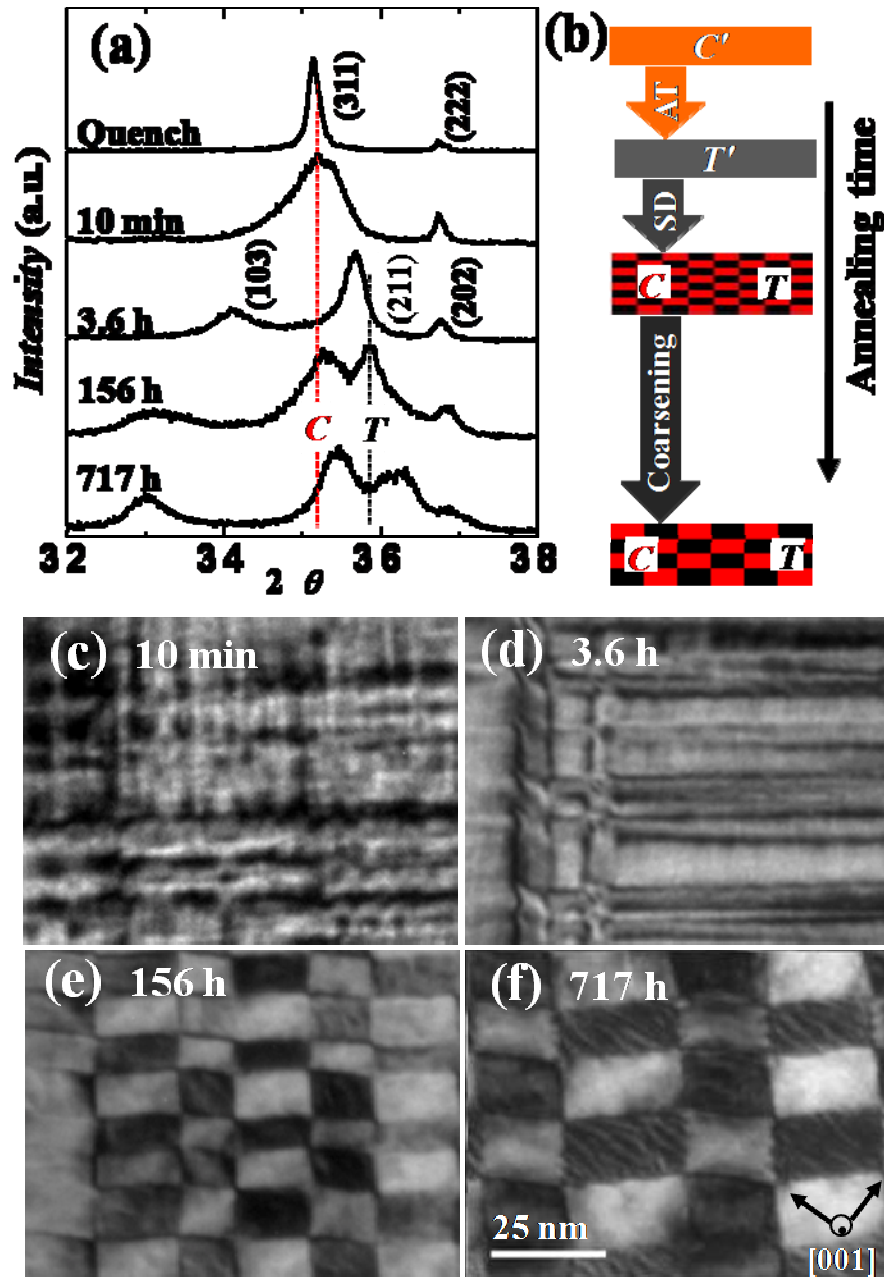
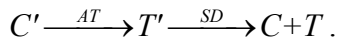


FIG. III.3. (a) XRD patterns of $\text{Co}_{0.6}\text{Fe}_{0.9}\text{Mn}_{1.5}\text{O}_4$ annealed at 375 °C with selected annealing time, *C'* is the cubic phase of the quenched specimen, *T'* is the tetragonal phase of the 3.6 h-annealed specimen, and the cubic and tetragonal peaks are denoted. *C* and *T* are the final equilibrium cubic and tetragonal phases after phase separation. The dashed lines indicate the positions of (311) and (211) peaks; (b) Schematic process of crystal structure evolution with prolonging annealing time; (c)-(f) The corresponding microstructure development with annealing time. All images have the same scale.

significantly broaden whereas the (222) peak still remains sharp. This suggests that the displacive distortions are confined in the (111) planes during the martensitic transformation. With further annealing, an allotropic transformation (AT) takes place which involves Mn^{3+} ions diffusing from A sites to B sites and then becoming JT active. Therefore, the quenched C' phase is completely converted to the T' phase due to the cooperative JT distortion. The T' phase is highly unstable and immediately subjects to spinodal decomposition (SD) into a new Fe-rich cubic phase C and a new Mn-rich tetragonal phase T , demonstrated by the two sets of peaks in the 156 h-annealed specimen. The broadening of cubic (311) and tetragonal (211) peaks is consistent with the appearance of nanostructure. Due to the spinodal instability, extending the annealing time up to 717 h causes small further splitting of the above two peaks, indicating coarsening of the nanostructure associated with larger scale phase separation. No significant changes were observed beyond 156 h, suggesting that stable equilibrium has been largely reached. Thus, the whole structural evolution process starts from a supersaturated cubic phase C' , then allotropically transforms to a metastable tetragonal state T' , and eventually precipitated into two equilibrium phases through spinodal decomposition: C and T . Fig. III. 3(b) is a schematic structural transformation pathway with annealing time:



It might be worthy to address T' phase a little bit. In the point view from diffusion, the metastable T' phase could play an important role in the formation of CB pattern in the subsequent of spinodal decomposition. The diffusion coefficient D is a scalar for a cubic structure, in which ion diffusion responds to chemical gradient identically in all

directions: $[D_{ij}] = \begin{bmatrix} D & & \\ & D & \\ & & D \end{bmatrix} = D$. Whereas in the lower symmetry system such as a

tetragonal structure, the ion diffusion anisotropically respond the chemical gradient with

exhibiting two independent diffusivity elements: $[D_{ij}] = \begin{bmatrix} D_{11} & & \\ & D_{11} & \\ & & D_{33} \end{bmatrix}$. The highly

anisotropy of diffusion should contribute to the formation of the heterogeneous microstructure [20,21]. So, the preferential diffusion occurs along the elastically soft directions, which coincides with the boundaries of CBs.

Fig. III. 3(c-f) show bright-field TEM images indicating the corresponding pronounced changes of microstructure with annealing time: from the initial tweed structure to the intermediate twin followed by nanoscale checkerboards. This is in good agreement with the structural evolution discussed above. The most impressive feature of the morphology evolution is that the size of CBs is tunable with annealing time. For the 10 min-annealed sample, the tweed microstructure (Fig. III. 3(c)) along the elastically soft direction $[110]$ or $[\bar{1}10]$ occurs immediately as a result of the diffusionless martensitic transformation due to the rapid small cooperative displacements. Following the disappearance of the tweed structure, the presence of twinned domains (T' phase) was observed in the 3.6 h-annealed specimen (Fig. III. 3(d)). Prolonged annealing over 90 h led to the formation of highly ordered CB domains from the twinned structure of the T' phase. Subsequently, the CBs undergo continuous adjustment with annealing time: the average size of CBs varies from $\sim 13.8 \times 7.9 \text{ nm}^2$ in the 90 h-specimen up to $\sim 17.3 \times 14.0 \text{ nm}^2$ in the 717 h-specimen (Fig. III.3(f)). Generally speaking, the wavelength of spinodal

decomposition is strongly temperature and annealing time dependent. Here we only observed a small fluctuation of compositions in the C and T phases in various samples under longer annealing. The compositions of the checkerboard domains are approximately $\text{Co}_{0.6}\text{Fe}_{1.6}\text{Mn}_{0.8}\text{O}_4$ and $\text{Co}_{0.6}\text{Fe}_{0.2}\text{Mn}_{2.2}\text{O}_4$ for C and T , respectively. This unambiguously indicates that the coarsening occurs without long range diffusion of ions, consistent with the subtle shift of (311) and (211) peaks (in Fig. III. 3(a)) and the invariant Curie temperature (T_c) of T phase (in Fig. III. 4a) with annealing time.

The slow coarsening of CBs is a capillarity-driven process, usually originating from the excess free energy of surfaces or interfaces [22]. The phase boundaries between C and T build up high energy barriers preventing the Mn ions in the T phase from diffusing back to the C phase, and the Fe ions in the C phase back to the T phase. We proposed that the only possible channel for coarsening is through the contacted corners of the CBs having the same phase such as C - C or T - T . The diffusion channel is so narrow that the coarsening rapidly slows down with decreasing the number of edges. As shown in Fig. III.1(b) and Fig. III.3(f), the average size of CBs in 324 h-annealed specimen does not look much different from that of the 717 h-annealed specimen, although the annealing time is more than twice longer. The final adopted size of CBs is assumed to be mainly determined from the balance between the elastic strain energy from the lattice mismatch and interfacial free energy of C and T [22-25].

Meanwhile, we notice that the rotation of β and δ increases from $\sim 6^\circ$ in the 90 h-annealed specimen to $\sim 8^\circ$ in the 717 h-annealed specimen so as to minimize macroscopic shear strains in a local region. Moreover, as shown in the 717 h-annealed specimen (Fig. III. 3f), fine striations on the T phase of CBs appear and align along the diagonal

direction of CBs, signifying further relief of lattice or shear strains. Since longer annealing always gives rise to larger concentration difference in the final phases before reaching a thermodynamic equilibrium, the lattice mismatch between different phases will lead phase boundaries evolving from coherent to semi-coherent and eventually to incoherent. Coherent boundaries are characterized with contiguous lattice planes associated with strongly localized strains, semi-coherent boundaries have periodic dislocations to reduce strains, and incoherent boundaries have neither contiguous planes nor boundary dislocations but possible long-range strain fields. The microstructures of precipitates take diverse morphologies with the variation of elastic strain. Thus, the increased rotation and appearance of fine striations are the natural consequences to reduce the strongly localized static strains both at the phase boundaries and within the CB domains [22].

The normalized M/H vs temperature curves (Fig. III. 4(a)) show that T_c of the quenched specimen (C' phase) and the 3.6 h-annealed one (T' phase) are above room temperature. A transition at ~ 70 K signifying T_c of the T phase, $T_c(T)$, is observed for specimens with the formation of CB ($C+T$ phases). We note that T_c of the C phase, $T_c(C)$, as determined by high temperature M/H measurement, is located at a much higher temperature ~ 560 K. $T_c(T)$ remains nearly unchanged for all of the specimens with $C+T$ phases. This further confirms that the compositional fluctuation is small, as suggested by XRD (Fig. III. 3(a)) and EDS measurements.

Fig. III. 4(b) shows the coercivity H_c and remanent magnetization M_r vs. annealing time in logarithmic scale at 5 K. H_c increases steadily from ~ 710 Oe for the quenched

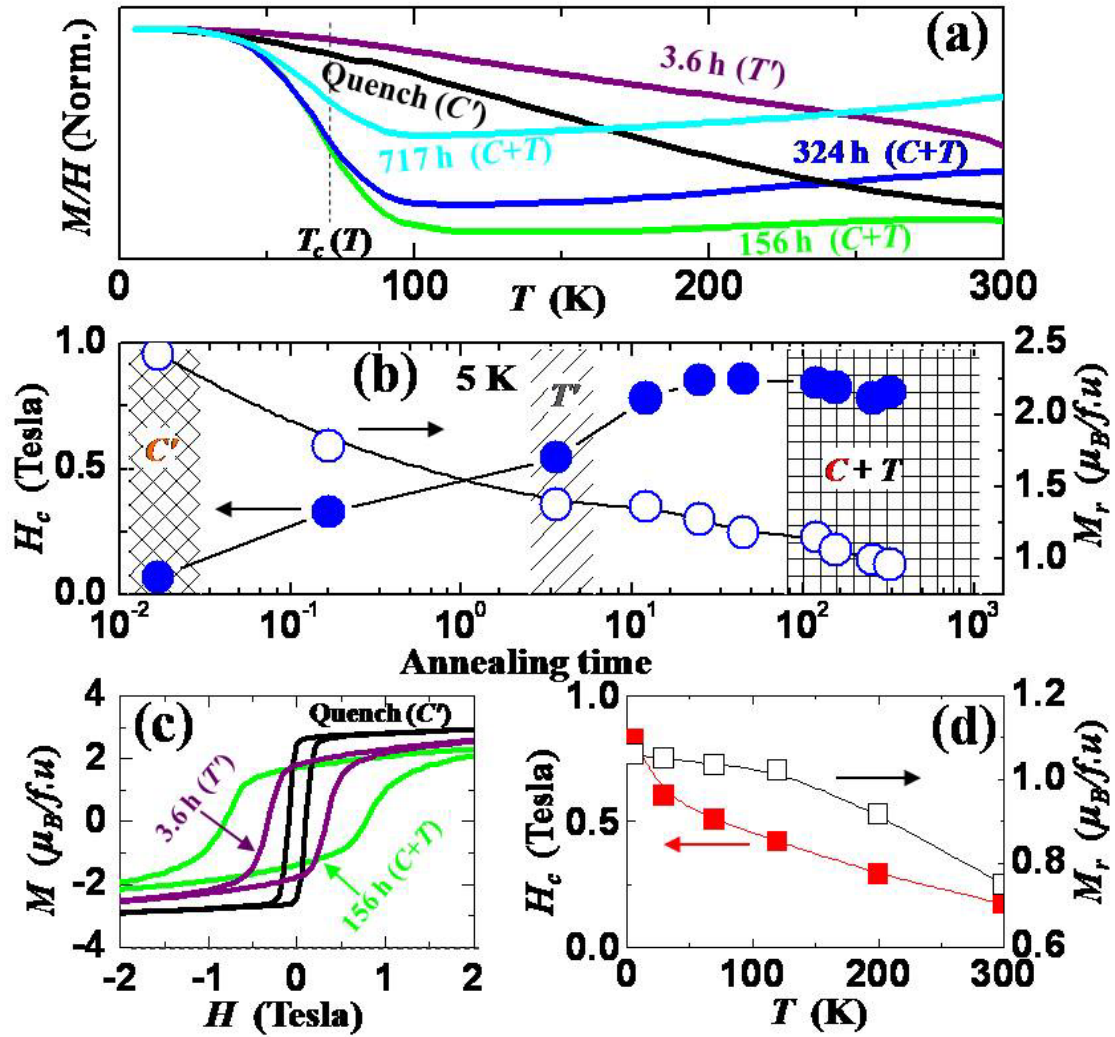


FIG. III.4. Magnetic properties of $\text{Co}_{0.6}\text{Fe}_{0.9}\text{Mn}_{1.5}\text{O}_4$ annealed at 375°C with selected annealing time. (a) Normalized M/H vs temperature with 200 Oe field cooling; (b) H_c (●) and M_r (○) vs annealing time in the logarithmic scale at 5 K, the shadow and patterned regions indicate the structure evolution with annealing time; (c) $M(H)$ at 5 K; (d) H_c (■) and M_r (□) vs temperature for the 156 h-annealed specimen.

sample to ~ 8400 Oe for the 156 h-annealed specimen, and remains largely unchanged ~ 8000 Oe with even longer annealing. Correspondingly, M_r decreases from $\sim 2.4 \mu_B / f.u$ to $\sim 1.1 \mu_B / f.u$ then to $\sim 0.96 \mu_B / f.u$ (Note: we took account of the magnetic contribution from the entire sample). Fig. III. 4(c) displays $M(H)$ curves of specimens with C' , T' and $C+T$ phases, which clearly shows that the strong enhancement of coercivity due to the formation of nanorods. Once the nanorods are formed, their magnetic properties are quite stable with annealing time as evidenced by small variations of H_c and M_r . Fig. III. 4(d) is H_c and M_r vs. temperature for the 156 h-annealed sample with the average size of the CB $\sim 14 \times 9$ nm². Since $T_c(T)$ is ~ 70 K, the contribution of the measured magnetic properties above 70 K are mainly from the C phase. We did not see any abrupt changes of H_c and M_r around 70 K, indicating the very weak magnetic properties of the T phase even at the low temperatures. If we only consider the contribution from the C phase, H_c and M_r at 300 K could be ~ 2100 Oe and $\sim 1.5 \mu_B / f.u$, respectively. Compared with that of 10°C/h-cooled $\text{MgMn}_{1.5}\text{Fe}_{0.5}\text{O}_4$ ($M_r \sim 0.27 \mu_B / f.u$, $H_c \sim 150$ Oe, at 300 K) [4], the 156 h-annealed $\text{Co}_{0.6}\text{Fe}_{0.9}\text{Mn}_{1.5}\text{O}_4$ shows a much larger coercivity and magnetization in the whole temperature range (we assumed that the amount of C phase is approximately half in both samples).

Practical applications of the magnetic nanostructure require the nanorods to be magnetically isolated without significant couplings among them [8,28]. With the lack of magnetic imaging techniques capable of resolving each individual magnetic nanorod, we can only speculate the extent of their magnetic coupling. We note that both C and T nanorods are insulators and the magnetic nanorods (C) are surrounded by nonmagnetic counterparts (T) at room temperature, therefore the dominant magnetic interaction is

probably dipole-type. Thus, the magnetic coupling among the magnetic nanorods ought to be weak and these nanorods may be readily controlled at room temperature.

4. The Mechanism in the Formation of Nanocheckerboards

The CB microstructure has been observed in several metallic systems such as Co-Pt. A 2D phase field microelasticity (PFM) was employed to explain the mechanism of the CB formation. But, the reduction from 3D to 2D leaves an open question: how the microstructure evolves with the isothermal annealing time [25]. Recently, the 3D PFM model gives quite clear time-dependent pictures and reasonably describes the natural underlying mechanism [26].

According to the free energy diagram of the cubic and tetragonal phases at a fixed temperature (Fig. III.5), the composition $\text{Co}_{0.6}\text{Fe}_{0.9}\text{Mn}_{1.5}\text{O}_4$ we study above is located in the region B, more precisely, close to the critical decomposition $c_o(T)$. $c_o(T)$ is on the thermodynamic boundary where cubic and tetragonal phase have equal free energies at the same composition. In the region B, the free energy of tetragonal phase is lower than that of the parent cubic phase. The free energy can be reduced by the quick diffusionless transformation without changing composition. Therefore, the cubic-tetragonal ($C' \rightarrow T'$) first order transformation happens prior to the spinodal decomposition.

In the 3D stochastic PFM model, the contribution from the chemical, elastic and interfacial energies to the transformation driving force has been automatically included. The 3D stochastic PFM equations are given by the time-dependent density functions $c(\mathbf{r}, t)$ and $\eta_p(\mathbf{r}, t)$:

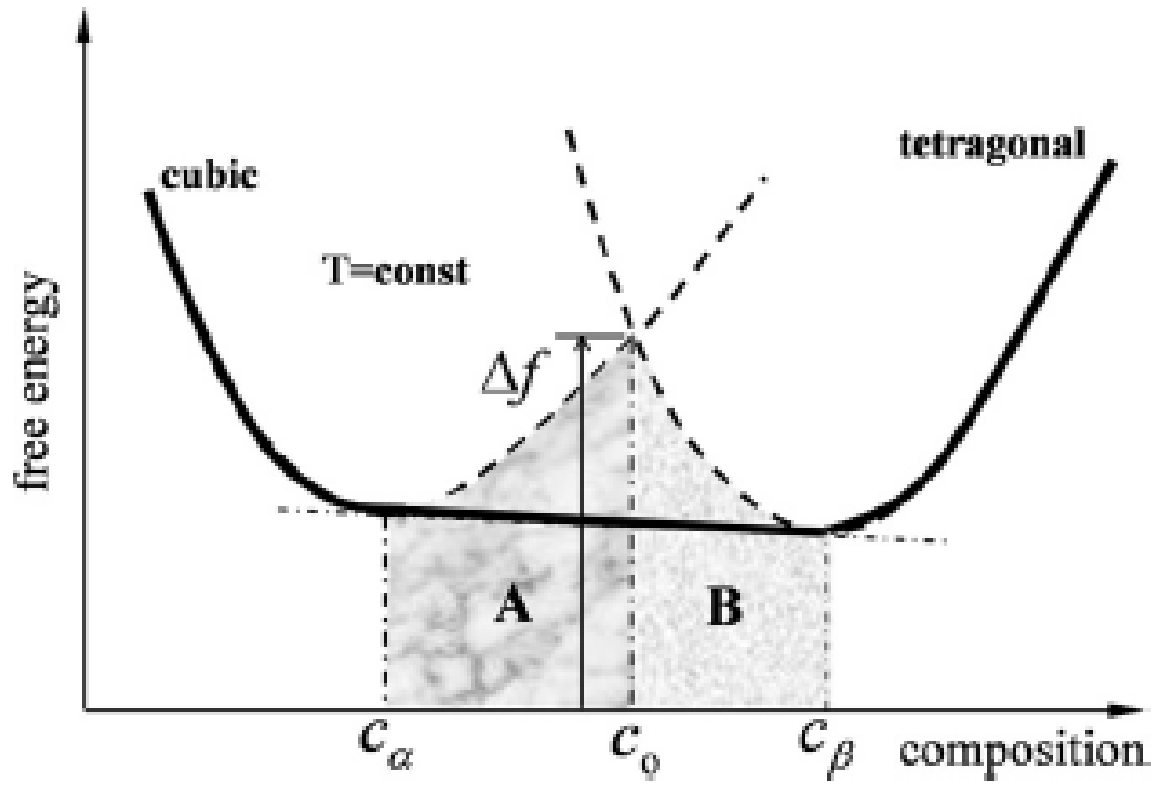


FIG. III.5. A schematic free energy vs. composition diagram for the spinodal decomposition with coherent cubic and tetragonal phases [26].

$$\frac{\partial c(\mathbf{r}, t)}{\partial t} = \nabla(M \nabla \frac{\delta F}{\delta c(\mathbf{r}, t)}) + \zeta^c(\mathbf{r}, t), \quad (1)$$

$$\frac{\partial \eta_p(\mathbf{r}, t)}{\partial t} = -L \frac{\delta F}{\delta \eta_p(\mathbf{r}, t)} + \zeta_p^\eta(\mathbf{r}, t), \quad (2)$$

where $c(\mathbf{r}, t)$ is the function of composition at the point \mathbf{r} and time t , $\eta_p(\mathbf{r}, t)$ is the long-range order parameters characterizing a density of structural domains of the p -th type (p represents the three different orientations of the tetragonal domains), F is the free energy, $\delta F/\delta c(\mathbf{r}, t)$ and $\delta F/\delta \eta_p(\mathbf{r}, t)$ are the transformation driving forces, M and L are the kinetic coefficients characterizing the diffusional mobility, $\zeta^c(\mathbf{r}, t)$ and $\zeta_p^\eta(\mathbf{r}, t)$ are the Gaussian-distributed Langevin noise terms describing the thermal fluctuations which induce the nucleation of tetragonal phases from the parent cubic compound.

The non-equilibrium free energy F is composed by Landau “chemical” energy and the elastic strain energy:

$$F = \int_V \left[f_L(c, \{\eta_p\}) + \beta_c (\nabla c)^2 + \sum_{p=1}^3 \beta_p (\nabla \eta_p)^2 \right] d^3r + \frac{1}{2} \int_{|\mathbf{k}| \neq 0} B(\mathbf{e})_{ijkl} \tilde{\varepsilon}_{ij}^0(\mathbf{k}) \tilde{\varepsilon}_{kl}^{0*}(\mathbf{k}) \frac{d^3k}{(2\pi)^3}, \quad (3)$$

where $f_L(c, \{\eta_p\})$ is the chemical free energy density, β_c and β_η are the constants determining the equilibrium properties of the system, $\tilde{\varepsilon}_{ij}^0(\mathbf{k})$ is the Fourier transform of Bain strain $\varepsilon_{ij}^0(\mathbf{r})$, \mathbf{k} is the wave vector, the symbol $*$ denotes the complex conjugate. $B(\mathbf{e})_{ijkl}$ is an algebraic function depending on the materials properties and related to the Green function of the elasticity problem, $\mathbf{e} = \mathbf{k}/k$.

The evolution of microstructure at B region $c > c_o(T)$ with different time scale is simulated as shown in Fig. III.6. The simulation patterns are quite reasonable consistent with the TEM observations. Presumably, decomposition in this case is actually a pseudo-spinodal decomposition which takes place among phases with different symmetries and is accompanied with nucleation. In sharp contrast, homogenous parent compound during a standard decomposition directly separates into phase mixture. The compositions of nucleated phases are close to that of parent compounds. The difference is asymptotically vanish when the compositions of parent compounds shift to the critical point $c_o(T)$. Hence, nucleation possibly occurs without large compositional fluctuation. The nucleation rate is comparable with the cubic-tetragonal displacive transformation. This particular nucleation causes both structural and compositional heterogeneous. The nucleation is of important to induce a tweed structure, formed by tetragonal nano domains embedded in the parent cubic matrix. The tetragonal nano domains with different orientations are spatially coherent so that the tweed structure serves as a template for developing nano CBs in the later stage. The prerequisite condition of nucleation is that the initial composition of parent compound is contiguous to the boundary $c_o(T)$. Ideally, a composition close to $c_o(T)$, but located in the region A, gives much more organized checkerboard pattern according to the 3D computation, because tetragonal phase already exists there. Due to the competition of the diffusionless cubic-tetragonal transformation and the nucleation of the tetragonal phase involving a short-range diffusion, the frustrated tweed structure is not perfect to form a highly ordered pattern. With the isothermal annealing time, the opposite rotation of rods becomes more obvious. The angle ϕ is proportional to the lattice mismatch between the two phases:

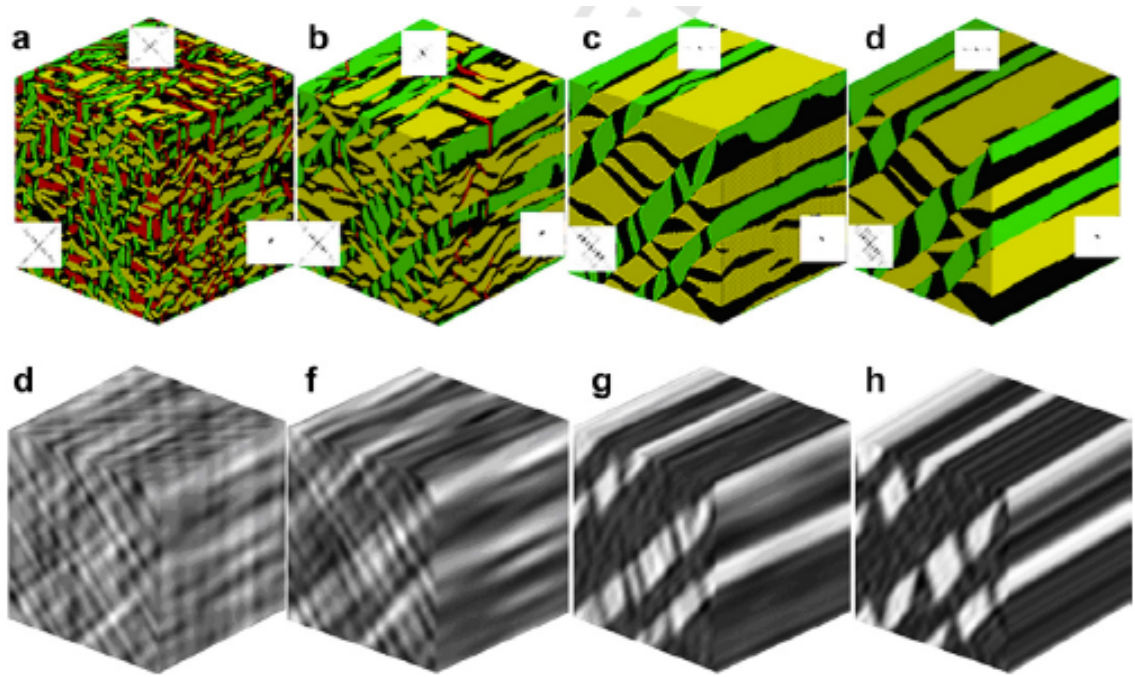


FIG. III.6. The 3D modeling of the microstructure evolution at $c > c_o(T)$ with different time scale. The black color is the cubic phases. Other colors are the tetragonal domains with three different orientations. The diffraction patterns in the insets are generated along $[010]$ axis of the tetragonal phases. (d)-(h) only show the green tetragonal domains by the Fourier filtering to remove small perturbations from the back Fourier transformation describing the image contrast [26].

$\phi \propto \frac{c_T - a_T}{a_C}$, where c_T and a_T are the lattice parameters of the tetragonal phase, a_C is that of the cubic phase. This is a good agreement with the observation in Fig. III.5(e) and (f). The coherent strain might deform the cubic phase to tetragonal phase while the tetragonal phase to orthorhombic phase. This prediction is quite consistent with the observation in the ZGMO thin film [27].

The essential of the model is that the formation of tweed structure is the precondition of the formation of CBs, which serves as a template. It also predicts the evolution of the microstructure with time. Furthermore, it concludes that the lattice parameters along [100] and [010] of tetragonal phase have to be identical to that of cubic phase. Or else, dislocation is going to be generated among the phase boundaries, which will affect the ordering of checkerboards. In some sense, the above simulation based on the 3D model is roughly agreement with our TEM observations.

We notice that the formation of T' phase is totally ignored in the above 3D simulation, which is found critical in the formation of CBs in the ZMGO thin film. Fig. III.7(a) is the dark field image of the as-grown ZMGO thin film. It presents as the tetragonal T' phase since the growth temperature is below the JT transition ($C' \rightarrow T'$) temperature. 90° domains appear. The twins lie vertically in the white regions while horizontally in the dark regions. Fig. III.7(b) is the schematic diffraction pattern of CBs. A and C peaks could be used to present the δ and β phases in Fig. III.2(c). Both are tetragonal phases but with different orientations. By using the “A” peak around (080) position, we see the β phases are actually not continuous stripes but show a tendency of phase separation (Fig. III.7(c)). By using the “C” peak, an image with an inverted contrast appears (Fig. III.7(d)).

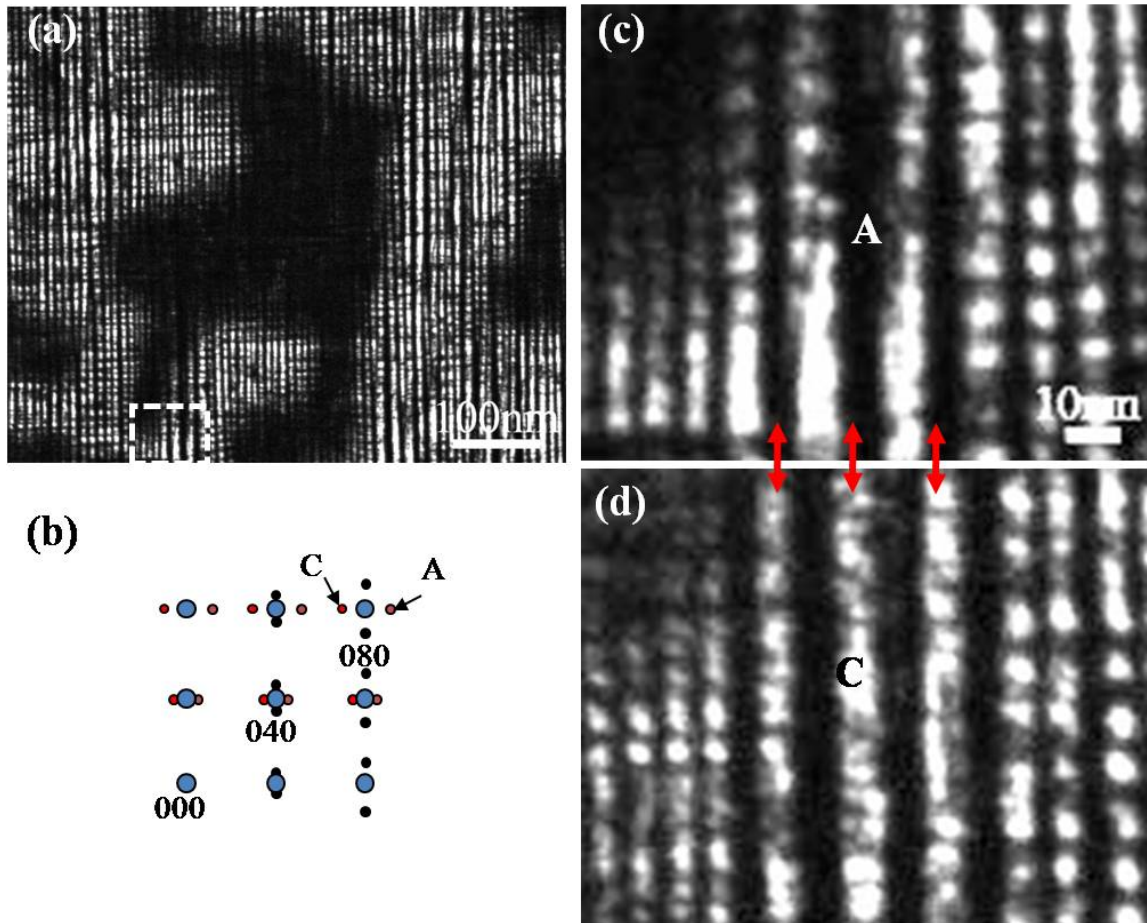


FIG. III.7. (a) The dark field images of the as-grown ZMGO thin film. (b) The schematic view of the diffraction pattern of CBs. The A and C peaks come from the tetragonal T' phase with different orientations. (c) and (d) are the magnified dark field images of the region marked with dashed line in (a) by using A and C peaks, respectively [from Y. Horibe].

The δ domains are also discontinuous. If we overlap their corresponding high magnified TEM images of the β (Fig. III.8(a)) and δ (Fig. III.8(b)) phases, we see that the white regions (the tetragonal phases) are surrounded by dark regions (supposed to be the cubic phases) in Fig. III.8(c). By post annealing on the as-grown film, the blur phase boundaries become sharp and eventually shape into nice CBs as shown in Fig. I.8(c) [28].

The TEM images of the as-grown ZGMO film with T' phase give a quite clear scenario how the twins in the T' phase evolve into CBs through spinodal decomposition. It is the twins in the T' phase, not tweed, serving as a template for the CBs in the subsequent progress of spinodal decomposition. The mechanism of forming CBs in Mn-based spinels is obviously different from the so-called CB patterns observed so far in alloys such as Co-Pt [25]. Undergoing a cubic to tetragonal transformation triggered by JT distortion is crucial in the formation of CBs. The phase field microelasticity (PFM) model which has successfully explained the phase separation in the alloys might have to be further modified in order to clarify our CBs. Some factors such as the external strain effect from the grain boundaries (which we will see in the following chapter) and JT distortion should be seriously counted.

5. Conclusion

In summary, unprecedented ordered arrays of 3D magnetic nanoscale checkerboards, with composition close to CoFe_2O_4 , were achieved in $\text{Co}_{0.6}\text{Fe}_{0.9}\text{Mn}_{1.5}\text{O}_4$ after phase separation, and the size can be readily tuned with the isothermal annealing time. Patterned media is known as the most promising approach to push the magnetic storage density far beyond the superparamagnetic limit. E-beam lithography usually is one of the ways to scale

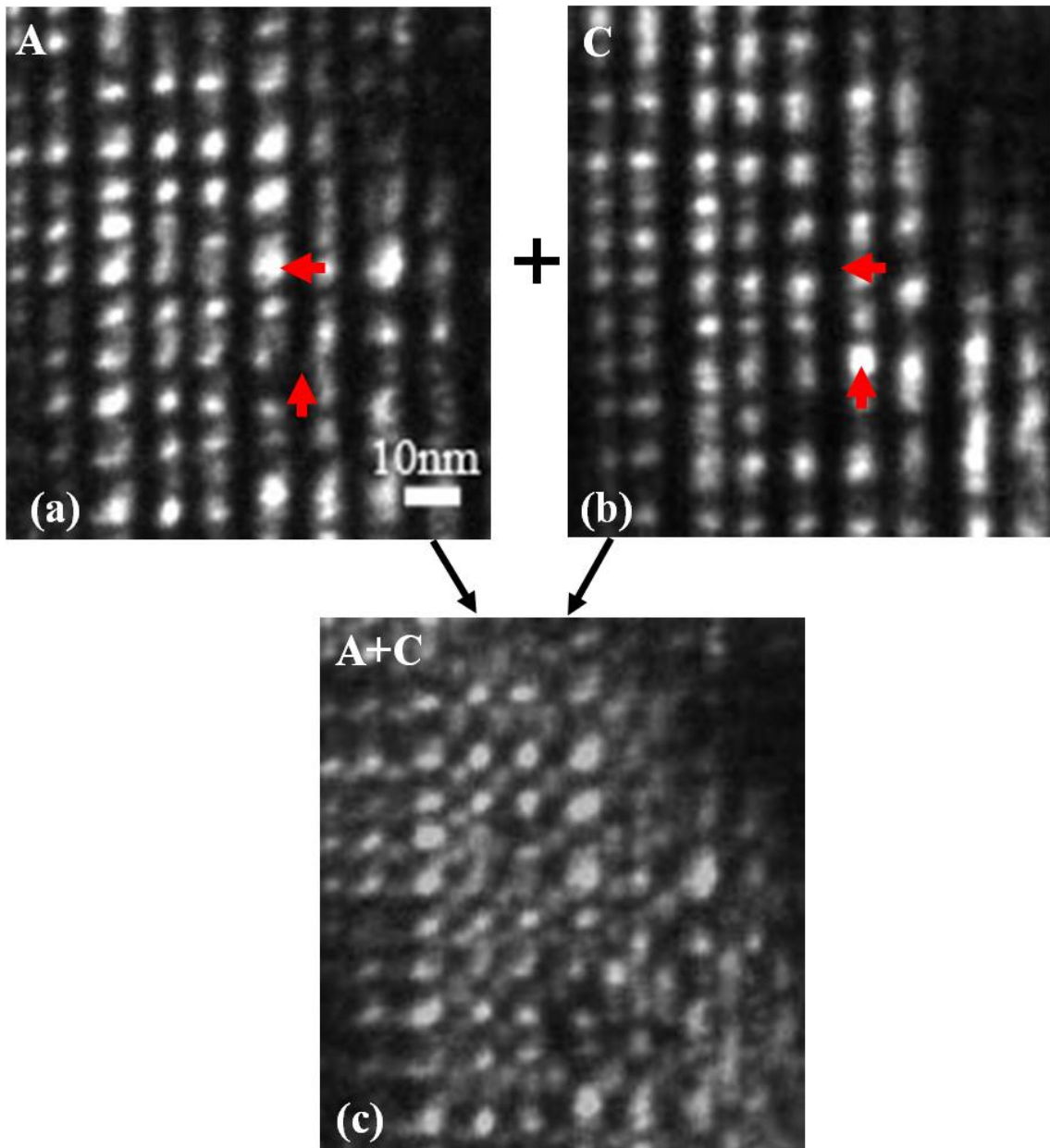


FIG. III.8 (a) and (b) are the high magnified TEM images of Fig. III.7(c) and Fig. III.7(d), respectively. The red arrows indicate that the contrast of the white region in (a) is inverted to the dark region in (b). (c) is the overlap of (a) and (b), showing a tendency of forming CBs [from Y. Horibe].

nanostructured magnetic patterns down to ~ 100 nm. However, it is not economically feasible and difficult to achieve high uniformity by direct deposition method [3]. Here we convincingly demonstrate a spinodal decomposition mediated by the cooperative J-T distortion as an alternative route to fabricate highly self-assembled and uniform nanostructures, with distinguished magnetic properties, down to a few nanometers in the Mn-doped CoFe_2O_4 spinel.

Since CB in ZMGO has been successfully fabricated on film [27], with properly selecting substrates and growth conditions, we believe that our remarkable pattern with well-aligned crystallographic orientation and quasi-long-range order can, in principle, be realized on films. The tunable size of the checkerboards with annealing time, and adjustable length of herringbones with the thickness of films, provide additional degrees of freedom to design the properties and functions of the magnetic nanostructures for ultrahigh magnetic storage density up to $1\sim 10$ Tb/in².

We also briefly discuss the mechanism of the formation of CBs. As we clearly see from the TEM image of the as-grown ZGMO thin film that the CBs form during the spinodal decomposition of the twins in the T' phase, not through the coarsening of tweed. Thus, we propose that the twins instead of tweed in the metastable T' phase serve as a template for the CBs.

6. References

- [1] S. Yeo, Y. Horibe, S. Mori, C. M. Tseng, C. H. Chen, A. G. Khachaturyan, C. L. Zhang, S. -W. Cheong, *Appl. Phys. Lett.* **89**, 233120(2006).
- [2] J. I. Martín, J. Nogués, K. Liu, J. L. Vicent, I. K. Schuller, *JMMM*, **256**, 449(2003).
- [3] J. V. Barth, G. Costantini, K. Kern, *Nature*, **437**, 671(2005).

- [4] C. L. Zhang, S. Yeo, Y. Horibe, Y. J. Choi, S. Guha, M. Croft, S. -W. Cheong, S. Mori, *Appl. Phys. Lett.* **90**, 133123(2007).
- [5] S. Y. Chou, *Proceedings of the IEEE*, **85**, 4(1977).
- [6] D. A. Thompson and J. S. Best, *IBM J. Res. Dev*, **44**, 311(2000).
- [7] D. Weller, A. Moser, *IEEE Trans. Magn.*, **35**, 4423(1999).
- [8] H. Zeng, J. Li, J. P. Liu, Zhong, L. Wang, S. H. Sun, *Nature*, **420**, 395(2002).
- [9] R. Plass, J. A. Last, N. C. Bartelt, G. L. Kellogg, *Nature*, **412**, 875(2001).
- [10] F. S. Galasso, *Structure and properties of inorganic solids*, Oxford, New York, Pergamon Press, Chap. 8(1970).
- [11] K. Maaza, A. Mumtaza, S. K. Hasanaina, A. Ceylan, *JMMM*, **308**, 289(2007).
- [12] M.C. Terzzoli, S. Duhalde, S. Jacobo, L. Steren, C.A. Moina, *J. Alloys Compd.*, **369**, 209(2004).
- [13] Z. Zhang, A. J. Rondinone, J. -X. Ma, J. Shen, S. Dai, *Adv. Mater.*, **17**, 1415(2005).
- [14] A. Hutlova, D. Niznansky, J. L. Rehspringer, C. Estournes, M. Kurmoo, *Adv. Mater.*, **15**, 1622(2003).
- [15] S. T. Kshirsagar, A. B. Biswas, *J. Chem. Phys. Solids*, **28**, 1493(1967).
- [16] S. Tamura, *Physica B*, **190**, 150(1993).
- [17] T. W. McDaniel, *J. Phys.: Condens. Matter*, **17**, 315(2005).
- [18] S. Kartha, *Phys. Rev. B*, **52**, 803(1995).
- [19] T. Fukuda, T. Saburi, K. Doi and S. Nenno, *Mater. Trans. JIM*, **33**, 271(1992).
- [20] D. A. Porter and K. E. Easterling, *Phase Transformations in Metals and Alloys* (CRC Press, Florida, 2 edition (1992)).

- [21] J. W. Martin, R. D. Doherty and B. Cantor, *Stability of Microstructure in Metallic Systems* (Cambridge University Press; 2 edition (1997)).
- [22] R. W. Balluffi, S. M. Allen, W. C. Carter, *Kinetics of Materials*, New York, John Wiley & Sons, 2005.
- [23] A. Suzuki, M. Takeyama, *J. Mater. Res*, **21**, 21(2006).
- [24] Y. Ni, Y. M. Jin, A. G. Khachaturyan, *Acta Mater.*, **55**, 4903(2007).
- [25] Y. Le. Bouar, A. Loiseau, A. G. Khachaturyan, *Acta Mater*, **46**, 2777(1998).
- [26] Y. Ni, and A. G. Khachaturyan, *Acta Mater* (2008), doi:10.1016/j.actamat.
- [27] S. Park, Y. Horibe, T. Asada, L. S. Wielunski, N. Lee, P. L. Bonanno, S. M. O'Malley, A. A. Sirenko, A. Kazimirov, M. Tanimura, T. Gustafsson, and S.-W. Cheong, *Nano Lett* **8**, 2, 720 (2008).
- [28] Y. Horibe, T. Asada etc. unpulished data.

Chapter IV

Composition and Strain Effect on the Microstructure of the Mn-based Spinel

1. Introduction

In the previous chapter, we demonstrated that the spinodal decomposition as an alternative route to fabricate highly self-assembled 3D nanorods with distinguished magnetic properties down to a few nanometers. The size of CB is tunable in a fixed composition with the isothermal annealing time. In the following chapter, we will report that the size of CB is also changeable with composition. For example, CBs with the size $\sim 13 \times 9 \text{ nm}^2$ are observed in $\text{Co}_{0.5}\text{FeMn}_{1.5}\text{O}_4$. This will give an additional freedom to design the magnetic properties of CBs. At the same time, we will discuss the effect of external strain on the formation of CBs. For instance, the microstructures of the annealed polycrystal and single crystal with the same composition $\text{Co}_{0.5}\text{FeMn}_{1.5}\text{O}_4$ are distinguishable. Although both separated into cubic and tetragonal phases during the spinodal decomposition, highly ordered CBs are observed in the former, twin-like structure in the latter. We conclude that, except the internal strain from the lattice mismatch between the cubic and tetragonal phases, the formation of nanostructure is intimately related with the external strain from the grain boundaries. This finding actually provided an important clue for fabricating CBs in the ZMGO thin film [1].

2. Experimental Method

Polycrystalline samples: $\text{Co}_{0.5}\text{FeMn}_{1.5}\text{O}_4$, $\text{Co}_{0.5}\text{Fe}_{1.8}\text{Mn}_{0.7}\text{O}_4$, $\text{Co}_{0.5}\text{Fe}_{0.2}\text{Mn}_{2.3}\text{O}_4$, $\text{CoFe}_{0.55}\text{Mn}_{1.45}\text{O}_4$ and $\text{Co}_{0.4}\text{FeMn}_{1.6}\text{O}_4$ were prepared by the solid state reaction. $\text{Co}_{0.5}\text{Fe}_{1.8}\text{Mn}_{0.7}\text{O}_4$ (cubic phase) and $\text{Co}_{0.5}\text{Fe}_{0.2}\text{Mn}_{2.3}\text{O}_4$ (tetragonal phase) are the final equilibrium phases of $\text{Co}_{0.5}\text{FeMn}_{1.5}\text{O}_4$ after spinodal decomposition. The single crystals

are grown in air by floating zone method. All the isothermal annealing is done below the Jahn-Teller transition ($C' \rightarrow T'$ transformation) temperature.

3. Result and Discussion

As the aforementioned $\text{Co}_{0.6}\text{Fe}_{0.9}\text{Mn}_{1.5}\text{O}_4$, highly ordered nanorods are evenly distributed throughout the entire grain in the polycrystal $\text{Co}_{0.5}\text{FeMn}_{1.5}\text{O}_4$ (Fig. IV.1(a)), sintered at 1150 °C followed by annealing at 380 °C for 148 hours. The length of herringbones (HB) is over 200 nm, and the average size of checkerboards (CB) is $\sim 13 \times 9 \text{ nm}^2$. The magnified images of HBs and CBs are shown in Fig. IV.1(b) and (c), respectively. The insets are their corresponding diffraction patterns, confirming that the nanostructures achieved here are analogue to the previously observed patterns. The CBs consist of four different domains: two cubic domains (with different rotations, Fe-rich) and two tetragonal domains (with different orientations, Mn-rich). The chemical compositions of cubic and tetragonal domains are identified by X-ray spectrometry (EDS) to be approximately $\text{Co}_{0.5}\text{Fe}_{1.8}\text{Mn}_{0.7}\text{O}_4$ and $\text{Co}_{0.5}\text{Fe}_{0.2}\text{Mn}_{2.3}\text{O}_4$, respectively.

The dashed lines represent the habit planes (110), which are free from crystal lattice mismatch and thus do not generate elastic strain during the cubic-tetragonal ($C' \rightarrow T'$) transformation. As we clearly see that the CBs are arranged along the softest elastic direction. The arrows show the zigzag arrangement of the adjacent nanorods, which are along the c axis of the tetragonal T phase.

According to the compositional identification on the C and T phases by EDS, we made $\text{Co}_{0.5}\text{Fe}_{1.8}\text{Mn}_{0.7}\text{O}_4$ and $\text{Co}_{0.5}\text{Fe}_{0.2}\text{Mn}_{2.3}\text{O}_4$ by the identical heat treatment we did on $\text{Co}_{0.5}\text{FeMn}_{1.5}\text{O}_4$. The XRD of the annealed $\text{Co}_{0.5}\text{FeMn}_{1.5}\text{O}_4$, (Fig. IV.2(a)) displays two

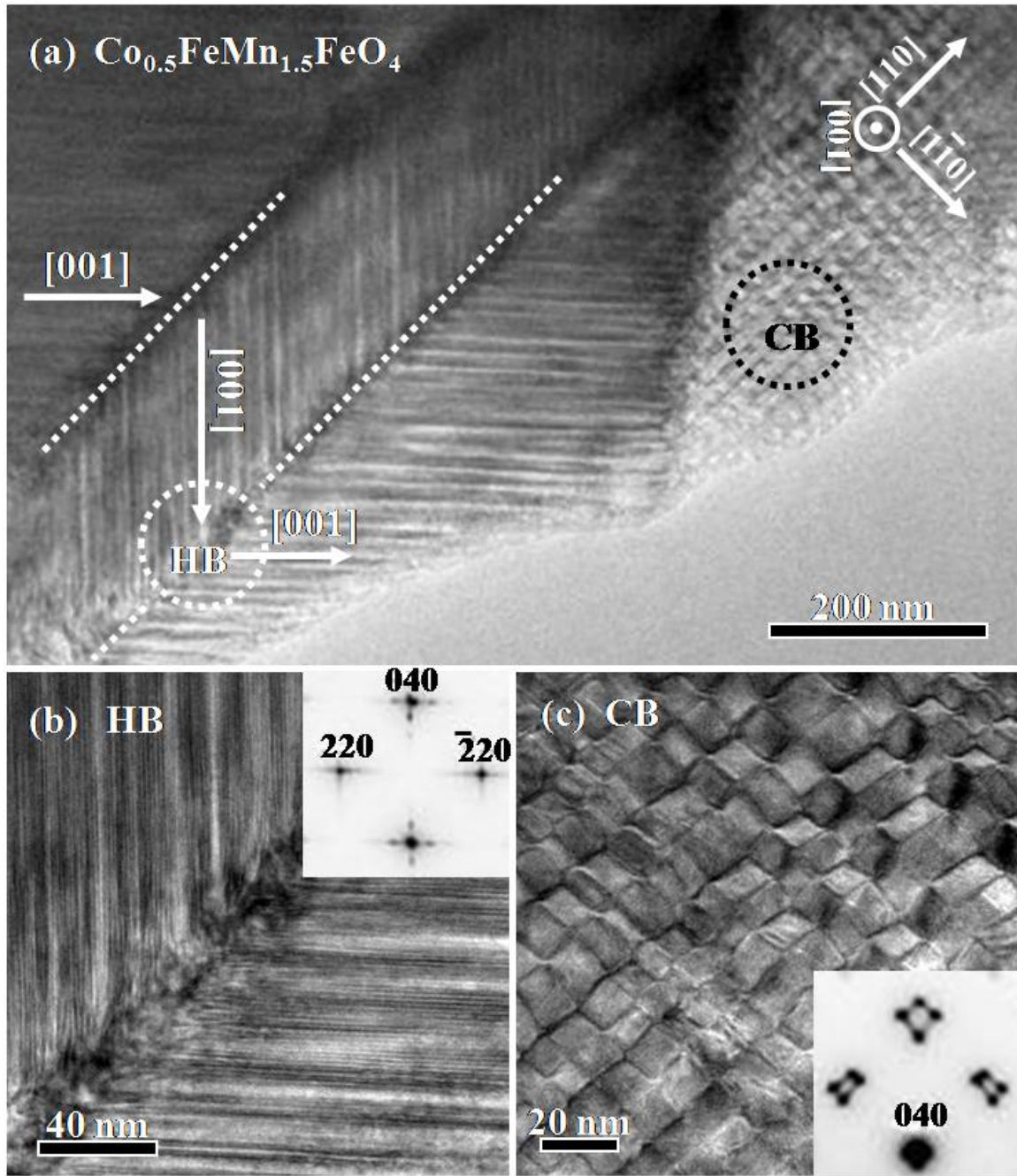


FIG. IV.1. (a) Bright field TEM images of the annealed polycrystal $\text{Co}_{0.5}\text{FeMn}_{1.5}\text{O}_4$. Coexisting nanoscale CB and HB domains, the dashed lines indicate the habit plane formed in the cubic to tetragonal transformation, arrows indicate the [001] direction of cubic phase; (b) and (c) Expanded views of HBs (the bottom circled region) and CBs (the upper circled region). The insets are the corresponding diffraction patterns.

sets of peaks. One is due to the cubic C phase, another tetragonal T phase. Compared with the sharp peaks in the single C and T phase, the broadening of the peaks in the annealed $\text{Co}_{0.5}\text{FeMn}_{1.5}\text{O}_4$ indicates the emergence of nanostructure in the sample.

All of the samples are annealed at a temperature between the two cubic-tetragonal ($C' \rightarrow T'$) transition temperatures 660 K and 630 K, which refer to the transition temperatures in the overheated and supercooled processes, respectively, as shown in the measurement of resistivity vs. temperature (Fig. IV.2(b)). The two transitions bound the temperature hysteresis range. The annealing temperature 648K (380 °C) is the equilibrium of the first-order transformation temperature, falling in between the two temperatures. Annealing above the JT transition temperature is not able to induce the spinodal decomposition. The characteristic length scale of spinodal decomposition is

determined by $\lambda \propto \left(-\frac{\partial^2 f}{\partial^2 c} \right)^{-1/2}$, where f is the free energy and c is the chemical

concentration. $\frac{\partial f}{\partial c}$ is strongly temperature dependence, which gets more negative with decreasing temperature. Herein, finer scale microstructures might be obtained by annealing samples at lower temperature. However, annealing at low temperature will not provide enough energy for the ion diffusion because the free energy barrier will increase associated with the appearance of infinitesimal heterogeneous structures [2].

Fig. IV.2(c) shows the magnetization vs. magnetic field at 300 K for the annealed $\text{Co}_{0.5}\text{FeMn}_{1.5}\text{O}_4$ (in red line) and its separated phases (C phase is in black, T phase in blue). Although all of the three samples are prepared by the identical condition, the magnetic behavior is completely different. The most impressive feature is that the coercivity of the annealed $\text{Co}_{0.5}\text{FeMn}_{1.5}\text{O}_4$ is much higher than those of its equilibrium

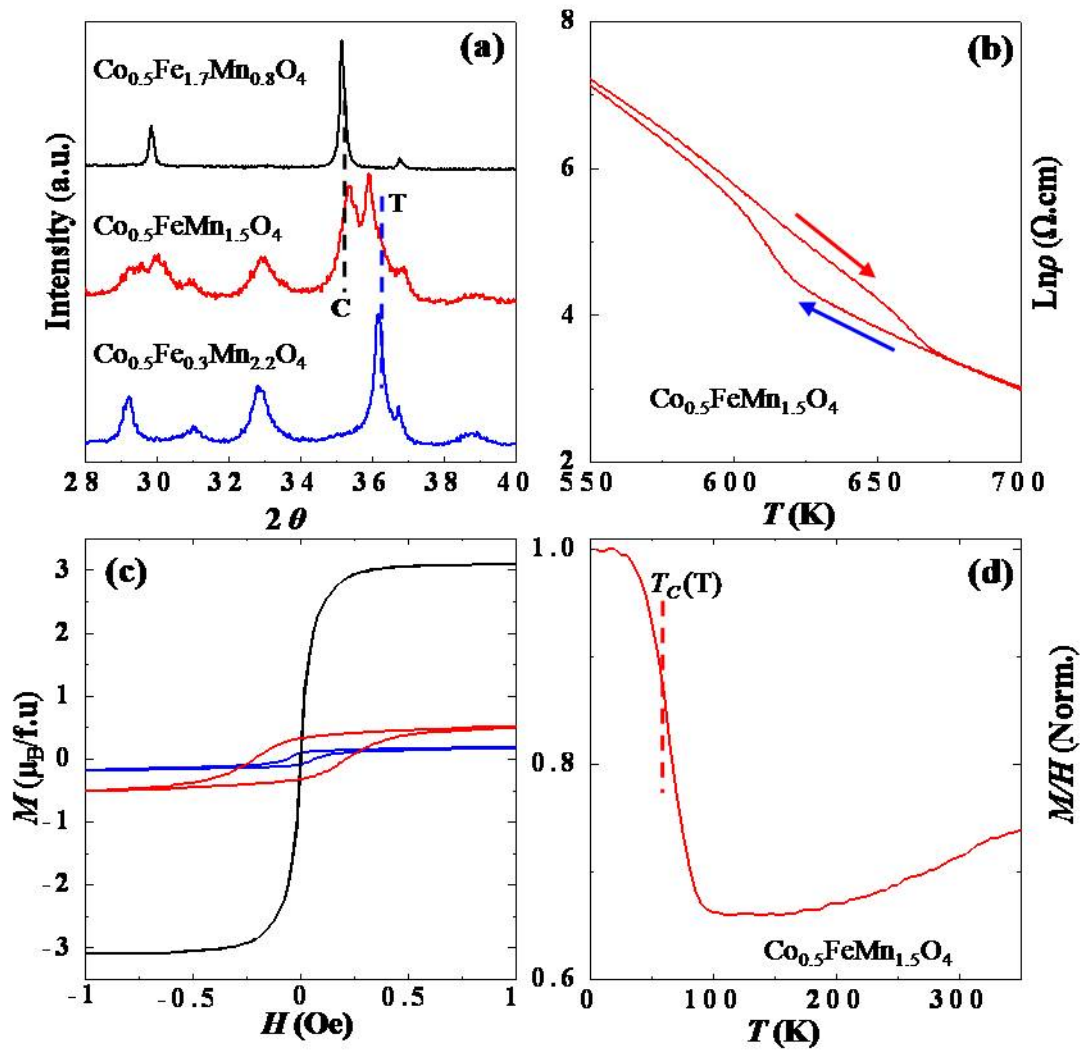


FIG. IV.2 (a) XRD patterns of $\text{Co}_{0.5}\text{FeMn}_{1.5}\text{O}_4$, $\text{Co}_{0.5}\text{Fe}_{1.7}\text{Mn}_{0.8}\text{O}_4$ (cubic) and $\text{Co}_{0.5}\text{Fe}_{0.3}\text{Mn}_{2.2}\text{O}_4$ (tetragonal). All of them have identical heat treatment. The latter two compositions are the spinodal separated phases of $\text{Co}_{0.5}\text{FeMn}_{1.5}\text{O}_4$. The dashed line indicates the peak shift of C and T phases. (b) The measurement of $\ln\rho$ vs. temperature. The arrows indicate the warming and cooling processes. (c) $M(H)$ for the three samples at room temperature. (d) Normalized M/H vs. temperature of the annealed $\text{Co}_{0.5}\text{FeMn}_{1.5}\text{O}_4$ with 200 Oe field cooling.

compositions. It gives direct evidence that the appearance of nanostructure could significantly improve the magnetic properties.

Fig. IV.2(d) is the susceptibility vs. temperature for the annealed $\text{Co}_{0.5}\text{FeMn}_{1.5}\text{O}_4$. The transition at ~ 65 K is supposed to be the T_C of the T phase. While another transition due to the C phase is above 600 K. Hence, the magnetic C domains are embedded in the nonmagnetic T domains at the room temperature, which architecture is exactly we are searching for.

In the spinodal decomposition, the microstructure evolution is related with the grain boundary energies γ of separated phases. We studied on the $\text{Co}_{0.5}\text{FeMn}_{1.5}\text{O}_4$ polycrystal sintered at 1200 °C followed by annealed at 385 °C for 357 h. The average grain size is supposed to be slightly larger than that of the sample sintered 1150 °C with showing nice CBs (Fig. IV.1(a)). Analogous study is also carried on single crystal with the same composition. From the XRD (Fig. IV.3(a)), phase separation takes place in all the three samples as illustrated by two sets of peaks. However, the microstructure in the sample sintered at 1200 °C (Fig. IV.3(b)) is largely different from the observation in the sample sintered at 1150 °C. Instead of CBs, crossed domains are observed, which look like alternately stacked lamina. The crossed diffusive spots in the diffraction pattern (Fig. IV.3(c)) is also different from the split four spots pattern of the CBs in the sample sintered at 1150 °C (the inset of Fig. IV.1(c)).

In the single crystal annealed at 385 °C for 398 h, crossed domains have been observed (Fig. IV.4(a)). Fig. IV.4(b) is the expanded view of the domains. The corresponding diffraction pattern shows the similarity with that of the sample sintered at 1200 °C (Fig. IV.3(c)). It confirms that the domains formed in the polycrystal sintered

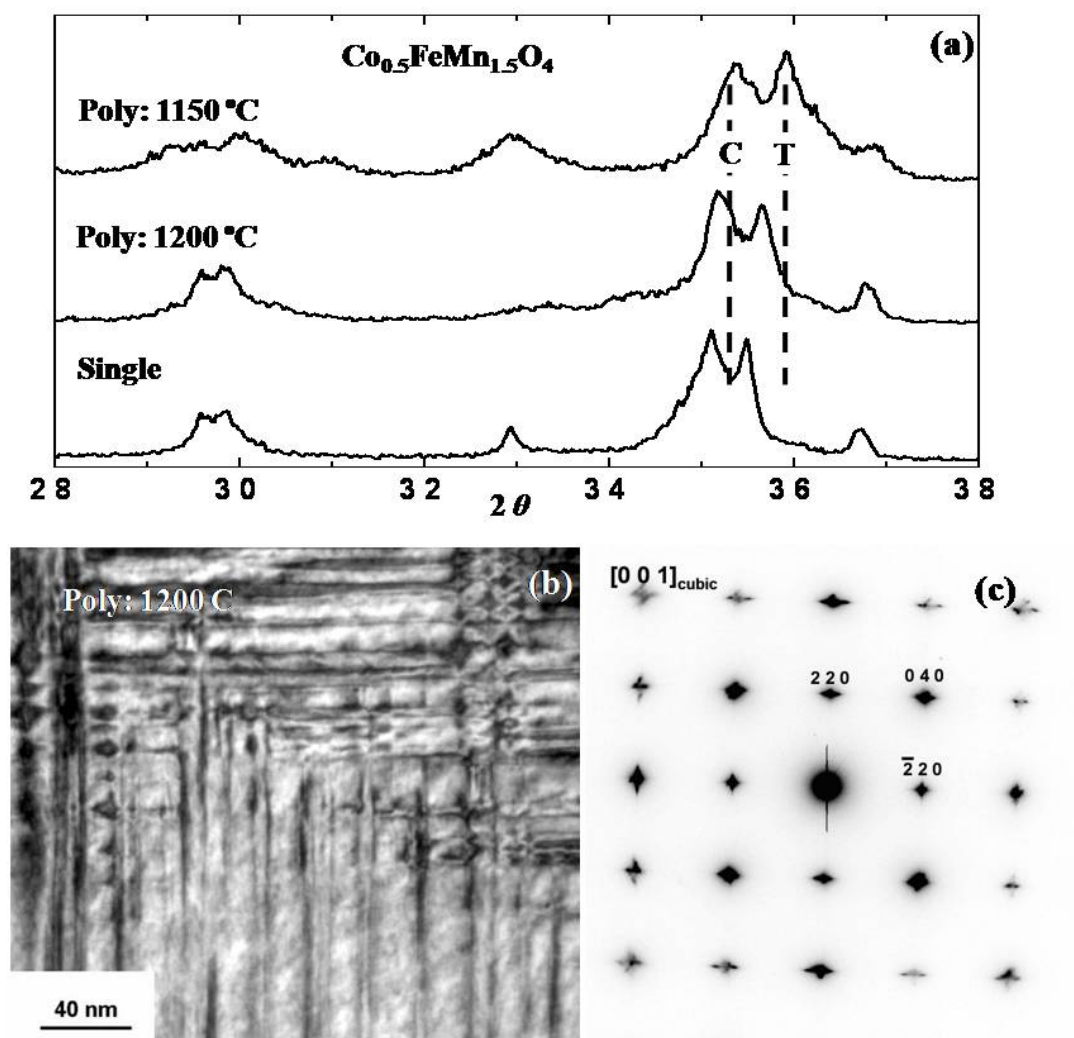


FIG. IV.3 (a) XRD of the annealed $\text{Co}_{0.5}\text{FeMn}_{1.5}\text{O}_4$ polycrystal sintered at different temperatures and annealed single crystal. (b) and (c) Bright field TEM image and diffraction pattern of the polycrystal sintered at 1200 °C.

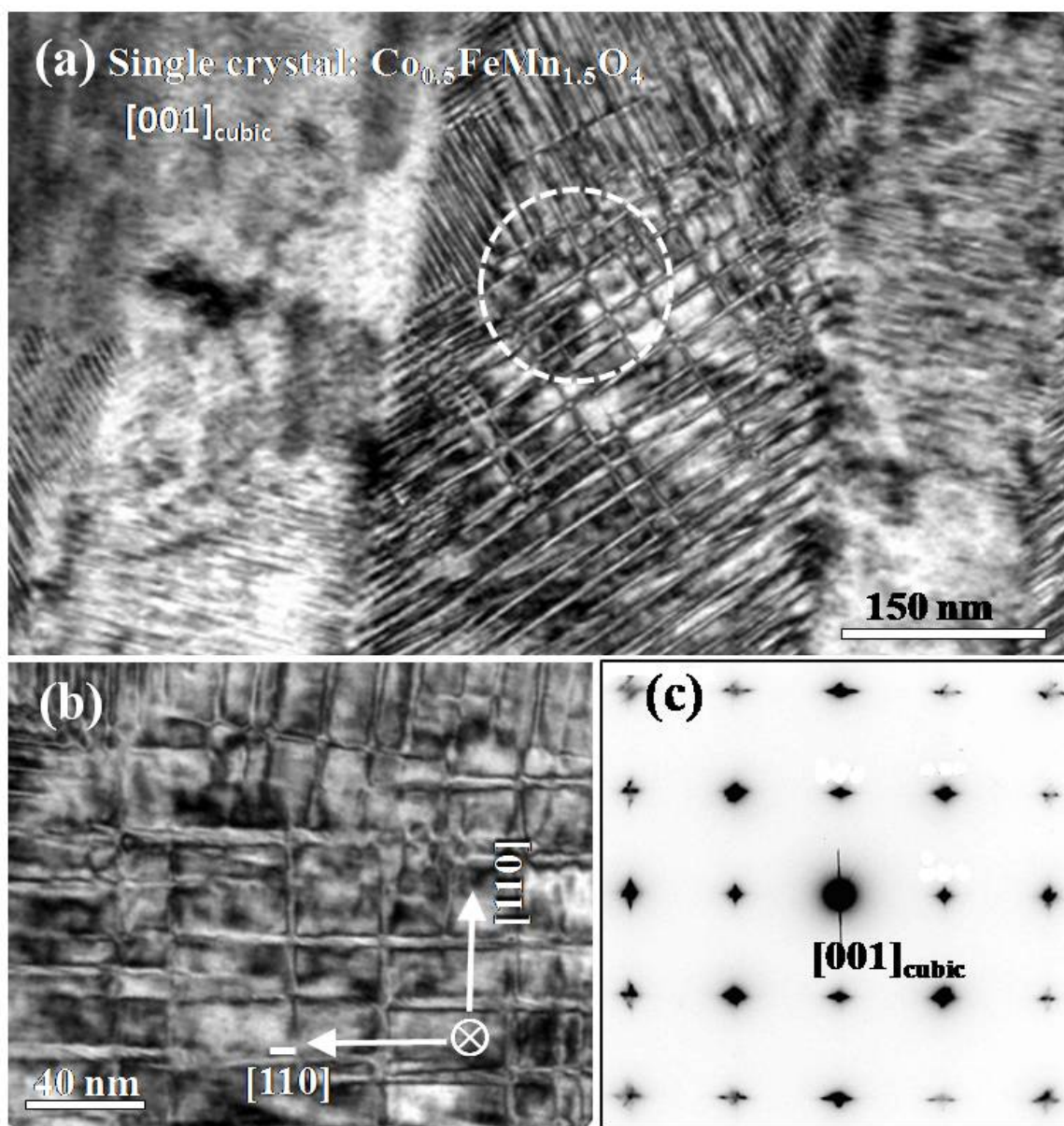


FIG. IV.4 (a) Bright field image of the annealed $\text{Co}_{0.5}\text{FeMn}_{1.5}\text{O}_4$ single crystal. (b) Expanded view the circle region in (a). (c) The diffraction pattern.

at 1200 °C are basically the same with that in the single crystal. From their TEM images, the scale of phase separations is large, which is consistent with their sharp peaks in their XRD.

From the above comparison of microstructures formed in the polycrystal and single crystal with the same composition, it unambiguously shows that grain boundary effect is critical in the formation of CBs. Generally during spinodal decomposition, the microstructure evolution in polycrystals and single crystals are different depending on the grain boundary energy of separated phases. In the polycrystals with fine grains, the phase separation assisted with grain boundaries is fast. The initial composition fluctuation is large due to the high concentration of defects and dislocations at the grain boundaries. The composition wave propagates throughout the entire grain. In the case of larger grain, grain boundary-assisted phase separation occurs in the regions close to the grain boundaries, in contrast, normal spinodal decomposition happens in the grain interior. In a single crystal without grain boundaries, only normal spinodal decomposition takes place. The initial fluctuation in composition is small [3]. The progress of diffusion is much slower compared with that in the polycrystals and takes much longer time to reach equilibrium state. The above qualitative analysis is in good agreement with the observation in the XRD and TEM. The annealing time of the single crystal is 398 h (Fig. IV3(a)). In order to induce well phase separation, much longer annealing time is obviously needed in the single crystal than polycrystals. The phase separation in the single crystal also extends in much larger scale. This finding provides important clue for properly selecting substrates in the thin film growth.

By fixing the concentration of Mn ~ 1.5 , we further change the relative concentration of Co and Fe. Phase separation occurs in the $\text{CoFe}_{0.55}\text{Mn}_{1.45}\text{O}_4$ polycrystal. The two separated phases are $\text{Co}_{1.1}\text{Fe}_{0.7}\text{Mn}_{1.2}\text{O}_4$ (cubic) and $\text{Co}_{0.9}\text{Fe}_{0.5}\text{Mn}_{1.6}\text{O}_4$ (tetragonal), respectively. From the [001] axis of the cubic phase, we observed a checkerboard-like pattern circled by dashed line (Fig. IV.5(a)). In fact, the pattern consists by crossed different domains. Because the edges of CBs should arrange along either [110] or $[1\bar{1}0]$ direction, however the seeming CBs are arranged 45° away from these directions. Rotating the sample to [111] direction, beautiful twin-like structures (Fig. IV.5(b)) show up analogous to the polytwinned microstructure in Fe-Pd alloy during the cubic-tetragonal (disorder-order) transformation [4]. More precisely, we should temporarily call them lamina since it is a mixture of phases. The fine lamina also gives rise to broadening of peaks in the XRD. Therefore, the broadening of peaks in the XRD is not a reliable indication of forming CBs in polycrystals. Moreover, we notice that the fine lamina formed here is much finer than that in the single crystal $\text{Co}_{0.5}\text{FeMn}_{1.5}\text{O}_4$ (Fig. IV.4(a)). This might be due to the small lattice mismatch between the final equilibrate phases in which the difference in compositions is small.

In the corresponding single crystal with the same composition, we observed twin-like structure although there is an indication of phase mixture in the XRD. By magnifying the circled region in Fig. IV.5(c), we clearly see the fine twin structure (Fig. IV.5(d)). In certain local area, the fine twins are interlaced with each other as confirmed by the crossed diffusive spots in the diffraction pattern (the inset of Fig. IV.5(d)). This kind of 90° -ordered domains is generally observed in other spinel systems such as $\text{Co}_{1.6}\text{Mn}_{1.4}\text{O}_4$ (Fig. IV.6(a)) and $\text{Fe}_{0.9}\text{Mn}_{2.1}\text{O}_4$ (Fig. IV.6(b)). This illuminates that the all twin-like

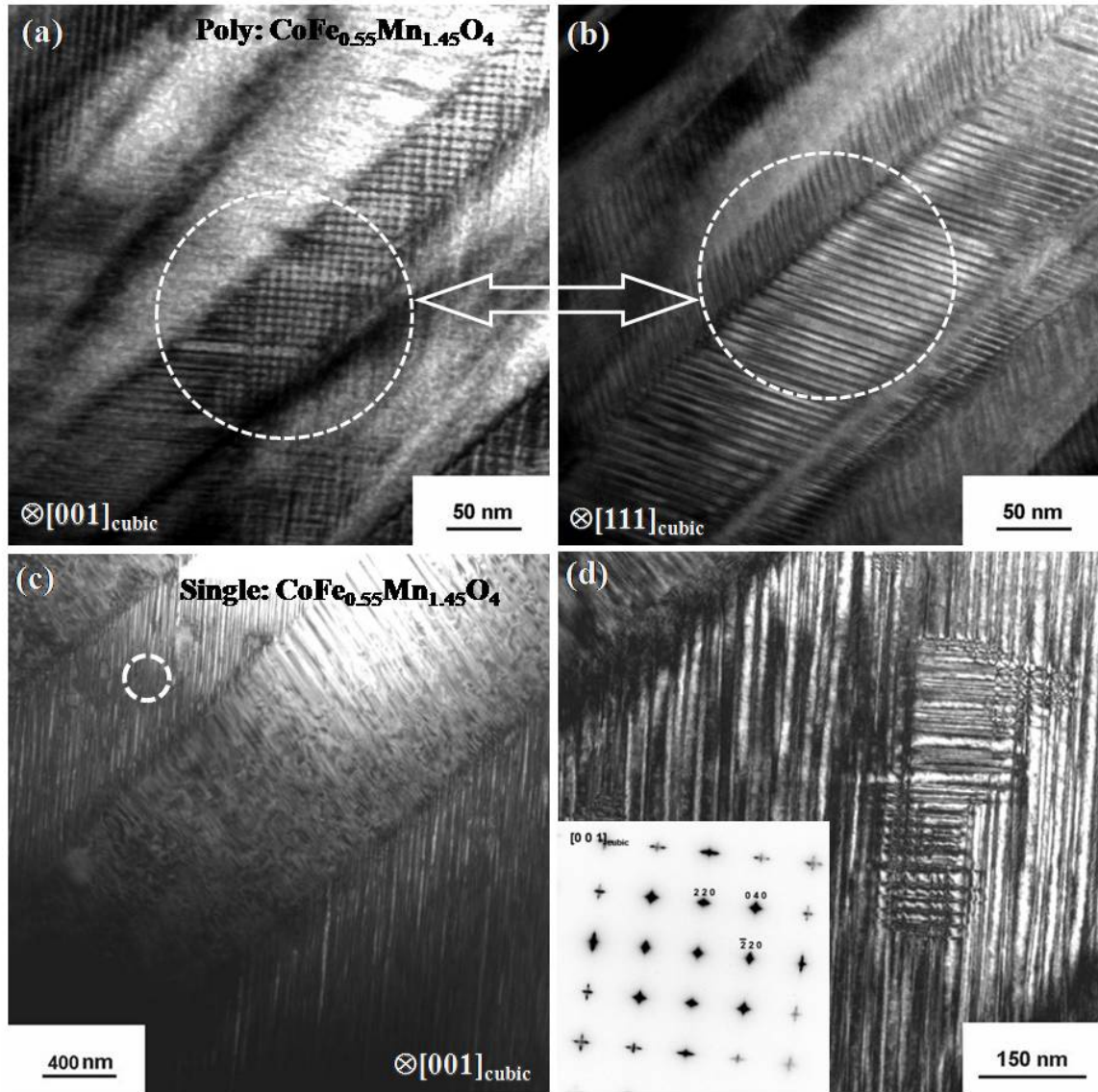


FIG. IV.5 (a) and (b) Bright field image of $\text{CoFe}_{0.55}\text{Mn}_{1.45}\text{O}_4$ polycrystals viewed from $[001]$ and $[111]$ directions of C phase. (sample made by S. Yeo) (c) Bright field image of $\text{CoFe}_{0.55}\text{Mn}_{1.45}\text{O}_4$ single crystal. (d) The high magnification image of the circled region in (c).

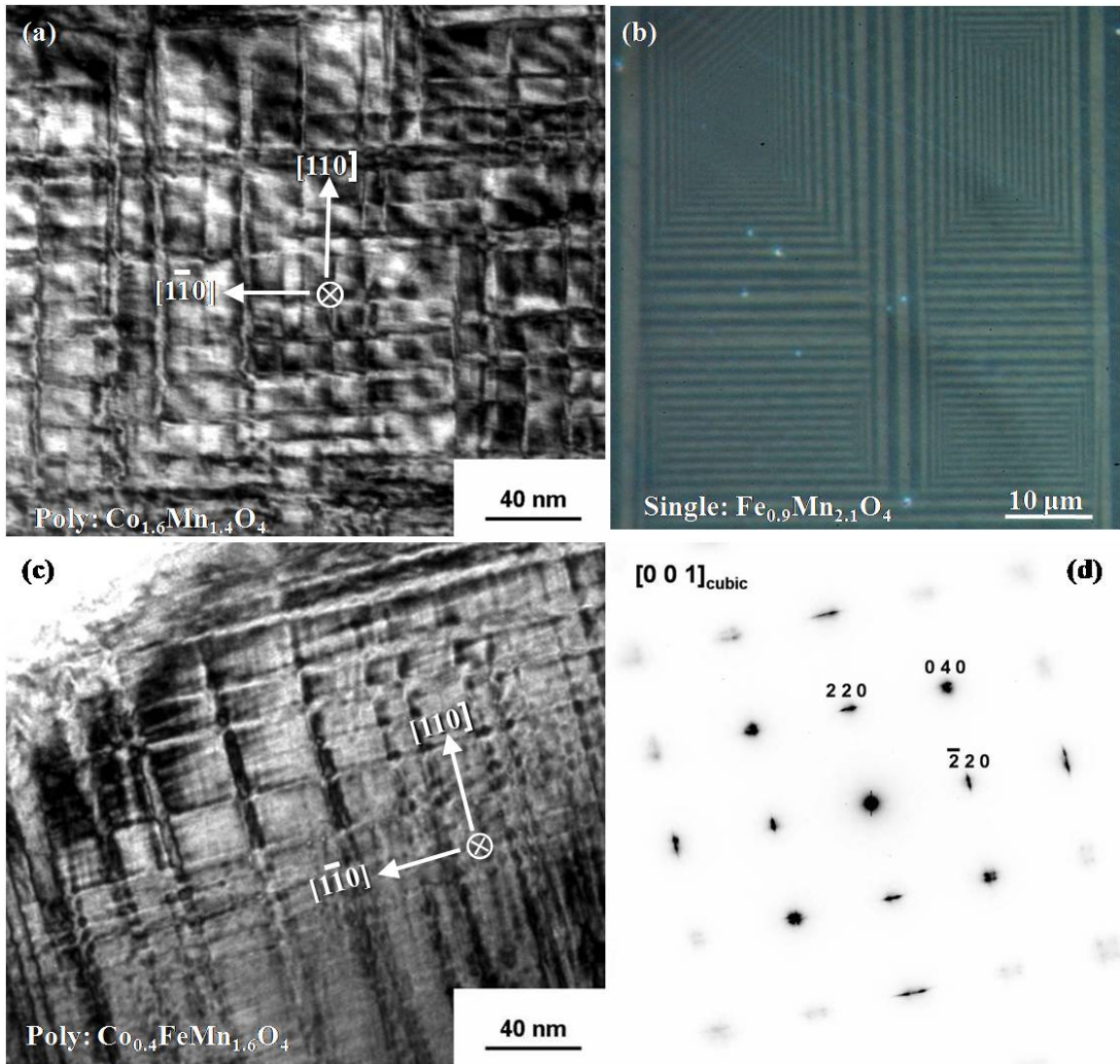


FIG. IV.6 (a) Bright field image of the annealed $\text{Co}_{1.6}\text{Mn}_{1.4}\text{O}_4$ polycrystal. (b) The optical picture of the annealed $\text{Fe}_{0.9}\text{Mn}_{2.1}\text{O}_4$ single crystal along the growth direction. (c) and (d) Bright field image of annealed $\text{Co}_{0.4}\text{FeMn}_{1.6}\text{O}_4$ polycrystal and the diffraction pattern, respectively.

structures observed so far either in polycrystals or single crystals are basically the same in nature but with different scales. Furthermore, the absence of nano CBs in $\text{Co}_{1.6}\text{Mn}_{1.4}\text{O}_4$ and $\text{Fe}_{0.9}\text{Mn}_{2.1}\text{O}_4$ indicates the formation of CBs is a very special case in terms of chemical composition. It takes place only in a system with three species of cations such as $(\text{Co}, \text{Fe}, \text{Mn})_3\text{O}_4$.

As we see from Fig. III.1(a) and Fig. IV.1(a), the size of CBs is tunable by fixing the Mn concentration but changing the relative concentration of Co and Fe. Here, we attempt to tune the size of CBs by fixing the concentration Fe but changing the relative concentration of Co and Mn. We found that the microstructure is extremely sensitive to the variation of Mn concentration. As shown in the TEM image of $\text{Co}_{0.4}\text{FeMn}_{1.6}\text{O}_4$ (Fig. IV.6(c)), the morphology is remarkably distinct from the previous CBs we observed. Although four spots, a characteristic of CBs, appear in the diffraction pattern (Fig. IV.6(d)), it is more or less like a mixture of tweed and crossed twins.

4. Conclusion

The microstructure in the Mn-based CoFe_2O_4 is extremely sensitive to the compositions. The morphology is drastically changed with the chemical composition. In the $\text{Co}_{0.5}\text{FeMn}_{1.5}\text{O}_4$ polycrystal, we observed well ordered CBs with $\sim 13 \times 9 \text{ nm}^2$. However, in the $\text{CoFe}_{0.55}\text{Mn}_{1.45}\text{O}_4$ polycrystal, twin-like structure was observed implying that the concentration of Co is important in the formation of CBs. Furthermore in the $\text{Co}_{0.4}\text{FeMn}_{1.6}\text{O}_4$ polycrystal, a mixture of twin and tweed was observed demonstrating the sensitivity of microstructure on the concentration of Mn. In neither $\text{Co}_{1.6}\text{Mn}_{1.4}\text{O}_4$ nor $\text{Fe}_{0.9}\text{Mn}_{2.1}\text{O}_4$, CBs have been formed except the generally observed twin-like structures.

Based on the above extensive search, we conclude that the formation of CB pattern is limited in a specific system with a very narrow concentration range. It does not universally happen in Mn-based spinel. Therefore, the CB patterns we observed are rare. Meanwhile, we found that the external strain originating from the grain boundaries might play an important role in the formation of CBs because crossed domains instead of CBs appear in the $\text{Co}_{0.5}\text{FeMn}_{1.5}\text{O}_4$ single crystal. This finding will provide useful information in the fabrication of CBs in thin films.

5. References

- [1] S. Park, Y. Horibe, T. Asada, L. S. Wielunski, N. Lee, P. L. Bonanno, S. M. O'Malley, A. A. Sirenko, A. Kazimirov, M. Tanimura, T. Gustafsson, and S.-W. Cheong, *Nano Lett* **8**, 2, 720 (2008).
- [2] A. G. Khachaturyan, *Theory of Structural transformations in solids* (Wily, New York, 1983).
- [3] H. Ramanarayan, T. A. Abinandanan, *Physica A*. **318**, 213, 90 (2003).
- [4] B. Zhang and W.A. Soffa. *IEEE Trans. Magn.* **27**, 6 (1991).

Chapter V

Conclusion

The achievement of the unprecedented high degree of ordered nano CBs in Mn-based CoFe_2O_4 is certainly not the end of this work, but a starting point to exploit more interesting phase separations in other spinels by harnessing JT distortion. In the rest of this thesis, we will make a brief conclusion on it and try to outline what might be interesting to be done in the future in this field.

In the first chapter, we mainly reviewed phase separation in oxides. Self-assembled nanoscale CBs through phase separation are also observed in a few metallic systems such as Co-Pt, Ni-V etc. However, it is an exotic case in oxides such as the (Li, Nd) TiO_3 perovskite system. Particularly, the observation of 3D nanorods with cross section checkerboard-like in the normal spinel ZnMnGaO_4 exhibits an alternative method to fabricate highly ordered nanostructure, except the conventional top-down and bottom-up methods. The solid state reaction utilized to fabricate nano CBs involves in a spinodal decomposition from a high temperature cubic phase into a new cubic phase poor with Mn^{3+} and a new tetragonal phase rich with Mn^{3+} .

Although ZMGO exhibits a beautiful nano CB pattern, unfortunately, the separated phases are nonmagnetic. Therefore, we focus on searching for magnetic nano CBs in Mn-based spinels starting from the second chapter. In the mixture of two inverse spinels MgFe_2O_4 (FM, $T_C \sim 713$ K) and MgMn_2O_4 (nonmagnetic down to low temperature), partially ordered checkerboards have been observed. In spite that the CBs are ordered not as well as that in ZMGO, it confirms the generality of fabricating a microstructure characterized with checkerboards in Mn-based spinels by the simple solid state reaction no matter whether they are normal or inverse spinels. Meanwhile, the coercivity of

samples with checkerboards is significantly improved compared with the parent compound without nanostructures.

In the third chapter, we discussed about Mn-based CoFe_2O_4 systems based on the consideration of the ionic size effect on the substitutional diffusion. Because the difference in ionic size remarkably affects the ionic mobility, usually, the larger the ionic size, the more difficult it is to diffuse. The three species of cations have quite similar ionic sizes leading to a small chemical fluctuation in the separated phases. Therefore, the strain field should be periodic. The excellent magnetic properties of CoFe_2O_4 such as high T_C and moderate magnetic coercivity are also included in our consideration. The CB pattern shows almost an ideal prototype of architecture for patterned recording media, which are constituted by two phases with distinct structural and magnetic properties. Meanwhile, the checkerboards size is facilely alterable with prolonging the isothermal annealing time at a fixed composition. A 3D stochastic phase field microelasticity (PFM) model is harnessed to understand the underlying physics in the formation of CBs, in which a tweed structure is proposed as a template for the formation of CBs. However, in the as-grown ZMGO thin film, we observed that the metastable tetragonal phase serves as the template for the CBs.

In the fourth chapter, we report that the size of CBs is also tunable with the composition. By comparing the microstructure in the annealed polycrystal and single crystal with the same composition $\text{Co}_{0.5}\text{FeMn}_{1.5}\text{O}_4$, we found that the formation of nano CBs is related with the stress from the grain boundaries. We also found that the formation of CBs is not a universal case in the Mn-based spinels as we thought before. The appearance of the unique pattern is limited in a very narrow window of composition

region. In terms of the underlying mechanism, the formation of CBs is a rare case, which is largely different from the CBs observed before.

Although highly ordered nano CBs have been fabricated in the Mn-based CoFe_2O_4 , a lot of more work can be done in the future. The conventional solid state reaction accompanied with a spinodal decomposition induced by J-T distortion has been confirmed as a way to fabricate nano CBs in Mn-based either normal or inverse spinels. Searching a system, which could be decomposed into one phase FM and another ferroelectric (FE), or one insulated and another conductive, probably will bring forth more interesting physics in this extraordinary phase separation. Direct imaging the magnetic properties of the CBs by Lorentz TEM and fabricating the CBs of the Mn-based CoFe_2O_4 on thin films are expected to be the most meaningful work to do in the near future. Once the magnetization of each magnetic CB domain could be independently controlled by applying an external magnetic field, it would provide a new platform to design patterned magnetic recording medium. The explanation of the formation of CBs is far from clear at present. Taking into account of the contributions from the external strain and J-T distortion might help to make the 3D PFM model more precisely to describe the evolution of the microstructure with the isothermal annealing time.

Appendix I.

APPLIED PHYSICS LETTERS 90, 133123 (2007)

Coercivity and nanostructure in magnetic spinel $\text{Mg}(\text{Mn}, \text{Fe})_2\text{O}_4$

C. L. Zhang, S. Yeo, Y. Horibe, Y. J. Choi, S. Guha, M. Croft, and S.-W. Cheong^{a)}
Rutgers Center for Emergent Materials, Rutgers University, Piscataway, New Jersey 08854 and Department of Physics and Astronomy, Rutgers University, Piscataway, New Jersey 08854

S. Mori

Department of Physics, Osaka Prefecture University, 1-1 Gakuen-cho, Sakai, Osaka 599-8531, Japan

(Received 7 January 2007; accepted 24 February 2007; published online 30 March 2007)

When Fe ions in the ferrimagnetic cubic MgFe_2O_4 are replaced by Jahn-Teller (JT)-active Mn ions, the structure evolves with two-step processes. For example, the quenched cubic $\text{MgMn}_{1.5}\text{Fe}_{0.5}\text{O}_4$ becomes tetragonal and JT distorted with slow cooling. However, with further slow cooling, the clustering tendency of JT-distorted Mn ions induces the formation of a checkerboard nano-self-assembly consisting of Mn-rich (tetragonal, paramagnetic) and -poor (cubic, ferrimagnetic) rods. This morphological evolution accompanies a drastic modification of ferrimagnetic properties, e.g., the magnetic coercivity changes by ~ 25 . The nanocheckerboard assembly with ferrimagnetic nanorods with large shape anisotropy can be a platform for ultra high-density memory devices. © 2007 American Institute of Physics. [DOI: 10.1063/1.2717568]

The electronic degeneracy of ions such as Mn^{3+} or Cu^{2+} can be lifted by a Jahn-Teller (JT) distortion, when the electronic energy gain can overcome the structural energy cost.¹ This JT effect can be associated with intriguing physical phenomena such as the colossal magnetoresistance effect in perovskite manganites and high temperature superconductivity in layered cuprates.²⁻⁴ Furthermore, the JT effect can couple to chemical phase separation by inducing a miscibility gap in the system with mixed JT and non-JT ions, leading to spatially separated regions with higher and lower JT ion concentrations.⁵ One extraordinary example of JT-induced phase separation was observed in the spinel $\text{Zn}(\text{Mn}, \text{Ga})_2\text{O}_4$ (ZMGO), where a truly nanoscale and well ordered structure is stabilized by the phase separation. The nanostructure consists of two types of long square rods with different Mn concentrations that are alternatively stacked with long-range periodicity, and thus its cross section shows a checkerboard (CB) pattern.⁶ Crystallographically, the nano-CB of ZMGO is truly remarkable, but does not constitute a technological advance in a “magnetic” sense because ZMGO is basically paramagnetic (PM) near room temperature.^{7,8}

Since “ferrimagnetic (FM)” spinel compounds are abundant,⁹ one can contemplate forming a nano-CB structure with two types of nanorods having distinct magnetic properties, ideally with one of them having a FM transition above room temperature. Such a magnetic nanostructure with large shape anisotropy is potentially useful as a medium for perpendicular magnetic recording.¹⁰ Herein, we report the realization of the magnetic nanostructure in $\text{Mg}(\text{Fe}, \text{Mn})_2\text{O}_4$. We also discuss the structural evolution of $\text{Mg}(\text{Fe}, \text{Mn})_2\text{O}_4$ as well as the change of magnetic properties with various chemical compositions and cooling rates (CR's). MgFe_2O_4 is FM with Curie temperature (T_C) of ~ 600 K, while MgMn_2O_4 is PM down to low temperatures.^{11,12} In addition, MgFe_2O_4 crystallizes in a cubic structure ($Fd3m$) with $a \approx 8.52$ Å,¹¹ but MgMn_2O_4 is tetragonal ($I4_1/amd$, due to cooperative JT distortions) with $a \approx 5.75$ Å and $c \approx 9.38$ Å.¹² Both of them are partially inverse spinels, meaning that some

of the Fe and Mn ions in $\text{Mg}(\text{Fe}, \text{Mn})_2\text{O}_4$ are located in the tetrahedral A sites.^{9,11,12}

A dozen $\text{MgMn}_x\text{Fe}_{2-x}\text{O}_4$ specimens were prepared by the solid state reaction. Stoichiometric amounts of MgO , Mn_2O_3 , and Fe_2O_3 powders were mixed and sintered at 1050 – 1250 °C three times with intermediate grindings. The final cooldown from 1250 °C to room temperature was performed with various CR, ranging from quenching in cold water to 0.3 °C/h cooling. Crystallographic structures were examined using a Rigaku x-ray diffractometer (XRD) at room temperature. A superconducting quantum interference device magnetometer was used for magnetization measurements and standard four-probe resistivity (ρ) experiments were performed. Bright field images were taken using a JEOL 2000FX transmission electron microscope (TEM) at 200 kV.

Figure 1(a) demonstrates that the CR drastically influences the magnetic hysteresis loop at 5 K for $x=1.5$. The coercivity (H_c) of the 50 °C/h cooled specimen is ~ 4700 Oe, ~ 25 times larger than that of the quenched one (~ 187 Oe). H_c vs CR reveals that it exhibits the maximum H_c [see the inset of Fig. 1(a)]. Figure 1(b) displays that the XRD patterns for $x=1.5$ significantly change with varying CR, suggesting that the H_c change is related with the structural modification. The quenched specimen is cubic, but the 50 °C/h cooled specimen is purely tetragonal, indicating a cooperative JT distortion in the entire specimen. The cubic nature of the quenched specimen may reflect that the quenching is faster than the kinetics needed to support the cooperative JT distortion. Note that in the quenched cubic specimen, there may be a significant amount of Mn ions in the A sites, which are not JT active. These non-JT-active Mn ions also contribute to the absence of cooperative JT distortions in the quenched specimen.^{13,14} In contrast, the 10 °C/h cooled specimen shows the mixture of cubic and tetragonal phases, stemming from the chemical phase separation with the clustering of the JT Mn ions in the octahedral B sites. Still slower cooling, 0.3 °C/h, produces a more distinct phase separation between the cubic and tetragonal phases.

^{a)}Electronic mail: sange@physics.rutgers.edu

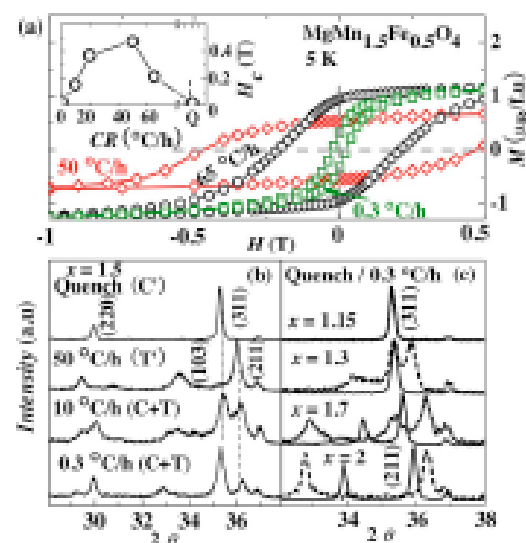


FIG. 1. (Color online) (a) $M(H)$ at 5 K for $x=1.5$ with selected CR's. The inset displays H_c vs CR. Q represents quenching in water. (b) XRD patterns for $x=1.5$ with selected CR's. C' represents the cubic phase of the quenched specimen, and the cubic peaks of (220) and (311) are denoted. T' represents the tetragonal phase of the 50 °C/h cooled specimen, and the tetragonal peaks of (003) and (211) are denoted. C and T represent the cubic and tetragonal phases after phase separation, respectively. (c) XRD patterns of the quenched (solid line) and 0.3 °C/h cooled (dashed line) specimens of selected Mn concentrations.

In order to conveniently discuss the structural change for $x=1.5$, we introduce a few notations. C' and T' are for the cubic phase of the quenched specimen and the tetragonal phase of the 50 °C/h-cooled one, respectively. Both of them are metastable, and slower cooling than 50 °C/h induces the decomposition of T' into a mixture of cubic (C) and tetragonal (T) phases. Mn concentrations in C' and T' are identical, but Mn concentration in T (C) is presumably more (less) than that in T'. Consistently, the tetragonality of T is larger than that of T', as evidenced in the XRD results. Using these notations, the structural evolution can be simplified as $C' \rightarrow T' \rightarrow C+T$ with decreasing CR. From extensive XRD studies, we have confirmed that other compositions in the miscibility gap region show a similar structural evolution by varying CR, and that C and T are the miscibility boundary compounds with compositions $\text{MgMn}_{12}\text{Fe}_{0.8}\text{O}_4$ and MgMn_2O_4 , respectively (see below).

A large H_c can be achieved by hindering the nucleation and growth of magnetization reversed domains through pinning of domain walls or increasing magnetic anisotropy.^{13,18} The magnetic anisotropy can originate from various sources such as magnetocrystalline, shape, magnetoelastic, interface, and exchange anisotropies.^{15–18} Magnetocrystalline anisotropy (MA) is commonly utilized to suppress the magnetization rotation. Presumably, C', T', and C are FM and T is PM. It is expected that the MA in the T' phase is large and in the C and C' phases is negligible. Thus, T' has the largest H_c , and the shape anisotropy of the C domains is presumed to be the main contribution to the coercivity of the C+T specimens.

Figure 1(c) shows the XRD patterns of the quenched and 0.3 °C/h cooled specimens for various concentrations. The

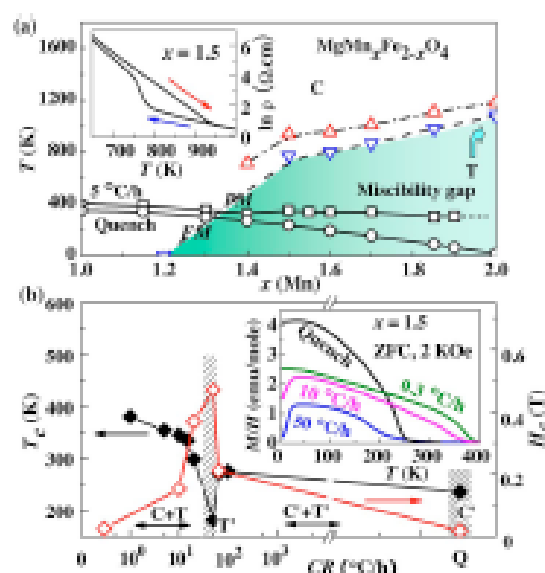


FIG. 2. (Color online) (a) Phase diagram of $\text{Mg}(\text{Mn,Fe})_2\text{O}_4$. The shaded area depicts the miscibility gap region in the 5 °C/h cooled specimens. The arrow denotes the tetragonal phase of $x=2$. Δ and ∇ denote the JT transition temperature T_{JT} upon warming and cooling, respectively. \square and \circ denote ferromagnetic T_c of the 5 °C/h cooled and quenched specimens, respectively. The inset displays $\log(\rho)$ vs temperature upon warming and cooling for $x=1.5$. (b) T_c (\blacklozenge) and H_c (\circ) vs $\log(\text{CR})$ for $x=1.5$. The mixture of C+T forms for very slow CR (the most left region). The shaded areas at the left and right hand sides represent T' and C' phases, respectively. Between the shaded regions, the mixed C+T' phase is observed. The inset displays the zero-field-cooled M/H vs temperature in $H=2$ kOe for $x=1.5$ with selected CR's.

$x=1.15$ pattern does not change with varying CR. However, for $x=1.3$, the 0.3 °C/h cooled specimen (dashed line) displays a totally different pattern from that of the quenched one (solid line), indicating that $x=1.2$ is close to one of the miscibility gap boundaries. The quenched specimens of $1.7 \leq x \leq 2$ are tetragonal (i.e., T'), while the quenched specimens of $1.2 < x < 1.7$ are cubic (i.e., C'). These results suggest that the kinetics for the cooperative JT transition for $1.7 \leq x \leq 2$ is faster than the quenching speed, while that for $1.2 < x < 1.7$ is slower than the quenching speed. The 0.3 °C/h cooled $x=1.7$ does exhibit the C-T phase separation, indicating that the other miscibility gap boundary is close to $x=2$.

Based on the results of XRD, high temperature resistivity, and magnetization experiments, the phase diagram for $\text{MgMn}_x\text{Fe}_{2-x}\text{O}_4$ [see Fig. 2(a)] has been constructed. The miscibility gap exists for $1.2 < x < 2$.¹⁹ The resistivity anomaly with thermal hysteresis in the inset of Fig. 2(a) originates from the first-order JT phase transition. The JT transition temperature upon warming (Δ) and cooling (∇) and the Curie temperature (T_c) for the quenched (C') and 5 °C/h cooled specimens (\square) are determined from sharp features in $d(\ln \rho)/dT$ and dH/dT , respectively. For $1.2 < x < 2$, the T_c 's of the 5 °C/h cooled specimens are almost independent of x . This is in good agreement with the scenario that only the amount, not chemical composition, of the C phase changes with x in phase separated specimens and that T_c is the FM transition of the C phase. On the other hand, T_c of the quenched specimens decreases monotonically with increasing x . Figure 2(b) displays how T_c (\blacklozenge) and

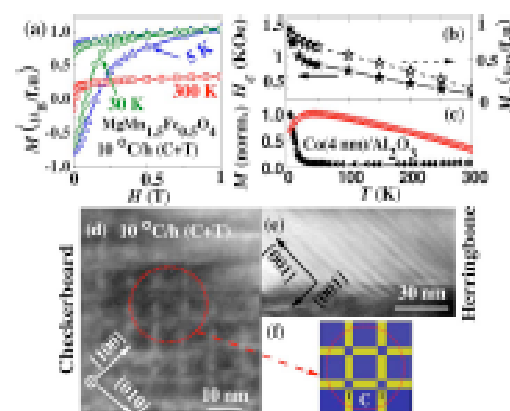


FIG. 3. (Color online) (a) $M(H)$ of the 10°C/h cooled $\text{MgMn}_{1.5}\text{Fe}_{0.5}\text{O}_4$ at selected temperatures. (b) H_c (\star) and M_r (\diamond) vs temperature. (c) Normalized M vs temperature of the 10°C/h cooled $\text{MgMn}_{1.5}\text{Fe}_{0.5}\text{O}_4$ (\diamond) and 4 nanometer size spherical Co particles embedded in Al_2O_3 matrix (\star) from Ref. 18. [(d) and (e)] TEM images of the 10°C/h cooled specimen, showing checkerboard and herringbone patterns, respectively. (f) Schematic view of the circled region in (d).

H_c (\diamond) of $x=1.5$ changes with CR. The T (50°C/h) specimen exhibits the maximum H_c and the minimum T_C . Cooling slower than 50°C/h produces the mixture of C and T, so that T_C of the mixture, fixed by that of C, is higher than that of C' and T'. The slower cooling of CR $< 50^\circ\text{C/h}$ generates a higher T_C due to the further phase separation with larger length scale. The temperature dependence of M/H of $x=1.5$ for various CR's is shown in the inset of Fig. 2(b). $M(H)$ curves at selected temperatures for the 10°C/h cooled $\text{MgMn}_{1.5}\text{Fe}_{0.5}\text{O}_4$ are shown in Fig. 3(a), and H_c and remnant magnetization (M_r), obtained from $M(H)$ curves, are displayed in Fig. 3(b). Interestingly, H_c increases abruptly below -30 K . This upturn of H_c below -30 K is apparently related with the downturn of M/H below -30 K [Fig. 3(c)].

In analogy with the observation in the 5°C/h cooled ZMGO,⁶ our TEM results show that the 10°C/h cooled $x=1.5$ specimen displays CB and herringbone (HB) patterns with a few nanometers in size, as shown in Figs. 3(d) and 3(e). As explained in Ref. 6, the CB and HB patterns are the cross sectional and side views of the self-assembled nanorods, respectively. The results in Ref. 6 along with our results of TEM, XRD, and magnetic measurements on $x=1.5$ indicate that the self-assembled nanostructure consists of two types of square nanorods with distinct magnetic properties: the cubic-phase (C) rods are FM and the tetragonal-phase (T) rods are PM. The unique self-assembly is spontaneously formed during the coherent spinodal decomposition into non-JT Fe^{3+} -rich (cubic) and JT Mn^{3+} -rich (tetragonal) phases through accommodating elastic strain induced by the lattice misfit of the two precipitated crystallographically distinct phases.^{6,20–22} Since the miscibility gap occurs for $1.2 < x < 2$, the chemical compositions of the C and T rods are expected to be closed to the miscibility gap boundaries. The lever rule for $x=1.5$ indicates that the total volume of the C rods is larger than that of the T rods, consistent with

the XRD results in Fig. 1(b) and TEM images. A schematic view of the CB structure is depicted in Fig. 3(f).

One of the main challenges to develop ultrahigh-density magnetic recording media is associated with the superparamagnetic limit due to the destabilization of magnetization direction by thermal fluctuations.²³ As shown in Fig. 3(c), spherical 4 nm size Co particles embedded in Al_2O_3 (\star) show little magnetization above -10 K .¹⁸ In contrast, the 10°C/h cooled $x=1.5$ (\diamond) exhibits a significant magnetization as well as coercivity in a wide temperature range, probably because of the large shape anisotropy of the C rods.

In conclusion, we have investigated how the JT distortions can influence the structural and magnetic properties, and induce a unique magnetically active nanocheckerboard in $\text{Mg}(\text{Mn},\text{Fe})_2\text{O}_4$ due to the clustering tendency of the JT-distorted Mn ions, which could be suitable for a ultrahigh-density perpendicular magnetic storage medium.^{21,22,24}

Work at Rutgers was supported by the NSF DMR-0405682.

¹See, for example, Isaac Bernstein, *The Jahn-Teller Effect* (Cambridge University Press, Cambridge, 2006), Chap. 3, pp. 479–566.

²E. Dagotto, *Science* **309**, 257 (2005).

³M. Uehara, S. Mori, C. H. Chen, and S.-W. Cheong, *Nature (London)* **399**, 560 (1999).

⁴M. Fahn, S. Freisem, A. A. Mazovsky, Y. Temizka, J. Aerts, and J. A. Mydosh, *Science* **285**, 1540 (1999).

⁵M. A. Ivanov, N. K. Tkachev, and A. Ya. Fainman, *Low Temp. Phys.* **25**, 459 (1999).

⁶S. Yao, Y. Horiba, S. Mori, C. M. Tseng, C. H. Chen, A. G. Khachatryan, C. L. Zhang, and S.-W. Cheong, *Appl. Phys. Lett.* **89**, 233120 (2006).

⁷A. S. Ribold, R. Seshadri, J. Eastling, and C. Fisher, *J. Phys.: Condens. Matter* **17**, 1039 (2005).

⁸S. Asabiri, A. Winkowski, L. Gerward, J. Staan Olsen, and E. Talik, *Phys. Rev. B* **60**, 12651 (1999).

⁹See, for example, F. S. Dainton, *Structure and Properties of Inorganic Solids* (Pergamon, New York, 1970), Chap. 8, pp. 220–225.

¹⁰D. A. Thompson and J. S. Bert, *IBM J. Res. Dev.* **44**, 311 (2000).

¹¹R. J. Harrison and A. Putnis, *Phys. Chem. Miner.* **26**, 322 (1999).

¹²C. B. Anzoni, M. C. Mozzati, L. Malavasi, P. Ghigna, and G. Flor, *Solid State Commun.* **119**, 591 (2001).

¹³A. J. Millin, *Phys. Rev. B* **53**, 8434 (1996).

¹⁴K. Kubo, V. Bonbers, P. Novak, R. Gumpel, and J. Simonet, *J. Magn. Mater.* **217**, 19 (2000).

¹⁵See, for example, H. Kronmüller and M. Fahnke, *Micromagnetism and The Microstructure of Ferromagnetic Solids* (Cambridge University Press, Cambridge, 2003), Chap. 6, pp. 90–147.

¹⁶J. D. Livingston, *J. Appl. Phys.* **52**, 2544 (1981).

¹⁷H. Zeng, J. Li, J. P. Liu, Z. L. Wang, and S. H. Sun, *Nature (London)* **420**, 395 (2002).

¹⁸Y. Shanyav, S. Soryanov, Y. Zhang, G. Hadjipouris, D. Givord, and J. Nogami, *Nature (London)* **423**, 850 (2003).

¹⁹See, for example, K. E. Eastling and D. A. Porter, *Phase Transformations in Metals and Alloys* 2nd ed. (CRC, Boca Raton, FL, 1992), Chap. 1, p. 33.

²⁰A. G. Khachatryan, *Theory of Structural Transformations in Solids* (Wiley, New York, 1983), Chap. 10, pp. 315–367.

²¹Y. Le Boucq, A. Loiseau, and A. G. Khachatryan, *Acta Mater.* **46**, 2777 (1998).

²²A. Suzuki and M. Takayama, *J. Mater. Res.* **21**, 21 (2006).

²³D. Weller and A. Moser, *IEEE Trans. Magn.* **35**, 4423 (1999).

²⁴H. Zhang, J. Wang, S. E. Lofland, Z. Ma, L. Mohandou-Arabi, T. Zhao, L. Salazar-Riba, S. R. Shinde, S. B. Ogale, F. Bai, D. Viehland, Y. Jin, D. G. Schlom, M. Wuttig, A. Roychoudhury, and R. Ramesh, *Science* **303**, 661 (2004).

Appendix II.

APPLIED PHYSICS LETTERS 91, 233110 (2007)

Magnetic nanocheckerboards with tunable sizes in the Mn-doped CoFe_2O_4 spinel

C. L. Zhang

Rutgers Center for Emergent Materials and Department of Physics and Astronomy, Rutgers University, Piscataway, New Jersey 08854, USA

C. M. Tseng^{*}

Center for Condensed Matter Sciences, National Taiwan University, Taipei 10617, Taiwan

C. H. Chen

Center for Condensed Matter Sciences and Department of Physics, National Taiwan University, Taipei 10617, Taiwan and Institute of Atomic and Molecular Sciences, Academia Sinica, Taipei 10617, Taiwan

S. Yeo, Y. J. Choi, and S.-W. Cheong

Rutgers Center for Emergent Materials and Department of Physics and Astronomy, Rutgers University, Piscataway, New Jersey 08854, USA

(Received 26 October 2007; accepted 15 November 2007; published online 6 December 2007)

Formation of magnetically ordered array of two types of rectangular nanorods, ~ 300 nm in length and a few nanometers in size, is achieved in the Mn-doped CoFe_2O_4 spinel through chemical phase separation mediated by cooperative Jahn-Teller distortions. At room temperature, the magnetic nanorods, with composition close to CoFe_2O_4 , interlace with the paramagnetic counterparts and form a highly organized checkerboard pattern in the cross section. The checkerboard size in the range of $\sim 13.8 \times 7.9 - \sim 17.3 \times 14.0$ nm² is tunable with composition and, particularly, with the isothermal annealing time. These three-dimensional nanocheckerboards exhibit a nearly ideal configuration for the patterned perpendicular recording medium. © 2007 American Institute of Physics. [DOI: 10.1063/1.2821838]

Recently, organized nanostructure in the nonmagnetic normal spinel system $\text{ZnMn}_2\text{Ga}_{1-x}\text{O}_4$ has been fabricated by a chemical phase separation.¹ This pioneering work demonstrated that solid state self-assembly mediated by cooperative distortions of Jahn-Teller (JT) ions (Mn^{2+}) could produce an ordered nanostructure through spinodal decomposition in which two distinct types of square rods, with different Mn concentrations but comparable sizes, were interlaced to form a cross-sectional checkerboard pattern. This emergent method provides an alternative route to fabricate ordered nanostructures, which are usually achieved by the conventional bottom-up and top-down techniques.^{2,3} However, highly ordered and densely packed magnetic nanocrystals with tunable sizes, which are indispensable for nanotechnology applications, have not yet been demonstrated using this unique method, despite an earlier report of a similar, but poorly ordered nanostructure in a magnetic inverse spinel system $\text{Mg}(\text{Mn}_x\text{Fe}_{1-x})\text{O}_4$.⁴ CoFe_2O_4 is an outstanding permanent magnet with high coercivity and moderate magnetization, showing great potential in magnetic recording applications.⁵ In the past few years, tremendous work has been devoted to fabricate its nanostructures with diverse geometries.⁶⁻⁸ Yet, no highly ordered nanostructure has been realized.

In this study, we focused on a magnetic spinel system Mn-doped CoFe_2O_4 (with nominal composition $\text{Co}_{0.8}\text{Fe}_{0.8}\text{Mn}_{1.2}\text{O}_4$), which can be viewed roughly as a proper mixture of CoFe_2O_4 and CoMn_2O_4 compounds. At room temperature, CoFe_2O_4 adopts a cubic ferromagnetic phase

($a \sim 8.3$ Å, $T_c \sim 800$ K)^{9,8} and CoMn_2O_4 adopts a tetragonal paramagnetic phase ($a \sim 8.1$ Å, $c \sim 9.3$ Å, $T_c \sim 100$ K).⁹

Compared with our previous work on the $\text{Mg}(\text{Mn}_x\text{Fe}_{1-x})\text{O}_4$ system,⁴ the magnetic nanocheckerboards achieved here are tunable in size, much better organized, and exhibit more than ten times larger coercivity at room temperature. Therefore, these nanocheckerboards offer a superior prototype for the ultrahigh density magnetic recording media.¹⁰

The polycrystals $\text{Co}_x\text{Fe}_{1-x}\text{Mn}_{1.5}\text{O}_4$ ($x=0.5, 0.6$) were prepared by solid state reaction. Co_3O_4 , MnO_2 , and Fe_2O_3 were mixed and sintered at $900-1150$ °C, followed by quenching into air (or ice water), and isothermally annealing with different periods of time. The details of the sample characterization were described elsewhere.^{1,4}

The annealing time was found to have the most critical effect on the microstructure of the Mn-doped CoFe_2O_4 . We will first discuss the ordered overall nanostructure in the form of long rectangular nanorods observed in the $\text{Co}_{0.8}\text{Fe}_{0.8}\text{Mn}_{1.5}\text{O}_4$ sample annealed at 375 °C for 324 h, as shown in Fig. 1(a). Nanorods are periodically stacked in a particular way such that the side view is herringbone (HB)-like with length of ~ 300 nm, and the cross-sectional view is checkerboard (CB)-like with the average size of $\sim 15 \times 10$ nm². The diffraction pattern of the HB (the bottom inset) shows densely packed superlattice spots on a streaking diffuse background. The periodicity of the superlattice spots is ~ 18 nm, close to the distance between dark/bright fringes of HBs and the diagonal length of the CBs [Fig. 1(b)]. The four types of spots in the diffraction pattern of the CB (the upper inset) can be identified, revealing that the CB is a patchwork of four different types of domains.

^{*}Author to whom correspondence should be addressed. Electronic mail: chuanmingtseng@gmail.com.

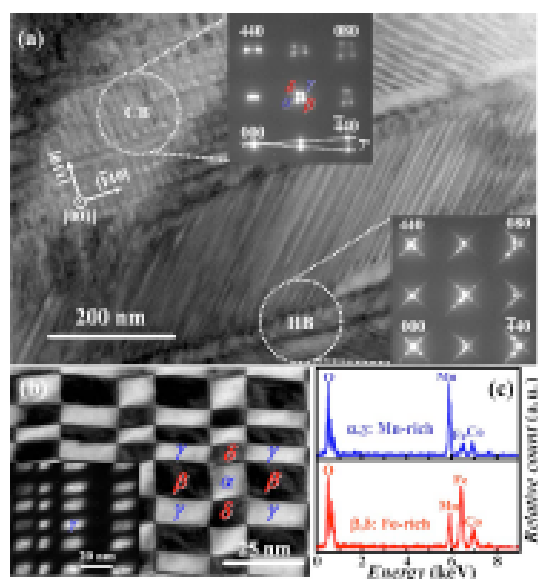


FIG. 1. (Color online) TEM image of $\text{Co}_{0.9}\text{Fe}_{0.9}\text{Mn}_{1.3}\text{O}_4$ annealed at 375°C for 324 h. (a) Bright field image of coexisting nanoscale CB and TB domains, the insets are the corresponding diffraction patterns. (b) High-resolution TEM image of the checkerboard, which consists of two cubic domains β/δ with different rotations and two tetragonal domains α/γ with different orientations. The inset is the dark field image taken by using γ spot around (008) position. (c) Energy dispersive EDS identifying the compositions of the cubic and tetragonal domains.

The detailed microstructural information of the CB is revealed through the analyses of dark-field image [Fig. 1(b)] and the corresponding electron diffraction [the insets of Fig. 1(a)]. The CB pattern is found to be an intricate patchwork of four different types of domains which give rise to four distinct diffraction peaks denoted as α , β , γ , and δ in the electron diffraction pattern. It is noted that α and γ domains are tetragonal whereas β and δ are cubic. The lattice constants are estimated from the positions of the diffraction peaks. The dark field image [the inset of Fig. 1(b)], using γ peak around (008) position, distinctly shows the highly ordered and alternating CBs of the tetragonal phase. The formation of complex microstructure is often concomitant with a chemical phase separation of the system during growth. Indeed, using energy dispersive x-ray spectrometry (EDS) with a fine electron probe $\sim 0.2\text{ nm}$ [Fig. 1(c)], we have determined the chemical compositions to be approximately $\text{Co}_{0.9}\text{Fe}_{1.0}\text{Mn}_{0.9}\text{O}_4$ (Fe rich) and $\text{Co}_{0.9}\text{Fe}_{0.9}\text{Mn}_{1.3}\text{O}_4$ (Mn rich) for the cubic (β and δ) and tetragonal (α and γ) domains, respectively. The cobalt concentration remains unchanged and uniform throughout the sample.

We now turn to the evolution of the microstructure with varying annealing time. Figure 2(a) shows the x-ray diffraction (XRD) patterns of $\text{Co}_{0.9}\text{Fe}_{0.9}\text{Mn}_{1.3}\text{O}_4$ annealed at 375°C . The crystal structure evolved remarkably with prolonged annealing time. Here, four notations C' , T' , C , and T are introduced to describe the structural change with annealing time. C' is a metastable cubic phase of the quenched sample. T' is an intermediate metastable tetragonal phase for the 3.6 h annealed sample. C denotes the Fe-rich cubic phase and T the Mn-rich tetragonal phase after the phase separation. The quenched sample undergoes a displacive, martensitic transformation during the first 10 min of annealing. We

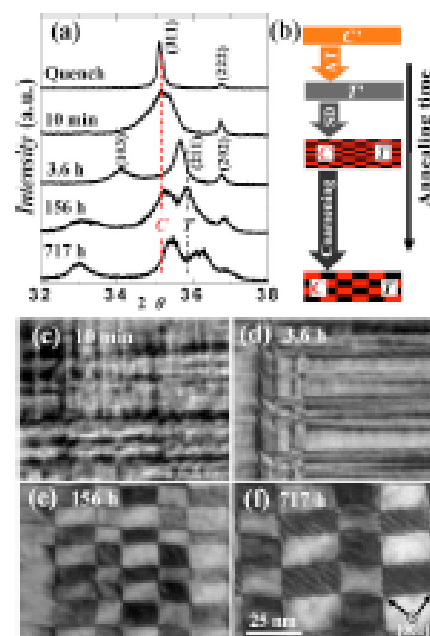


FIG. 2. (Color online) (a) XRD patterns of $\text{Co}_{0.9}\text{Fe}_{0.9}\text{Mn}_{1.3}\text{O}_4$ annealed at 375°C with selected annealing time. C' is the cubic phase of the quenched specimen, T' is the tetragonal phase of the 3.6 h annealed specimen, and the cubic and tetragonal peaks are detected. C and T are the final equilibrium cubic and tetragonal phases after phase separation. The dashed lines indicate the positions of (311) and (211) peaks. (b) Schematic process of crystal structure evolution with prolonged annealing time. [(c)–(f)]. The corresponding microstructure development with annealing time. All images share the same scale.

note from XRD patterns that the (311) peak has significantly broaden, whereas the (222) peak remains sharp. This suggests that the displacive distortions are confined in the (111) planes during the martensitic transformation. With further annealing, an allotropic transformation takes place which involves Mn^{2+} ions diffusing from A sites to B sites and then becoming JT active. Therefore, the C' phase is completely converted to the T' phase. The T' phase is highly unstable and immediately subjects to spinodal decomposition into C and T phase, demonstrated by the two sets of peaks in the 156 h-annealed specimen. The broadening of the cubic (311) and tetragonal (211) peaks is consistent with the appearance of nanostructure. No significant changes were observed beyond 156 h, suggesting that stable equilibrium has been largely reached. Thus, the whole structural evolution process starts from a supersaturated cubic phase C' , then allotropically transforms to a metastable tetragonal state T' , and eventually precipitated into two equilibrium phases through spinodal decomposition: C and T . Figure 2(b) is a schematic structural transformation pathway with annealing time: $C' \xrightarrow{\text{AT}} T' \xrightarrow{\text{SD}} C+T$.

Figures 2(c)–2(f) show bright-field TEM images indicating the corresponding pronounced changes of microstructure with annealing time from the initial tweed structure to the intermediate twin followed by nanoscale checkerboards. This is in good agreement with the structural evolution discussed above. The most impressive feature of the morphology evolution is that the size of CBs is tunable with annealing time. For the 10 min annealed sample, the tweed microstructure

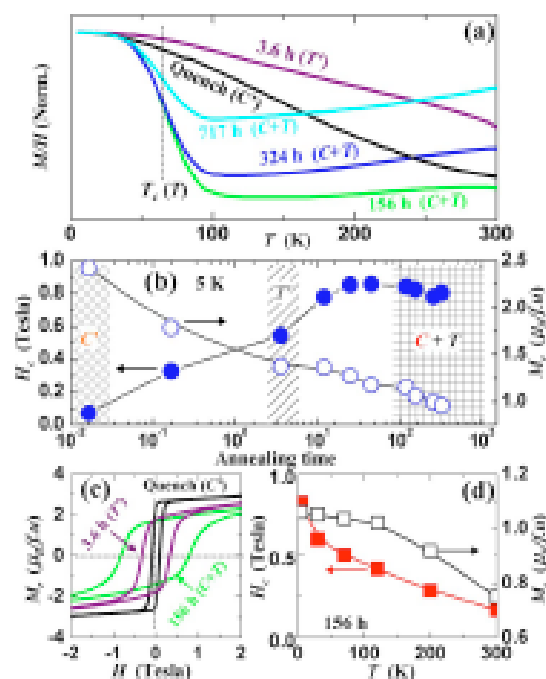


FIG. 3. (Color online) Magnetic properties of $\text{Co}_{0.5}\text{Fe}_{0.5}\text{Mn}_{1.5}\text{O}_4$ annealed at 375°C with selected annealing time. (a) Normalized M/H vs temperature with 200 Oe field cooling. (b) H_c (●) and M_r (○) vs annealing time in the logarithmic scale at 5 K; the shadow and patterned regions indicate the structure evolution with annealing time; (c) $M(H)$ at 5 K; (d) H_c (■) and M_r (□) vs temperature for the 156 h annealed specimen.

[Fig. 2(c)] along the elastically soft direction $[110]$ or $[\bar{1}10]$ occurs immediately as a result of the diffusionless martensitic transformation due to the rapid small cooperative displacements.¹¹ The presence of twinned domains (T' phase) observed in the 3.6 h annealed specimen [Fig. 2(d)] is crucial and serves as a template in the formation of the regular CB pattern. Unlike the isotropic C' phase with similar concentration gradients or strain in all directions, the T' phase, with unequal lattice parameters, is highly anisotropic, so that the preferential diffusion occurs along the elastically soft directions, which coincides with the boundaries of CBs. Prolonged annealing over 90 h led to the formation of ordered CB domains from the twinned structure of the T' phase. Subsequently, the CBs undergo continuous adjustment with annealing time: the average size of CBs varies from $-13.8 \times 7.9 \text{ nm}^2$ in the 90 h specimen up to $-17.3 \times 14.0 \text{ nm}^2$ in the 717 h specimen [Fig. 2(f)]. The compositions of the checkerboard domains are kept almost unchanged. This unambiguously indicates that the coarsening occurs without long range diffusion of ions, consistent with the subtle shift of (311) and (211) peaks [in Fig. 2(a)] and the invariant Curie temperature (T_c) of T phase [in Fig. 3(a)] with annealing time.^{12,13}

The normalized M/H versus temperature curves [Fig. 3(a)] show that T_c of C' and T' phases are above room temperature. A transition at -70 K signifying T_c of the T phase, $T_c(T)$, is observed for specimens with the formation of CB ($C+T$ phases). We note that T_c of the C phase, $T_c(C)$, as determined by high temperature M/H measurement, is located at a much higher temperature -560 K . $T_c(T)$ remains

nearly unchanged for all of the specimens with $C+T$ phases. This further confirms that the compositional fluctuation is small.

Figure 3(b) shows the coercivity H_c and remanent magnetization M_r versus annealing time in logarithmic scale at 5 K. H_c increases steadily from -710 Oe for the quenched sample to -8400 Oe for the 156 h annealed specimen, and remains largely unchanged -8000 Oe with even longer annealing. Correspondingly, M_r decreases from $-2.4 \mu_B/\text{f.u.}$ to $-1.1 \mu_B/\text{f.u.}$ then to $-0.06 \mu_B/\text{f.u.}$ (note that we took account of the magnetic contribution from the entire sample). Figure 3(c) displays $M(H)$ curves of specimens with C' , T' and $C+T$ phases, which clearly shows that the strong enhancement of coercivity due to the formation of nanorods. Once the nanorods are formed, their magnetic properties are quite stable with annealing time as evidenced by small variations of H_c and M_r . Figure 3(d) is H_c and M_r versus temperature for the 156 h annealed sample with the average size of the CB $-14 \times 9 \text{ nm}^2$. Since $T_c(T)$ is -70 K , the contribution of the measured magnetic properties above 70 K are mainly from the C phase. We did not observe any abrupt changes of H_c and M_r around 70 K , indicating the very weak magnetic properties of the T phase even at the low temperatures. If we only consider the contribution from the C phase, H_c and M_r at 300 K could be -2100 Oe and $-1.5 \mu_B/\text{f.u.}$, respectively. Compared with that of 10°C/h cooled $\text{MgMn}_{1.5}\text{Fe}_{0.5}\text{O}_4$ ($M_r = 0.27 \mu_B/\text{f.u.}$, $H_c = 150 \text{ Oe}$, at 300 K),⁴ the 156 h annealed $\text{Co}_{0.5}\text{Fe}_{0.5}\text{Mn}_{1.5}\text{O}_4$ shows a much larger coercivity and magnetization in the whole temperature range (the amount of C phase is assumed to be half in both samples).

In summary, magnetically ordered arrays of three-dimensional nanoscale checkerboards were achieved in $\text{Co}_{0.5}\text{Fe}_{0.5}\text{Mn}_{1.5}\text{O}_4$, and the size can be readily tuned with the isothermal annealing time. Furthermore, checkerboards with dimension $-13 \times 9 \text{ nm}^2$ were observed in a $\text{Co}_{0.5}\text{FeMn}_{1.5}\text{O}_4$ sample. If our remarkable pattern is realized on films, it possibly extends the magnetic storage density up to $1\text{--}10 \text{ Tb/in}^2$.

We thank the useful discussion with Dr. Y. Ni, a postdoctoral fellowship from the Department of Materials Science and Engineering, Rutgers University. The research was supported by the National Science Council, Taiwan, under the Contract Nos. NSC95-2752-M-002-006-PAE (National Taiwan University) and NSF-DMR-0405682 (Rutgers).

¹S. Yeo, Y. Horibe, S. Mori, C. M. Tseng, C. H. Chen, A. G. Khachatryan, C. L. Zhang, and S.-W. Cheong, *Appl. Phys. Lett.* **89**, 233120 (2006).

²J. I. Martin, J. Nogata, K. Liu, J. L. Vicent, and I. K. Schuller, *J. Magn. Magn. Mater.* **256**, 449 (2003).

³J. V. Barth, G. Costantini, and K. Kern, *Nature (London)* **437**, 671 (2005).

⁴C. L. Zhang, S. Yeo, Y. Horibe, Y. J. Choi, S. Guha, M. Croft, S.-W. Cheong, and S. Mori, *Appl. Phys. Lett.* **90**, 133123 (2007).

⁵R. Skomski, *J. Phys.: Condens. Matter* **15**, R841 (2003).

⁶K. Mizuta, A. Muramatsu, S. K. Hasanain, and A. Ceylan, *J. Magn. Magn. Mater.* **308**, 289 (2007).

⁷Z. Zhang, A. J. Rondinone, J. X. Ma, J. Shen, and S. Dai, *Adv. Mater. (Weinheim, Ger.)* **17**, 1415 (2005).

⁸Z. H. Han, R. S. Chen, C. L. Li, S. G. Yang, M. Lu, B. X. Gu, and Y. W. Du, *J. Alloy Compd.* **427**, 199 (2007).

⁹S. Tamura, *Physica B* **190**, 150 (1993).

¹⁰T. W. McDaniel, *J. Phys.: Condens. Matter* **17**, 315 (2005).

¹¹S. Kartha, *Phys. Rev. B* **52**, 803 (1995).

¹²Y. Ni, Y. M. Jia, and A. G. Khachatryan, *Acta Mater.* **55**, 4903 (2007).

¹³H. Romanowicz and T. A. Abinandanan, *Physica A* **318**, 213 (2003).

Curriculum Vitae

Chenglin Zhang

1. Educations

2002. 9. – Present Ph. D. in Physics and Astronomy, Rutgers University, New Jersey, U. S. A.
 2000. 9. – 2002. 7. M. S. in physics, Institute of Solid State Physics, CAS, Hefei, China
 1999. 9. – 2000. 6. in physics, University of Science and Technology, Hefei, China
 1995. 9. – 1999. 6. B. S. in Physics, Hubei University, Wuhan, China

2. Publications

1. Multiferroicity in the spin-1/2 quantum matter of LiCu_2O_2
 A. Rusydi, I Mahns, S. Muller, M. Rubhausen, S. Park, Y. J. Choi, C. L. Zhang, S.-W. Cheong, S. Smadici, P. Abbamonte, M. von Zimmermann, and G. A. Sawatzky,
Appl. Phys. Lett. **92**(26), 262506 (2008)
2. Raman scattering studies of the temperature- and field-induced melting of charge order in $\text{La}_x\text{Pr}_y\text{Ca}_{1-x-y}\text{MnO}_3$
 M. Kim, H. Barath, S. L. Cooper, P. Abbamonte, E. Fradkin, M. Rubhausen, C. L. Zhang, and S.-W. Cheong,
Phys. Rev. B. **77**(13), 134411 (2008)
3. Magnetic nanocheckerboards with tunable sizes in the Mn-doped CoFe_2O_4 spinel.
C. L. Zhang, C. M. Tseng, C. H. Chen, S. Yeo, Y. J. Choi, and S.-W. Cheong,
Appl. Phys. Lett. **91**(23), 233110 (2007)
4. Covercivity and nanostructure in magnetic spinel $\text{Mg}(\text{Mn},\text{Fe})_2\text{O}_4$.
C. L. Zhang, S. Yeo, Y. Horibe, Y. J. Choi, S. Guha, M. Croft, S.-W. Cheong, and S. Mori
Appl. Phys. Lett. **90**, 133123 (2007)
5. Valence Changes and Structural Distortions in "Charge Ordered" Manganites Quantified by Atomic-Scale Scanning Transmission Electron Microscopy
 J. C. Loudon, L. F. Kourkoutis; J. S. Ahn, C. L. Zhang, S.-W. Cheong and D. A. Muller,
Phys. Rev. Lett. **99**, 237205 (2007)
6. Colossal magnon-phonon coupling in multiferroic $\text{Eu}_{0.75}\text{Y}_{0.25}\text{MnO}_3$
 R. Valdes Aguilar, A. B. Sushkov, C. L. Zhang, Y. J. , Choi, S.-W. Cheong, and H. D. Drew,
Phys Rev B, **76**(6), 060404 (2007)
7. Ferroelectricity in a $S=1/2$ Chain Cuprate.
 S. Park, Y. J. Choi, C.L. Zhang, and S.-W. Cheong,
Phys. Rev. Lett. **98**(5), 057601(2007)
8. Solid state self-assembly of nanocheckerboards
 S. Yeo, Y. Horibe, S. Mori, C. M. Tseng, C. H. Chen, A. G. Khachaturyan, C. L. Zhang, and S.-W. Cheong,
Appl. Phys. Lett. **89**(23), 233120 (2006)
9. Jahn-Teller effect in spinel manganites probed by soft x-ray absorption spectroscopy
 H. J. Noh, S. Yeo, J.-S. Kang, C. L. Zhang, S.-W. Cheong, S.-J. Oh, and P. D. Johnson,
Appl Phys Lett, **88**(8), 081911 (2006)

10. Relating supercooling and glass-like arrest of kinetics for phase separated systems:
Doped CeFe_2 and $(\text{La,Pr,Ca})\text{MnO}_3$.
K. Kumar, A. K. Pramanik, A. Banerjee, P. Chaddah, S. B. Roy, S. Park, C. L. Zhang, and S.-W. Cheong,
Phys Rev B, **73**(18), 184435 (2006)
11. Magnetic Inversion Symmetry Breaking and Ferroelectricity in TbMnO_3
M. Kenzelmann, A. B. Harris, S. Jonas, C. Broholm, J. Schefer, S. B. Kim, C. L. Zhang, S. W. Cheong, O. P. Vajk, and J. W. Lynn,
Phys. Rev. Lett, **95**(8), 087206 (2005)